AUTONOMOUS RECEIVERS FOR NEXT-GENERATION OF HIGH-SPEED OPTICAL COMMUNICATION NETWORKS

A Dissertation
Presented to
The Academic Faculty

by

Pierre Isautier

In Partial Fulfillment
of the Requirements for the Degree
Doctor of Philosophy in the
School of Electrical and Computer Engineering

Georgia Institute of Technology
December 2015

AUTONOMOUS RECEIVERS FOR NEXT-GENERATION OF HIGH-SPEED OPTICAL COMMUNICATION NETWORKS

Approved by:

Dr. Stephen E. Ralph, Advisor
School of Electrical and Computer Engineering
Georgia Institute of Technology

Dr. John Barry
School of Electrical and Computer Engineering
Georgia Institute of Technology

Dr. Matthieu Bloch
School of Electrical and Computer Engineering
Georgia Institute of Technology

Dr. Branislav Vidaković
School of Industrial and Systems Engineering
Georgia Institute of Technology

Dr. Richard DeSalvo
Photonics Core Technology Center
Harris Corporation

Date Approved: November 2, 2015

За Зорану

ACKNOWLEDGEMENTS

PREFACE

Any sufficiently advanced technology is indistinguishable from magic.

Arthur C. Clarke

In the world of today, it might be difficult to discern telecommunications technology from magic, as the former has reached impressive levels of progress. Indeed, the ability to communicate with each other instantaneously from almost anywhere in the world has become commonplace and can be done at virtually no cost from a plethora of synchronized platforms (including phones, desktops, laptops, tablets, and even watches to name a few). As the democratization and globalization of telecommunications have enabled organizations to operate faster and more efficiently at a global scale, sovereign states and their citizens continuously feel threatened, externally and internally, because disruptive entities to the social order have also expanded their spheres of influence globally.

In 2013, major media disclosures exposed the existence of clandestine global surveillance programs, under which governmental intelligence agencies had collected individuals' communications from technology companies and communications service providers. These major media disclosures revealed that these governments made the choice to protect their citizens at any cost, even if it implied trading liberty for security. Global government-sponsored surveillance programs have since become controversial. While one segment of the population condones government surveillance in the interest of collective security, others believe it is violating essential liberties, mirroring ideals emanating from

the Age of Enlightenment. One of the Founding Fathers of the United States of America, Benjamin Franklin, once expressed such sentiment: "Those who would give up essential liberty, to purchase a little temporary safety, deserve neither liberty nor safety" (Benjamin Franklin, for the Pennsylvania Assembly in its Reply to the Governor, November 11th 1755).

This Doctoral dissertation exposes the fundamental principles for acute monitoring and surveillance of telecommunications in modern optical networks. The author, a fervent believer in individual liberties ending precisely where another man's liberties begin, sincerely hopes that this resource will be used responsibly. As Sir Winston Churchill famously said, echoing many others before him: "Where there is great power, there is great responsibility" (Sir Winston Churchill, in the House of Commons, February 28, 1906).

RECOGNITIONS

Fortune favors the ~~bold~~ innocent.

~~Latin~~ French Proverb

I consider myself blessed, for having had the privilege to work under the supervision of Dr. Stephen E. Ralph. The day I joined the *Georgia Institute of Technology Terabit Optical Networking Consortium*, Monday August 13th 2012, I had very superficial knowledge in the overlapping fields of Optics, Photonics, Fiber Optic Communications, and Digital Signal Processing. It took hard work and determination to accomplish this Doctoral thesis, but what really contributed to this accomplishment was Dr. Ralph's vision, guidance, breadth and depth of expertise, energy, ambition, patience, and generosity, to name a few of his qualities; qualities that helped me grow, professionally and personally,

beyond what I would have ever expected to, when I first started my Doctorate. Therefore, my first acknowledgement goes to Dr. Ralph.

Then, I would like to thank my parents for the quality of education and the life philosophy they provided me, as well as their unconditional support throughout my life; my brothers for their encouragements and support; and my extended family for helping me in my deepest needs.

I would also like to thank Dr. Smadja, from the *Lycée Français de Los Angeles*, and Dr. François Vandenbrouck, formerly from the *Lycée Janson de Sailly* (now teaching at the *Lycée Louis-le-Grand*) for inculcating me the passion for this amazing science that is Physics.

I am very grateful for both the French and American Education Systems, which are very complementary to my opinion. While the French Education System taught me how to flirt with my mental capabilities' limit, and enabled me to develop high quality, theoretical, scientific knowledge through *Classes Préparatoires aux Grandes Ecoles*; the American Education System, through the *Georgia Institute of Technology*, refined my knowledge, taught me different perspectives, helped me develop practical expertise, and gave a meaning and impact to my studies.

Next, I wish to thank all my former and current colleagues, who made my learning experience more enjoyable and meaningful: Dr. Andy Stark, Dr. Jie Pan, Sriharsha Kota Pavan, Patrick Decker, Kevin Anzalone, Justin Lavrencick, Evan Atwood, Jerrod Langston, David Haupt and recent colleagues, Alirio Melgar, Siddharth Varughese, and Edward Tan.

My next acknowledgements go to Drs. Matthieu Bloch, and DeSalvo for serving on my reading committee and Drs. Branislav Vidaković, and John Barry for hearing my Doctoral defense to ensure the quality of this Doctoral Dissertation.

American people are truly both fascinating and remarkable people. Their kindness, enthusiasm, curiosity, energy, and work ethic made my Doctoral experience really pleasant and exceptional, and I would like to thank all the people I have met during my American journey and who helped me aspire to become a better person.

Last, I want to thank my girlfriend for her good mood, energy, and unconditional support, without who this American journey would have not been complete.

TABLE OF CONTENTS

LIST OF TABLES

LIST OF FIGURES

Page

LIST OF SYMBOLS AND ABBREVIATIONS

SYMBOLS

A	Mode Weight Factor
a	Radius of the Fiber Core
B	Bandwidth
$\vec{B}$	Magnetic Flux Density Vector in Space and Time
C	Channel Capacity Limit
$\tilde{C}$	Channel Capacity
$C_{4,i}$	i^{th} Fourth-Order Cumulant of 2-Dimensional Projected Clusters Coordinates in the Plane Q
$\tilde{C}_{4,i}$	Normalized Estimate of i^{th} Fourth-Order Cumulant of 2-Dimensional Projected Clusters Coordinates in the Plane Q
$\tilde{C}_{4,i,w}$	Normalized Weighted Estimate of i^{th} Fourth-Order Cumulant of 2-Dimensional Projected Clusters Coordinates in the Plane Q
${C_{4,i}}^{n}$	i^{th} Fourth-Order Cumulant of the Digital Signal x_n
${\tilde{C}_{4,i}}^{n}$	Normalized Estimate of i^{th} Fourth-Order Cumulant of the Digital Signal x_n
c	Speed of Light in the Vacuum
D	Dispersion Parameter
$\vec{D}$	Electric Flux Density Vector in Space and Time
$\overrightarrow{\tilde{D}}$	Fourier Transform of the Electric Flux Density Vector
$d\vec{l}$	Element of Length
$d\vec{S}$	Element of Surface
dV	Element of Volume
$\vec{E}$	Electric Field Vector in Space and Time

$\vec{\tilde{E}}$	Fourier Transform of the Electrical Field Vector
E_x (E_y)	Transverse Distribution of the Electric Field Vector Linearly Polarized Along the x (y) Direction
$\overrightarrow{E_x}$ $(\overrightarrow{E_y})$	Electric Field Vector Linearly Polarized Along the x (y) Direction
e_x (e_y)	X (Y) Polarization Error Signal
F_s	Sampling Rate of the Analog-to-Digital Converter
$\vec{F}_2$	Coulomb's Force on the Electric Charge 2
f_c	Carrier Frequency
f_{max}	Frequency of the Spectrum Edge of the Transmitted Signal
f_{symbol}	Symbol Rate
$\vec{H}$	Magnetic Field Vector in Space and Time
H_{CD}	Frequency Domain Transfer Function of an Optical Fiber Under Chromatic Dispersion
$h(Y)$	Differential Entropy of the Continuous Random Variable Y
$h(Y\|X)$	Conditional Entropy of the Continuous Random Variable Y Given the Knowledge of X
$I(X;Y)$	Mutual information Between Random Variables X and Y
I_S	Direct Current Flowing Through the Surface S
$i_{i,S}$	i^{th} Discrete Direct Current Flowing Through the Surface S
$\boldsymbol{J}$	Jones Matrix
$\vec{j}$	Current Density
k_0	Wavenumber in the Vacuum
$\vec{M}$	Magnetic Polarization Vector of the Medium in Space and Time
m	Modulating Signal
n	Refractive Index of the Medium
n_0	Refractive Index of Air

n_1	Refractive Index of Medium 1
n_2	Refractive Index of Medium 2
n_2	Kerr Coefficient
$\vec{P}$	Dielectric Polarization Vector in Space and Time
$\vec{\tilde{P}}$	Fourier Transform of the Dielectric Polarization Vector
$\overrightarrow{P_L}$	Linear Dielectric Polarization Vector in Space and Time
$\overrightarrow{P_{NL}}$	Nonlinear Dielectric Polarization Vector in Space and Time
Q_V	Total Electric Charge Enclosed by the Volume V
$q_{i,V}$	i^{th} Discrete Electric Charge Contained in the Volume V
q_1 (q_2)	Electric Charge 1 (2)
R_k	Responsivity of the Coherent Receiver Photodetector k
$\hat{R}_T^{(\alpha)}$	Classical Estimator for Blind Symbol Rate Estimation
$\hat{S}_T^{(\alpha)}$	Weighted Estimator for Blind Symbol Rate Estimation
S_{Xk}	Output Electrical Signal of the Coherent Receiver Photodetector k
V	Normalized Frequency
V_{in}	Driving Voltage
V_π	Half-Wave Voltage of the Modulator
α	Attenuation Coefficient
$\alpha(dB/km)$	Normalized Loss Parameter
α_i	i^{th} Cluster Weight in 3-Dimensional Stokes Space
$\alpha_{Q,i}$	i^{th} Cluster Weight in 2-Dimensional Plane Q
β	Propagation Constant
β_r	Real-Part of the Propagation Constant
β_1	First-Order Dispersion Coefficient

β_2	Second-Order Dispersion Coefficient
β_3	Third-Order Dispersion Coefficient
Γ	Asymptotic Covariance Matrix of the Classical Estimator for Blind Symbol Rate Estimation
$\hat{\Gamma}$	Estimate of the Asymptotic Covariance Matrix of the Classical Estimator for Blind Symbol Rate Estimation
Γ_{XY}	Spatial Cross-Correlation Index Between the Observations X and Y
Δ	Laplace Operator
$\Delta\tau_{DGD}$	Differential Group Delay
ε	Permittivity in the Medium
$\hat{\varepsilon}_x$ ($\hat{\varepsilon}_y$)	Estimator of the Timing Phase Error in the X (Y) Polarization Signal
ε_0	Permittivity in the Vacuum
θ_c	Critical Angle
θ_{max}	Acceptance Angle
θ_1	Angle of Incidence
θ_{1r}	Angle of Reflexion
θ_2	Angle of Refraction
λ	Wavelength of the Light in the Medium
λ_{cutoff}	Cutoff Wavelength
λ_i	i^{th} Cluster Dirichlet Concentration Parameter in 3-Dimensional Stokes Space
$\lambda_{Q,i}$	i^{th} Cluster Dirichlet Concentration Parameter in 2-Dimensional Plane Q
λ_0	Wavelength of the Light in the Vacuum
μ	Permeability of the Medium
μ	Constant Modulus Algorithm Step-Size Parameter
$\vec{\mu}_i$	i^{th} Cluster Mean Position in 3-Dimensional Stokes Space
$\vec{\mu}_{Q,i}$	i^{th} Cluster Mean Position in 2-Dimensional Plane Q

μ_0	Permeability of the Vacuum
μ_φ	Carrier Phase Recovery Step-Size Parameter
ρ	Volume Electric Charge Density
σ_N^2	Noise Power of the Complex Gaussian Random Variable N
$\sigma_{sampling-jitter}$	Root Mean Square Sampling Jitter
φ	Carrier Phase Noise
$\tilde{\varphi}$	Estimate of the Carrier Phase Noise
Φ	Transverse Field Distribution
χ	Susceptibility of the Medium
$\tilde{\chi}$	Fourier Transform of the Susceptibility of the Medium
$\chi^{(j)}$	j^{th} Order Susceptibility
χ_{eff}	Effective Susceptibility of the Medium
$\chi_{xx}{}^{(1)}$	Component of the Second-Rank Tensor $\chi^{(1)}$
$\chi_{xxxx}{}^{(3)}$	Component of the Fourth-Rank Tensor $\chi^{(3)}$
Ψ	Any Component of the Electric/ Magnetic Field Vector in Space and Time
$\boldsymbol{\omega}$	Angular Frequency

ABBREVIATIONS

AAH	Asynchronous Amplitude Histogram
ADC	Analog-to-Digital Converter
ANN	Artificial Neural Networks
APSK	Amplitude and Phase-Shift Keying
ASE	Amplified Spontaneous Emission
ASK	Amplitude-Shift Keying
ASIC	Application-Specific Integrated Circuit

BER	Bit Error Rate
BPSK	Binary Phase-Shift Keying
CD	Chromatic dispersion
CMA	Constant Modulus Algorithm
CO-OFDM	Coherent Optical Orthogonal Frequency-Division Multiplexing
CSP	Communications Service Provider
DD	Decision-Directed
DAC	Digital-to-Analog Converter
DCF	Dispersion Compensating Fiber
DFB	Distributed-Feedback
DGD	Differential Group Delay
DSF	Dispersion-Shifted Fiber
DSP	Digital Signal Processing
EC	External Cavity
EDFA	Erbium-Doped Fiber Amplifier
ENoB	Effective Number of Bits
FEC	Forward Error Correction
FSK	Frequency-Shift Keying
FWM	Four-Wave Mixing
GMM	Gaussian Mixture Model
HOS	Higher Order Statistics
ICA	Independent Component Analysis
ICI	Inter-Channel Interference
IF	Intermediate Frequency
IP	Internet Protocol

ISI	Inter-Symbol Interference
LAF	Large-Area Fiber
LED	Light-Emitting Diode
LO	Local Oscillator
LMS	Least Mean Square
LN	Lithium Niobate
LNA	Low-Noise Amplifier
MFR	Modulation Format Recognition
MIMO	Multiple-Input Multiple-Output
MZI	Mach-Zehnder Interferometer
MZM	Mach-Zehnder Modulator
NA	Numerical Aperture
NRZ	Non-Return-to-Zero
NZDSF	Non-Zero Dispersion Shifted Fiber
OFDM	Orthogonal Frequency-Division Multiplexing
OOK	On-Off Keying
OSNR	Optical Signal-to-Noise Ratio
PCA	Principal Component Analysis
PDF	Probability Density Function
PDL	Polarization Dependent Loss
PDM	Polarization Division Multiplexing
PMD	Polarization Mode Dispersion
PRBS	Pseudo-Random Bit Sequence
PSK	Phase-Shift Keying
QAM	Quadrature Amplitude Modulation

QPSK	Quadrature Phase-Shift Keying
RC	Raised Cosine
RF	Radio Frequency
RoF	Radio-over-Fiber
RRC	Root Raised Cosine
ROADM	Reconfigurable Optical Add/Drop Multiplexer
RZ	Return-to-Zero
SDM	Space-Division Multiplexing
SDN	Software-Defined Networking
SE	Spectral Efficiency
SINAD	Signal-to-Noise-and-Distortion Ratio
SNR	Signal-to-Noise Ratio
SOP	State of Polarization
SPM	Self-Phase Modulation
SSMF	Standard Single Mode Fiber
TDHMF	Time-Domain Hybrid Modulation Format
WDM	Wavelength Division Multiplexing
XPM	Cross-Phase Modulation

SUMMARY

Advances in fiber optic communications and the convergence of the optical-wireless network will dramatically increase the network heterogeneity and complexity. The goal of our research is to create smart receivers that can autonomously identify and demodulate, without prior knowledge, nearly any signal emerging from the next-generation of high-speed optical communication networks.

CHAPTER 1

INTRODUCTION

1.1 BACKGROUND

The Global Capacity Demand

The continuing and relentless demand for capacity in the global network is predominantly fueled by growing Internet Protocol (IP) traffic. There are many drivers behind this growth. Increased global penetration of broadband access at home and on wireless devices, have enabled consumers to use high-speed Internet, anytime, anywhere, for: browsing, social networking, accessing cloud services, utilizing Internet video services applications, or mobile services applications. At the same time, businesses increasingly rely on high-speed networks, as a communication medium for internal, business-to-consumer, or business-to-business use, to conduct their operations. According to the Cisco Visual Networking Index, which forecasts and analyses the growth and use of IP networks worldwide, annual global IP traffic will increase nearly threefold over the next five years (2014-2019), surpassing the zettabyte (or 10^{21} bytes – which is the capacity equivalent to about 100 million Libraries of Congress worth of data included in all printed materials) threshold in 2016, and the two zettabyte threshold in 2019 [1].

An Increasingly Heterogeneous Network

Technological advances have succeeded in continuously reducing the cost of bandwidth, spurring the development of new sets of services and transmission technologies deployed alongside older ones, resulting in increased levels of heterogeneity in the telecommunication ecosystem. This development of new solutions in turns drives an increased need for bandwidth in the network, resulting in a positive feedback cycle [2].

The Perfect Storm

These technologically-driven changes in the telecommunication industry have resulted in multiple challenges for communications service providers (CSPs). CSPs have to address the growing need for bandwidth, manage an increasingly heterogeneous network, and maintain the required quality of service (QoS) of its service portfolio, while remaining competitive and profitable. In addition to these challenges, CSPs have been confronted to a revenue stagnation since 2012, while capital expenditures (CapEx) and operational expenditures (OpEx) have soared. As an illustration, $2 trillion in network investments will be needed over the next decade to keep pace with traffic demand. This divergence between the growth of revenue and cost is setting the atmosphere for a "Perfect Storm" [3], Fig. 1.1, which might result in a disruption within the telecommunication industry causing the necessary redefinition of some of its segments.

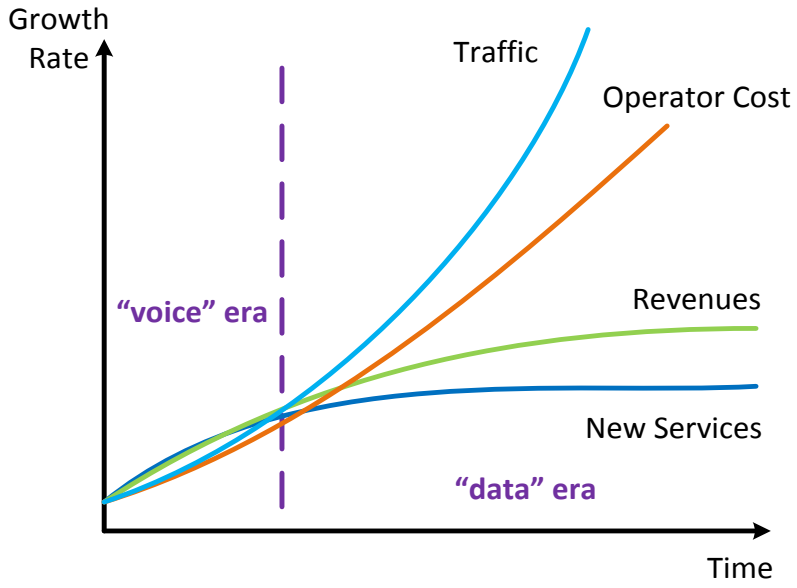

Fig. 1.1. Traffic, cost, and revenue growths trends in the telecommunication industry. Source: [3].

The Fiber Optic Backbone

High-data rate transmissions over optical fiber have demonstrated the undeniable superiority of optical communications in terms of capacity and reach. As a consequence,

for data transmissions over few tens of megabits per second and over anything from hundreds of meters and upwards, optical fiber has become the preferred transmission medium, making fiber optics, de facto, the backbone of our telecommunications and data networking infrastructures.

But optical networks have other advantages beyond contributing enormous capacities to the network, such as providing a common infrastructure over which a variety of services can be delivered, and to a certain degree, spatio-temporal flexibility in the delivery of bandwidth.

Growingly Complex Optical Networks

Similar to the telecommunication network in its whole, optical networks have grown more complex. Indeed, the field of fiber optic communications has advanced significantly over the last three decades. Fiber optic usable bandwidth has evolved from an under-utilization in the early days, to an extensive utilization via improvements in spectral efficiency (SE). In fact, because of uninterrupted development in high-speed electronics, advances in fiber optic network optical elements, and the use of advanced signaling techniques, optical communication systems have reached a state of greater signal waveform flexibility and higher single channel data rates that now exceed 200 Gb/s [4]. As a result, the next generation of fiber optic communication systems is leaning towards a larger degree of dynamic adaptability in reach, data rate, and spectral occupancy [5], thus shifting away from legacy single purpose transceivers.

Limitations of Fiber Optic Communications

However, some limitations of optical fiber communication networks lie in their lack of mobility and required intensive infrastructures. Certainly, deploying or redeploying optical fiber is costly, time-consuming, and can be problematic in some environment. This

is the case for highly urban areas or extreme geographical locations where infrastructure costs are significant, or in the worst case, laying the optical fiber is practically impossible.

Advantages of Wireless Communications

On the contrary, conventional microwave radio technology is rapid to deploy and is suited for mobile and remote environments, but is challenged by the growing data demands of users.

Wireless and Mobile Devices Growth

Yet, according to the Cisco Visual Networking Index, IP traffic from wireless and mobile devices will exceed traffic from wired devices by 2019. Specifically, in 2019, wired devices will account for a third of IP traffic, while Wi-Fi and mobile devices will account for two-third. In 2014, IP traffic was roughly split in half between wired and wireless devices [1].

The Emergence of High-Data Rate Wireless Transmissions

Multi-gigabit wireless photonics enable bridging fiber optic and wireless networks in a seamless fashion, via the interposition of wireless gateway which enables the conversion of optical signals to electrical wireless signals and vice versa [6]. This technology provides the maneuverability and capacity required in some applications, since it retains the mobility and deployment ease of wireless while providing fiber optic equivalent capacities and latencies to fixed and mobile users within a coverage area.

Therefore, evolutions in fiber optic network optical elements, high-speed electronics, and the convergence of the optical-wireless network have already and will dramatically increase the network heterogeneity as well as its complexity.

The Supervisory Control Layer and its Limitations

Managing greater heterogeneity and complexity for modern communication network is feasible with the cooperation of an omniscient supervisory control layer, which role is to ensure coordination between all elements of the network for smoother data transmission from one client site to another.

However, there are important situations where network elements are not properly synchronized with the flowing signal, despite conventional procedures that the supervisory control layer usually carries to solve a problem. For example, the optical receiver either cannot or does not know the properties of the incoming signal, thus cannot extract the information, because the supervisory channel is disrupted or deemed too slow to allow fast and flexible provisioning.

Additionally, managing multiple environments can, not only result in suboptimal performance, but also impact CSPs' costs as the complexity of the network grows.

1.2 MOTIVATION

The telecommunication industry is at a crossroad. A new landscape of competitive challenges and opportunities is surfacing, with the following major trends: an increasing global demand for IP traffic, driven by higher data rates needs and growing wireless devices data traffic; and the development of new sets of services and transmission technologies coexisting with currently deployed solutions, adding to the complexity of an increasingly heterogeneous network, and contributing to CSPs' costs.

New technology-driven solutions need to address these issues. Enabling networks with the ability to self-configure and self-optimize, with minimum human supervision, can help CSPs offset their costs, and free up cash flows necessary to deploy next-generation telecommunications and data networking infrastructures required to sustain the global need for bandwidth.

Key enablers for greater network independence are autonomous receivers. The concept of autonomous receiver consists of a universal intelligent receiver, that can operate

fully autonomously, requiring no intervention from a network operator or a supervisory control layer, and which can identify and demodulate any signal, without prior knowledge and with negligible acquisition delay.

The research interests of this dissertation are at the intersection of ultra-high speed optical communication networks, software-defined optical transceivers, secure optical networks, and multi-gigabit photonic assisted wireless systems. The ultimate goal of these efforts is to create autonomous receivers for signals transported within fiber optic communication networks, including fiber optic links and multi-gigabit photonic assisted wireless links.

This dissertation primarily focuses on exploring architectural design of autonomous receivers for fiber optic communication links and photonic assisted wireless communication links.

1.3 OUTLINE OF THE DISSERTATION

This dissertation is arranged in five chapters. Because optical communications is an interdisciplinary field that combines photonic/optoelectronic devices and communication systems, Chapter 2 details: the fundamental physical phenomena that describe optical propagation in the fiber optic channel, the system components involved in fiber optic networks, and the conventional communication concepts and technologies involved in optical transmissions.

Chapter 3 describes the state of the art of research and development in the fields of: cognitive optical networks, fiber optic communications (including training-aided digital signal processing, blind digital signal processing, software-defined optical transceivers, and optical performance monitoring technologies), and wireless photonics communications.

Chapter 4 contains the main contributions of this dissertation. It focuses on: the concept of autonomous receivers, the motivation and applications behind, and investigates:

architectures for fiber optic communication links, architectures for photonic assisted wireless communication links, and blind parameters (including optical link impairments parameters and signal parameters) identifications techniques. Various novel modulation format recognition (MFR) algorithms are also introduced in this Chapter.

Chapter 5 discusses the concept of blind signal reconstruction, some applications, and investigates preliminary architectures enabling high-fidelity signal reconstruction.

Finally, Chapter 6 concludes this dissertation with: a review of key concepts introduced in Chapter 4 and 5, a summary of all contributions made in the field, and a suggestion for future research topics.

CHAPTER 2

FIBER OPTIC COMMUNICATION SYSTEMS

This chapter aims at providing the necessary background in optics, photonics, and communications systems, required to understand, with minimum prior knowledge, the topics covered in this dissertation, and appreciate the presented contributions. This chapter does not claim to provide any novelty in the field of optical communications, and is heavily inspired from the synthetic work of Ramaswami et al. [7], Kumar et al [8], Stark et al. [9], and Pan et al. [10].

In Section 1, we review a short history of optical networks. Section 2 covers the physical phenomenon and the limitations involved in the transmission of light in fiber optic links. In Section 3, we investigate components supporting optical networks. Section 4 and Section 5 deal with the signaling aspect of optical communications, particularly, Section 4 covers modulation concepts that describe how electrical signals carrying information are converted to light signals that can be transported in the fiber optic network; and Section 5 covers the retrieval of the information from an optical signal.

2.1 HISTORY OF OPTICAL NETWORKS

The history of optical fiber transmission has been about continuously improving key macro transmission metrics such as higher capacity, longer distances, and lower cost per bit transmitted per kilometer.

Today, the undeniable superiority of fiber optic transmission in terms of capacity, reach, and cost per bit transmitted per kilometer, has made optical fiber become the primary transport medium for metropolitan, regional, and global telecommunications.

2.1.1 EARLY STAGES

Glass Fiber as a Waveguide

The 1960s marked the dawn of optical fiber transmission systems. Relatively quickly after Theodore H. Maiman introduced the first ruby laser in 1960, based on the theoretical work of Charles H. Townes and Arthur L. Schawlow; early experiments proved, in the mid-1960s, that optical transmission over fiber optic was feasible [2].

An optical fiber is a thin cylindrical glass waveguide consisting of an inner core material and an outer cladding material. The core and cladding are designed to contain light inside the fiber allowing the transmission of light signals from one end to the other.

Optical fiber has multiple advantages. Principally made of glass, the raw materials are both inexpensive and abundant. Additionally, silica enables low-loss propagation over reasonably long distances of optical frequencies which is not possible in coaxial waveguides or wire transmission lines. Finally, optical fibers are immune to various electromagnetic interferences.

Loss in Optical Fibers and Transmission Windows

Early generations of optical fibers were highly lossy (~1000 dB/km). Manufacturing process refinements in the early 1970s enabled drastic reduction of this loss [2]. Modern silica-based optical fiber has three low-loss windows in the 0.8 μm infrared wavelength band (also known as the first transmission window), in the 1.3 μm infrared wavelength band (also known as the second transmission window), and in the 1.55 μm infrared wavelength band (also known as the third transmission window). The loss is about 1.5-2 dB/km in the 0.8 μm wavelength window, 0.5 dB/km in the 1.3 μm wavelength window, and 0.2 dB/km in the 1.55 μm wavelength window [11].

Early Optical Fibers and Intermodal Dispersion

The early fibers were multimode fibers [2]. Multimode fibers have core diameters of ~ 50 - 85 μm. Since the core diameter is larger than the wavelength of the optical carrier, intermodal dispersion occurs, limiting considerably the reach of multimode fiber systems.

Intermodal dispersion results, at the output of the optical fiber, in a spatiotemporal stretch of the input optical bit pulses, because the optical signal energy propagates in the optical waveguide by taking simultaneously different optical paths, or modes, with different propagation time.

Regenerators

A regenerator is an optoelectronic device that converts the input optical signal into an electrical signal, and retransmits that electrical signal, after having corrected some transmission impairments, in a new optical signal. Multimode fibers enabled transmission of optical signals over distances of several tens of kilometers before they needed to be regenerated [2].

Early Telecommunication Systems Design and Performance (Late 1970s – early 1980s)

Early telecommunication systems used multimode fibers with light-emitting diodes (LEDs) or laser transmitters in the first or second transmission window (0.8 and 1.3 μm wavelength bands respectively) [2]. LEDs are lower output power optoelectronic devices that emit light over a wide spectrum of several nanometers [2]. Early generation of lasers (multilongitudinal mode Fabry-Perot lasers) also emitted light over a wide spectrum of several nanometers, but provided higher output power than LEDs, and therefore allowed transmission over greater distances before requiring regeneration [2].

These early systems had to have regenerators every few kilometers to regenerate the signal [2]. Typically, these early systems operated at bit rates ranging from 32 to 140 Mb/s with regenerators every 10 km [2].

2.1.2 SINGLE MODE FIBER

Single Mode Optical Fibers and Intermodal Dispersion

Single-mode fiber was designed to have a relatively smaller core compared to multimode fiber, about 8 - 10 μm, to eliminate intermodal dispersion, thus enhancing the capacity and reach of systems deployed with single-mode fiber. Unlike multimode fiber, input optical bit pulses energy propagates in the single-mode fiber core in one mode.

Telecommunication Systems Design and Performance (mid-1980s)

The next generation of systems deployed in the mid-1980s used single-mode fiber and multilongitudinal mode Fabry-Perot lasers in the 1.3 μm wavelength window (the second transmission window) [2]. Transport links typically carried a few hundred megabits per second and required regenerators at intervals of about 40 km [2].

Single Mode Optical Fibers, Loss, and Transmission Windows

Although waiving intermodal dispersion by reducing the core of the optical fiber improved the capacity and reach of fiber optic links, loss in the 1.3 μm wavelength window became a limiting impairment for single-mode systems [2]. While the loss was about 0.5 dB/km in the 1.3 μm wavelength window (second transmission window), it could be reduced to 0.2 dB/km by deploying systems in the 1.55 μm wavelength window (third transmission window), enabling longer spans between regenerators.

Single Mode Optical Fibers and Chromatic Dispersion

Systems deployed in the third transmission window traded low-loss for higher dispersion, limiting increase in transport rates. Indeed, optical signals transported in the 1.55 μm wavelength window were now limited by chromatic dispersion (CD), which is significant in the third transmission window unlike the second transmission window where it is negligible [2].

CD results, at the output of the optical fiber, in a temporal stretch of the input optical bit pulses, because the different frequency components of the pulse, of finite bandwidth, propagate with different velocities in the fiber optic core. Since the magnitude of CD-

induced temporal stretch of input optical bit pulses is proportional to the square of the pulse bandwidth, shorter pulses (larger bandwidth) have less tolerance to CD.

Telecommunication Systems Design and Performance (late 1980s)

In the late 1980s, optical telecommunication systems were deployed in the 1.55 μm wavelength window to leverage the lower window loss, improving the transmission reach between regenerators [2].

The performance limiting CD at 1.55 μm motivated the development of dispersion-shifted fiber (DSF) [2]. DSF is engineered to have zero CD in the third transmission window, enhancing the reach of optical transmission systems in the 1.55 μm wavelength window.

But in the 1980s, optical networks were already deployed with conventional single-mode fiber (non-dispersion shifted fiber). Therefore, solutions to reduce CD in the third transmission window were actively researched. Methods focused on reducing the bandwidth of input optical signals, to minimize the impact of CD, led to the introduction of narrower spectral width lasers, such as the distributed-feedback (DFB) laser [2].

Optical telecommunication systems deployed with single-mode fiber and DFB lasers in the 1.55 μm wavelength window could transport data over 1 Gb/s [2], with signal regeneration every 40 to 80 km.

2.1.3 OPTICAL AMPLIFIERS AND WAVELENGTH DIVISION MULTIPLEXING

Erbium-Doped Fiber Amplifiers

The development of erbium-doped fiber amplifiers (EDFAs) in the late 1980s and early 1990s marked a significant incremental evolution in optical telecommunications [2].

The EDFA consists of a short length (a few meters) of fiber doped with Erbium atoms. When pumped with a high-power laser of a specific wavelength, the Erbium atoms are excited from their ground state to a higher energy level. Incoming photons from an

input optical signal in the 1.55 μm wavelength band experience gain provided by stimulated emission from excited Erbium atoms [2].

EDFAs can not only amplify an incoming optical signal at a given carrier wavelength, thus improve its reach; but it can also amplify signals at many wavelengths simultaneously.

Wavelength Division Multiplexing

The development of EDFAs enabled the deployment of wavelength division multiplexing (WDM) systems [2]. WDM is the technique whereby data channels carried by lasers at neighboring wavelengths are multiplexed onto a single optical fiber. WDM provided another way of increasing the system capacity by using more than one wavelength.

The use of WDM and EDFAs dramatically brought down the cost of long-haul transmission systems and increased their capacity [2].

Telecommunication Systems Design and Performance (mid 1990s)

WDM systems with EDFAs were first deployed in the mid-1990s, and achieved capacities over 1 Tb/s over a single fiber. Simultaneously, transmission bit rates on a single channel reached 10 Gb/s [2].

External Modulators

To further reduce the transmitted spectrum width of optical signals, to lower the impact of CD that became a limiting factor as EDFA enhanced systems reach, external modulators were developed [2].

External modulators are external devices that turn the transmitter laser on and off instead of directly turning the laser on and off (direct modulation).

Using external modulators along with DFB lasers and EDFAs, optical telecommunication systems could achieve distances of ~600 km at 2.5 Gb/s between

regenerators over standard single-mode fiber in the third transmission window [2]. The reach is substantially less at 10 Gb/s.

Fiber Nonlinearities

EDFA-amplified WDM systems saw the emergence of phenomena limiting the uninterrupted improvement of capacity and reach of optical telecommunication networks, such as: nonlinear fiber effects, various polarization-related impairments, and the uneven gain profile of EDFAs [2].

Kerr-induced nonlinear effects such as self-phase modulation (SPM), cross-phase modulation (XPM), and four-wave mixing (FWM), generate interfering signals in the bandwidth of the signal of interest, degrading the quality of the transmission. FWM, for example, consists in the interaction of three optical signals at different wavelengths to create a fourth optical signal at a wavelength that may overlap with one of the optical signals.

Chromatic Dispersion Management

Paradoxically, the higher the CD is, the lower the effect of fiber nonlinearities [2]. Indeed, CD causes optical signals at different wavelengths to propagate at different velocities in the core of the optical fiber. This results in less overlap between the transmitted optical signals, weakening the nonlinear fiber effects. Conversely, propagation of optical signals in DSF resulted in strong nonlinearities, degrading the transmission performances, and therefore limiting the achievable reach of the transmission system.

Trade-offs between CD and fiber nonlinearities increased the complexity of CD management. But it also stimulated the development of new types of single-mode optical fiber [2].

Limiting Chromatic Dispersion

Non-zero dispersion shifted fibers (NZDSF) were engineered to provide less CD than conventional fiber but, at the same time, reduce nonlinearities.

The development of dispersion compensating fiber (DCF), which is an engineered type of fiber that exhibits dispersion opposite effects of the conventional transport fiber, enabled the decrease of the total CD accumulated in the optical signal [2].

Such CD techniques have enabled optical telecommunication systems to achieve distances of several thousand kilometers between regenerators at bit rates as high as 10 Gb/s per channel [2].

Telecommunication Systems Design and Performance (2000s)

WDM systems, EDFAs, and advances in fiber optic network optical elements led in the 2000s, to the deployment of high-capacity amplified terabits/second WDM systems with hundreds of channels at 10 Gb/s, spaced by frequency bands as low as 50 GHz. Distances between electrical regenerators were extended to a few thousand kilometers. In the late 2000s, optical telecommunication networks upgraded to systems operating at 40 Gb/s channel rates.

2.1.4 COHERENT DETECTION AND DIGITAL SIGNAL PROCESSING

Coherent Detection

Coherent detection has improved the transmission SE of fiber optic links by unlocking additional degrees of freedom for encoding of information. Indeed, polarization diverse coherent receivers enabled polarization division multiplexing (PDM) and the retrieval of in-phase and quadrature signals of the electrical field in both orthogonal polarizations, thus making phase, amplitude, and polarization recovery of the received full electrical field a possibility [12]. PDM is a very effective method to double the SE of a transmission system.

With the phase state of the transmitted signal available at the receiver, advanced (phase-based) modulation formats could then be introduced into fiber optic communication systems. Around the turn of the millennium, capacity growth was mainly driven by increase in SE with advanced modulation formats that have progressively been replacing the omnipresent on-off keying (OOK) systems in long-haul applications [13].

Digital Signal Processing

The integration of digital signal processing (DSP) in optical communication systems marked another significant incremental evolution in optical telecommunications.

Continuous development in high-speed electronics, specifically in application-specific integrated circuit (ASIC), have made the advent of DSP a reality for optical communication systems. DSP routines are designed to mitigate transmission impairments, recover polarization multiplexed signals, and subsequently encoded information. Typically, compensated transmission impairments are CD, analog-to-digital converters (ADCs) sampling clock timing error and jitter, polarization mode dispersion (PMD), frequency offset, and carrier phase noise [14]. Nonlinear effects can also be mitigated [15].

Telecommunication Systems Design and Performance (late 2000s – early 2010s)

Coherent detection, and DSP led to the deployment in late 2000s-early 2010s of 100 Gb/s line rates transponders. The next logical step from 100 Gb/s line rates is to either 400 Gb/s or 1 Tb/s rates.

2.1.5 NEXT INCREMENTAL EVOLUTION IN FIBER OPTIC COMMUNICATIONS

Terabit per second channel

To meet the SE requirements of terabit per second channels, coherent optical orthogonal frequency-division multiplexing (CO-OFDM) [16, 17, 18] and coherent WDM

[19] have been proposed. Each technology utilizes coherent, phase-locked subcarriers generated with an optical comb generator [20].

Space-Division Multiplexing

Recent research trends identified space-division multiplexing (SDM) as a promising technology for achieving the next order of magnitude increase in SE in optical networks. Space-dimension multiplexing for fiber systems has been proposed as multi-core fibers [21], few-mode fibers [22, 23, 24], and a combination of both [25]. Challenges for SDM techniques include efficient amplification, channel multiplexing, and multiple-in multiple-out (MIMO) signal processing [26].

Figure 2.1 summarizes the historical evolution of achieved system capacities since the first development of single-mode fibers in the mid-1980s.

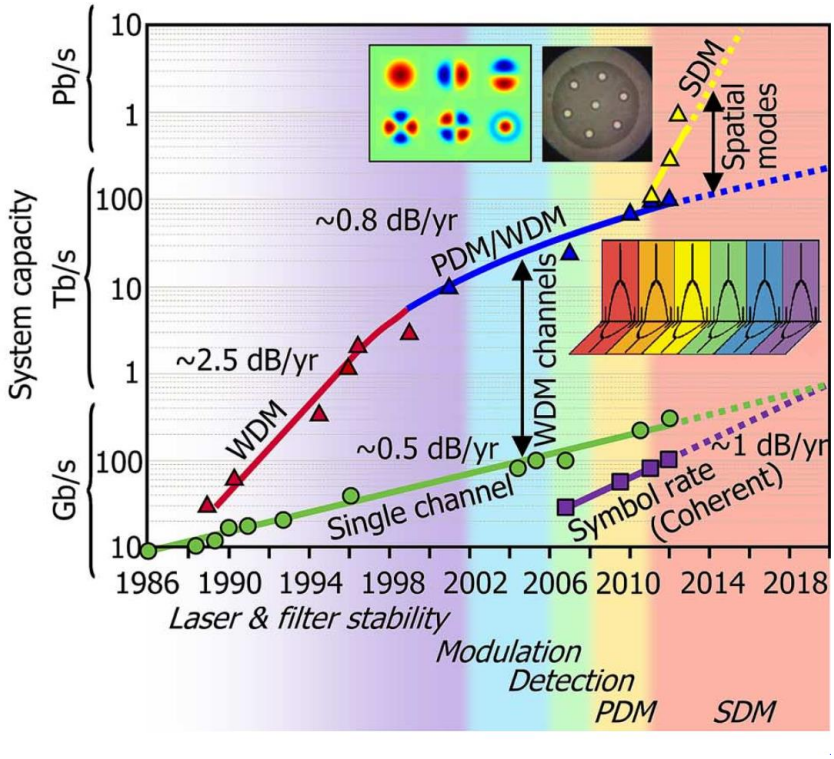

Fig. 2.1. Evolution of experimentally achieved system capacities. Source: [27].
Green circles: single-channel (single-carrier, single-polarization, and electronically multiplexed) bit rates.
Purple squares: symbol rates in digital coherent detection.
Red triangles: aggregate per-fiber capacities using wavelength-division multiplexing (WDM).
Blue triangles: aggregate per-fiber capacities using polarization division multiplexing (PDM).
Yellow triangles: aggregate per-fiber capacities using space-division multiplexing (SDM).

2.2 PROPAGATION OF SIGNALS IN OPTICAL FIBER

2.2.1 OPTICAL FIBER STRUCTURE

An optical fiber is comprised of a cylindrical core surrounded by a cladding, Fig. 2.2.

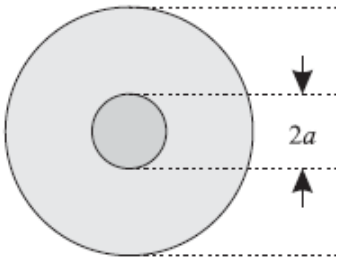

Fig. 2.2. Cross section of an optical fiber showing the core and cladding regions. 2a denotes the diameter of the fiber core. Source: [28].

Glass Optical Fiber

For the majority of optical fibers, both the core and the cladding are made primarily of glass, i.e. silica (SiO_2). The cladding, made of pure silica, has a refractive index which is slightly lower than the refractive index of the core. The index of the cladding may be lowered by injecting impurities such as fluorine (F_2O_3) or boron (B_2O_3). The refractive index of the core is increased by doping the silica with impurities such as germanium (GeO2, germanosilicate), phosphorus (P_2O_5, phosphosilicate), and aluminium (Al_2O_3, aluminosilicate). The resulting higher refractive index of the core enables light to be guided by the core, and thus propagate through the fiber [28].

Plastic Optical Fiber

For short distance and low data rate transmission systems, plastic optical fibers can be used. Compared to glass optical fibers, plastic optical fibers are less costly to

manufacture, and flexible. Conversely, glass optical fibers are used for long distance and high data rate transmission systems [29].

Optical fibers can usually be segmented in two mutually exclusive categories: multimode fibers and single mode fibers. Plastic optical fibers are mostly multimode whereas glass optical fibers can be either single mode or multimode. Multiple systems design parameters affect the choice of type of fibers suited for a particular application, among these parameters: cost, reach, capacity, ease of installation…

Multimode Fiber

Multimode fibers have core diameters much larger than the wavelength of light that propagates within (core diameters of ~50 - 85 μm). Consequently, a simple geometrical optics approach can be used to describe the overall behavior of light propagation in multimode fibers [28]. Since the core diameter is larger than the wavelength of the optical carrier, intermodal dispersion occurs. Multimode fibers carry hundreds of modes, which can be thought of as independently propagating paths of the optical signal [28]. Intermodal dispersion limits considerably the reach of multimode fiber systems. Intermodal dispersion results, at the output of the optical fiber, in a spatiotemporal stretch of the input optical bit pulses, because the optical signal energy propagates in the optical waveguide by taking simultaneously different optical paths, or modes, of different propagation time.

Single Mode Fiber

Single mode fibers have core diameters on the same scale as the wavelength of light that propagates within [28]. This restricts the light to propagate in a single fundamental spatial core [28], thus eliminating intermodal dispersion, and improving the reach and capacity of optical fiber links. Since single mode fiber core is on the same scale as the wavelength of light that propagates within, the simple geometrical optics approach does not suffice to describe the overall behavior of light propagation in single mode fibers. An

electromagnetism-based wave theory approach is rather used to understand light propagation in single mode optical fibers [28].

2.2.2 GEOMETRICAL OPTICS APPROACH

In the geometrical optics approach, light can be considered as consisting of a number of light rays propagating in straight lines within a medium and getting reflected and/or refracted at the interfaces between two materials [28].

Because multimode fibers have core diameters much larger than the wavelength of light that propagates within (core diameters of ~ 50 - 85 μm), a simple geometrical optics approach can be used to describe the overall behavior of light propagation in multimode fibers

Geometrical Optics Laws

Consider a light ray which is incident on the interface between two media of refractive index n_1 and n_2, Fig. 2.3.

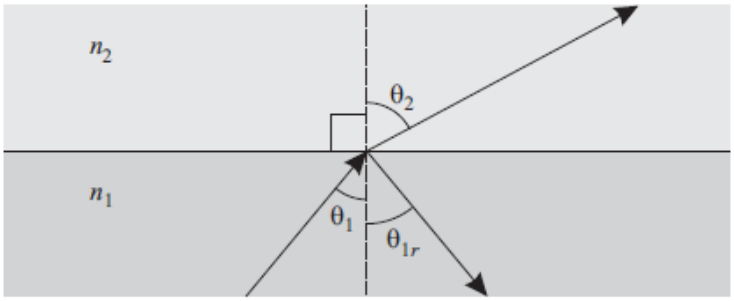

Fig. 2.3. Reflection and refraction of light rays at the interface between two media. Source: [28].

The light ray from medium 1, of refractive index n_1, is incident on the interface between medium 1 and medium 2, of refractive index n_2 [28]. We assume that $n_1 > n_2$. The angle of incidence is the angle between the incident ray and the normal to the interface between the two media, denoted by θ_1 [28]. Part of the energy is reflected into medium 1

as a reflected ray, and the remainder passes into medium 2 as a refracted ray [28]. The angle of reflection θ_{1r} is the angle between the reflected ray and the normal to the interface [28]. Similarly, the angle of refraction θ_2 is the angle between the refracted ray and the normal [28].

The laws of geometrical optics state that:

$$\theta_{1r} = \theta_1$$

$$n_1.\sin(\theta_1) = n_2.\sin(\theta_2) \qquad \text{(Snell-Descartes' law)}$$

For $\theta_1 > \theta_c = \arcsin(n_2/n_1)$, there is no refracted ray. All the energy from the incident ray is reflected. This phenomenon is called total internal reflection [28]. The smallest angle of incidence for which we get total internal reflection is called the critical angle $\theta_c = \arcsin(n_2/n_1)$ [28].

Ray Propagation in Optical Fibers

From the geometrical optics point of view, light propagates in optical fiber due to a series of total internal reflections that occur at the core-cladding interface [28].

Let medium 1, of refractive index n_1, be the optical fiber core. Let medium 2, of refractive index n_2, be the optical fiber cladding, Fig. 2.4. We have $n_1 > n_2$.

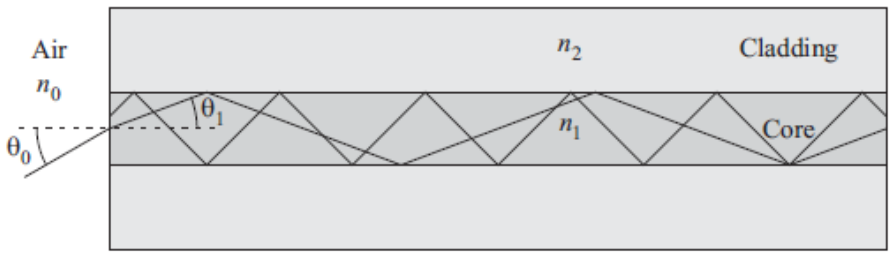

Fig. 2.4. Propagation of light rays in optical fiber by total internal reflection. Source: [28].

Total internal reflection occurs if the angle of incidence θ_1 on the interface between the core and the cladding is strictly greater than the critical angle $\theta_c = \arcsin(n_2/n_1)$ [28]:

$$\theta_1 > \theta_c.$$

Using geometrical optics laws, we have at the air-core interface:

$$n_0.\sin(\theta_0) = n_1.\sin(\theta_1)$$

Where n_0 is the refractive index of air. Combining the previous inequality and equation, we obtain that only light rays that are incident at the air-core interface at an angle $\theta_0 < \theta_{max} = \arcsin(\frac{\sqrt{{n_1}^2-{n_2}^2}}{n_0})$ will undergo total internal reflection at the subsequent care-cladding interfaces, and will therefore propagate in the optical fiber core. Such light rays are called guided rays [28].

Numerical Aperture

The numerical aperture (NA) of the optical fiber is defined as:

$$NA = \sin(\theta_{max}) = \frac{\sqrt{{n_1}^2-{n_2}^2}}{n_0}$$

And θ_{max} is called the acceptance angle.

If the incident light ray at the air-core interface is within the cone $\theta_0 < \theta_{max}$, it will be guided through the fiber. Else, it will vanish to the cladding and information carried by the light ray will not be received at the output of the optical fiber.

Intermodal Dispersion

When the core diameter is larger than the wavelength of the optical carrier, which is the case for multimode fibers, the optical fiber supports multiple guided modes. This phenomenon is known as intermodal dispersion, and limits considerably the reach of multimode fiber systems. Intermodal dispersion results, at the output of the optical fiber, in a spatiotemporal stretch of the input optical bit pulses, because the optical signal energy propagates in the optical waveguide by taking simultaneously different optical paths, or modes, of different propagation time.

2.2.3 WAVE THEORY APPROACH

Intermodal dispersion can be eliminated by reducing the optical fiber core diameter to the order of the wavelength of the optical carrier. This restricts the light to propagate in a single fundamental spatial core. These optical fibers are called single mode fibers. Since single mode fibers cores are on the same scale as the wavelength of light that propagates within, the simple geometrical optics approach does not suffice to describe the overall behavior of light propagation in single mode fibers. Light being an electromagnetic wave, an electromagnetism-based wave theory approach is rather used to understand light propagation in single mode optical fibers.

The propagation of light can be described by specifying the evolution of the associated electric and magnetic field vectors in space and time, denoted by $\vec{E}$ and $\vec{H}$ respectively [28].

Coulomb's Law

According to Coulomb's law, the force between two electric charges q_1 and q_2 separated in a medium is directly proportional to the product of the electric charges and inversely proportional to the square of the distance r between them. The force is repulsive if the electric charges have the same sign, but attractive if the electric charges are of opposite sign. Specifically, the force F_2 on the electric charge q_2 is given by [30]:

$$\vec{F}_2 = \frac{q_1 q_2}{4\pi\varepsilon r^2}\vec{u}_{12}$$

Where $\vec{u}_{12}$ is a unit vector in the direction of the vector pointing from electric charge q_1 to electric charge q_2, and ε is the permittivity which depends on the medium in which the electric charges are placed.

The electric charge q_1 generates an electric field $\vec{E}$ at any point in space located at a distance r from the electric charge q_1 [30]:

$$\vec{E} = \frac{q_1}{4\pi\varepsilon r^2}\vec{u}_{12}$$

Where $\vec{u}_{12}$ is a unit vector in the direction of the vector pointing from electric charge q_1 to the point in space of interest located at a distance r from the electric charge q_1.

Thus, we can express the force F_2 on the electric charge q_2 as a function of the electric field generated by the electric charge q_1 [30]:

$$\vec{F}_2 = q_2\vec{E}$$

The expression above shows that the electric field $\vec{E}$ is defined as the force on a positive unit electric charge q_2 = 1 C.

Gauss' Law

When an electric field is applied to a material, the forces experienced by the nuclei (positive electric charge) and the electrons (negative electric charge) are in opposite directions [28]. These forces result in the atoms being polarized. The induced electric polarization of the material, or dielectric polarization, can be described by a vector $\vec{P}$, which depends both on the material properties and the applied field [28]. The dielectric polarization can be viewed as the response of the medium to the applied electric field [28]. The electric flux density $\vec{D}$ is defined as:

$$\vec{D} = \varepsilon_0\vec{E} + \vec{P} = \varepsilon\vec{E}$$

Where $\varepsilon_0$the permittivity of vacuum and ε is the permittivity of the medium.

According to Gauss' law, the total electric flux passing through a closed surface S of a volume V is equal to the electric charge enclosed by the volume [30]:

$$\oiint_S \vec{D}\,.\,d\vec{S} = Q_V$$

Where $d\vec{S}$ is an element of surface of the chosen closed surface S of a volume V, and Q_V is the total electric charge enclosed by the volume V.

If the chosen volume V is only comprised of discrete electric charges, we simply have:

$$Q_V = \sum_i q_{i,V}$$

Where $q_{i,V}$ is the i[th] discrete electric charge contained in the volume V.

If the chosen volume V comprises electric charges that are distributed in a volume, we rather use the volume electric charge density ρ, such that $Q_V = \iiint_V \rho . dV$, and utilize the differential form of Gauss' law:

$$div\, \vec{D} = \rho$$

Green-Ostrogradsky's theorem can be used to relate the total electric flux passing through the closed surface S of a volume V to the volume integral of the divergence of the electric flux density over the volume V:

$$\oiint_S \vec{D} . d\vec{S} = \iiint_V div\, \vec{D} . dV$$

Where dV is an element of volume of the chosen volume V of total surface S.

Ampere's Law

Similar to the fact that the electric field $\vec{E}$ is defined as the force on a positive unit electric charge, the magnetic field $\vec{H}$ is defined as the force on a positive magnetic charge [30] .

According to Ampere's law, the line integral of the magnetic field about any closed path C of surface S is equal by the direct current enclosed by that path [30]:

$$\oint_C \vec{H} . d\vec{l} = I_S$$

Where $d\vec{l}$ is an element of length of the chosen closed path C of surface S, and I_S is the direct current flowing through the surface S enclosed by the closed path C.

Ampere's law is a relation between the total amount of magnetic field around any closed path C of surface S due to the direct current which passes through that enclosed path.

If the chosen closed path C is only comprised of discrete direct currents, we simply have:

$$I_S = \sum_i i_{i,S}$$

Where $i_{i,S}$ is the i[th] discrete direct current flowing through the surface S enclosed by the closed path C.

If the chosen closed path C of surface S is comprised of direct currents that are distributed in a surface, we rather use the current density $\vec{j}$, which is a vector with its direction given by the direction of the current, such that $I_S = \iint_S \vec{j} \,.\, d\vec{S}$, and we rather utilize the differential form of Ampere's law:

$$\overrightarrow{curl}\, \vec{H} = \vec{j}$$

Kelvin-Stokes theorem can be used to relate the line integral of the magnetic field about any closed path C of surface S to the surface integral of the curl of the magnetic field over the surface S:

$$\oint_C \vec{H} . d\vec{l} = \iint_S \overrightarrow{curl}\, \vec{H} \,.\, d\vec{S}$$

Where $d\vec{S}$ is an element of surface of the chosen surface S associated to the closed path C.

In analogy with the definition of electric flux density $\vec{D}$, magnetic flux density $\vec{B}$ is defined as [28]:

$$\vec{B} = \mu_0(\vec{H} + \vec{M}) = \mu\vec{H}$$

Where μ_0 is the permeability of vacuum, $\vec{M}$ is the magnetic polarization of the medium, and μ is the permeability of the medium.

An isolated magnetic charge does not exist without the existence of an associated counterpart of magnetic charge of the opposite sign [30]. Because magnetic flux lines are closed and do not emerge from or terminate on magnetic charges, unlike electric flux lines

which can start or terminate on electric charges, the magnetic flux density integrated over a closed surface is null [30]:

$$div\,\vec{B} = 0$$

Faraday's Law

Faraday's work concluded that a time-varying magnetic field produces an electromotive force which is responsible for a current in a closed circuit [30]. The electromotive force is the voltage developed in the closed circuit as the result of the circulation of the electric field (induced by the time-varying magnetic field) around the closed circuit [30]. The induced electric field forces the electrons to move in a particular direction leading to a current [30].

According to Faraday's law, the electromotive force about a closed path C of surface S is equal to the opposite time rate of change of the magnetic flux crossing the surface S [30]:

$$\oint_C \vec{E}.d\vec{l} = -\frac{d}{dt}\iint_S \vec{B}\,.d\vec{S} = -\iint_S \frac{\partial\vec{B}}{\partial t}.d\vec{S}$$

Where $d\vec{S}$ is an element of surface of the chosen surface S associated to the closed path C.

Using Kelvin-Stokes theorem, we obtain Faraday's law in the differential form:

$$\overrightarrow{curl}\,\vec{E} = -\frac{\partial\vec{B}}{\partial t}$$

From Faraday's law, we see that if the magnetic field changes with time, it induces an electric field. Owing to symmetry, time-changing electric field induces a magnetic field [30]. This leads us to add an additional term in Ampere's law, to account for the induction of a magnetic field as a result of a time-varying electric field. We obtain the complete Ampere's law under its differential form:

$$\overrightarrow{curl}\,\vec{H} = \vec{j} + \frac{\partial\vec{D}}{\partial t}$$

Maxwell's Equations

The propagation of electromagnetic waves is governed by the following Maxwell's equations:

$$div\,\vec{D} = \rho$$

$$div\,\vec{B} = 0$$

$$\overrightarrow{curl}\,\vec{E} = -\frac{\partial \vec{B}}{\partial t}$$

$$\overrightarrow{curl}\,\vec{H} = \vec{j} + \frac{\partial \vec{D}}{\partial t}$$

Where ρ is the volume electric charge density, and $\vec{j}$ is the current density.

Wave Equations

In optical fiber communications, the medium in which light propagates is primarily made of silica. We assume that there are no free charges in the medium such that the volume electric charge density $\rho = 0$ [31]. The conductivity of silica is very small thus we can assume that $\vec{j} = \vec{0}$ [31]. Since silica is a nonmagnetic material, we set the magnetic polarization of the medium $\vec{M} = \vec{0}$ [31]. Maxwell's equations can be simplified as:

$$div\,\vec{D} = 0$$

$$div\,\vec{B} = 0$$

$$\overrightarrow{curl}\,\vec{E} = -\frac{\partial \vec{B}}{\partial t}$$

$$\overrightarrow{curl}\,\vec{H} = \frac{\partial \vec{D}}{\partial t}$$

Where the electric flux density $\vec{D} = \varepsilon_0 \vec{E} + \vec{P}$, the magnetic flux density $\vec{B} = \mu_0 \vec{H}$, and with $\vec{P}$ the electric polarization of the material.

Therefore, we have:

$$\overrightarrow{curl}\,\overrightarrow{curl}\,\vec{E} = -\mu_0 \varepsilon_0 \frac{\partial^2 \vec{E}}{\partial t^2} - \mu_0 \frac{\partial^2 \vec{P}}{\partial t^2}$$

Let $\vec{\tilde{E}}$ and $\vec{\tilde{P}}$ be the Fourier transforms of the electric field $\vec{E}$ and the electric polarization of the material $\vec{P}$ respectively.

By definition, we have:

$$\vec{\tilde{E}}(\vec{r},\omega) = \int \vec{E}(\vec{r},t)\exp(i\omega t)\,dt$$

Taking the Fourier transform of the equation, we obtain:

$$\overrightarrow{curl}\,\overrightarrow{curl}\,\vec{\tilde{E}} = \mu_0\varepsilon_0\omega^2\vec{\tilde{E}} + \mu_0\omega^2\vec{\tilde{P}}$$

Where ω is the angular frequency.

Assuming that the core and the cladding regions of the silica fiber are locally responsive, isotropic, linear, homogeneous, and lossless (although silica fiber is certainly not lossless, the loss is negligible and can be assumed to be zero in the discussion of propagation modes), we obtain the following relationship between the electric polarization of the material $\vec{P}$ the electric field $\vec{E}$ [28]:

$$\vec{P}(\vec{r},t) = \varepsilon_0\chi(t) * \vec{E}(\vec{r},t) = \varepsilon_0\int_{-\infty}^{t}\chi(t-\tau)\,\vec{E}(\vec{r},\tau)d\tau$$

Where χ is called the susceptibility of the medium.

Noting $\tilde{\chi}$ the Fourier transforms of the susceptibility χ, we obtain the simple following relationship between $\vec{\tilde{E}}$ and $\vec{\tilde{P}}$:

$$\vec{\tilde{P}}(\vec{r},\omega) = \varepsilon_0\tilde{\chi}(\omega)\vec{\tilde{E}}(\vec{r},\omega)$$

Substituting $\vec{\tilde{P}}$, we obtain the following equation:

$$\overrightarrow{curl}\,\overrightarrow{curl}\,\vec{\tilde{E}} = \mu_0\varepsilon_0\omega^2\vec{\tilde{E}} + \mu_0\varepsilon_0\omega^2\tilde{\chi}\vec{\tilde{E}}$$

We note $c = \frac{1}{\sqrt{\mu_0\varepsilon_0}}$, the speed of light in the vacuum, and $n^2(\omega) = 1 + \tilde{\chi}(\omega)$, the refractive index of the material [28]. Therefore, we obtain:

$$\overrightarrow{curl}\,\overrightarrow{curl}\,\vec{\tilde{E}} = \frac{\omega^2 n^2}{c^2}\vec{\tilde{E}}$$

The left-hand side of the equation can be expanded as:

$$\overrightarrow{curl}\,\overrightarrow{curl}\,\vec{\tilde{E}} = \overrightarrow{grad}\left(div\vec{\tilde{E}}\right) - \Delta\vec{\tilde{E}}$$

Where Δ is the Laplace operator. In Cartesian coordinates, we have for any vector $\vec{u}$:

$$\Delta\vec{u} = (\Delta u_x, \Delta u_y, \Delta u_z)^T, \text{ with } \Delta u_x = \frac{\partial^2 u_x}{\partial x^2} + \frac{\partial^2 u_x}{\partial y^2} + \frac{\partial^2 u_x}{\partial z^2}.$$

Because of our assumption of homogenous medium, we obtain [31]:

$$0 = div\left[\overrightarrow{\tilde{D}}(\vec{r},\omega)\right] = div\left[\varepsilon_0\vec{\tilde{E}}(\vec{r},\omega) + \vec{\tilde{P}}(\vec{r},\omega)\right] = div\left[\varepsilon_0\big(1+\tilde{\chi}(\omega)\big)\vec{\tilde{E}}(\vec{r},\omega)\right]$$

$$= \varepsilon_0\big(1+\tilde{\chi}(\omega)\big)div\left[\vec{\tilde{E}}(\vec{r},\omega)\right]$$

Where $\overrightarrow{\tilde{D}}$ is the Fourier transform of the electric flux density. This leads to: $div\left[\vec{\tilde{E}}(\vec{r},\omega)\right] = 0$.

Finally, we obtain the following wave equation for the Fourier transform $\vec{\tilde{E}}$ of the electric field $\vec{E}$:

$$\frac{\omega^2 n^2}{c^2}\vec{\tilde{E}} = -\Delta\vec{\tilde{E}}$$

Which can be rewritten as:

$$\Delta\vec{\tilde{E}} + \frac{\omega^2 n^2}{c^2}\vec{\tilde{E}} = 0$$

Following similar steps, the following wave equation for the Fourier transform $\vec{\tilde{H}}$ of the magnetic field $\vec{H}$ can be derived [31]:

$$\Delta\vec{\tilde{H}} + \frac{\omega^2 n^2}{c^2}\vec{\tilde{H}} = 0$$

The wave equations are second-order, linear, partial differential equations for the Fourier transforms of the electric and magnetic field vectors [28].

2.2.4 OPTICAL FIBER AS A WAVEGUIDE

To understand the electromagnetic field propagation in optical fibers, Maxwell equations must be solved with the condition that the tangential components of electric and magnetic fields should be continuous at the interface between the fiber core and cladding

[29]. Every pair of solutions to the wave equations that satisfies the boundary conditions is a fiber mode [28]. Fiber modes can be considered as one possible path that a guided light ray can take to propagate in the optical fiber. Because the path lengths are different, the propagation speeds of the modes are different.

The wave equations can be generalized as [29]:

$$\Delta\Psi + \frac{n^2}{c^2}\frac{\partial^2\Psi}{\partial t^2} = 0$$

Where Ψ is any one of the components E_x, E_y, E_z, H_x, H_y, H_z.

The parameter c/n is the speed of light in the medium of refractive index n.

General Solutions to Wave Equations

Detailed works on the propagation modes in optical fiber [29] provide key results on the solutions to the wave equations. Specifically, when the output of a continuous wave laser operating at the angular frequency ω is incident on a single mode optical fiber, the optical field distribution, solution to the generalized wave equation, which propagates along the +z axis, can be written as [29]:

$$\Psi(x, y, z, t) = \Phi(x, y, \omega)A(\omega)\exp \mathrm{i}[\omega t - \beta(\omega)z]$$

Where A is the mode weight factor, Φ is the transverse field distribution, and β is the propagation constant. In the presence of fiber loss, the propagation constant satisfies [29]:

$$\beta(\omega) = \beta_r(\omega) + i\alpha(\omega)/2$$

Where β_r is the real part of β and α is the attenuation coefficient in units of km^{-1}.

The optical field distribution can be rewritten as [29]:

$$\Psi(x, y, z, t) = \Phi(x, y, \omega).A(\omega).\exp(-\alpha z/2).\exp \mathrm{i}[\omega t - \beta_r(\omega)z]$$

$\Phi(x, y, \omega)$ represents the transverse distribution of the optical field distribution, $A(\omega).\exp(-\alpha z/2)$ represents the field envelope, and the term $\exp \mathrm{i}[\omega t - \beta_r(\omega)z]$ represents the optical carrier [29].

Each fiber mode has a different associated propagation constant real part $\beta_r(\omega)$. The fiber modes propagate partly in the cladding and partly in the core, and thus the real part of their propagation constants $\beta_r(\omega)$ satisfies: $k_0.n_2 < \beta_r(\omega) < k_0.n_1$ [28].

Where k_0 is the wavenumber in the vacuum and is giver by: $k_0 = 2\pi/\lambda_0 = \omega/c$. And λ_0 is the wavelength of the light in the vacuum.

In general, the wavenumber in a medium of refractive index n is given by: $k = 2\pi n/\lambda_0 = 2\pi/\lambda = \omega n/c$, with $\lambda = \lambda_0/n$ the wavelength of the light in the medium of refractive index n.

The number of guided modes supported by an optical fiber can be calculated using a specific design parameter called the normalized frequency V. For a step-index fiber of refractive index n_1 in the core and n_2 in the cladding (with $n_1 > n_2$), with a core radius a, we have the following expression for the normalized frequency V [28, 29]:

$$V = \frac{2\pi a}{\lambda}\sqrt{{n_1}^2 - {n_2}^2}$$

Where λ is the wavelength.

In order for a fiber to be single moded at the wavelength λ, the normalized frequency V must satisfy the following condition [28, 29]:

$$V \leq 2.4048$$

In this condition, the optical fiber supports only the LP_{01} mode [29]. And the smallest λ for which a given fiber is single moded is called the cutoff wavelength, and is denoted λ_{cutoff} [28]. For any $\lambda \geq \lambda_{cutoff}$, the optical fiber remains single moded at the wavelength λ. Conversely, for any $\lambda < \lambda_{cutoff}$, the optical fiber will not be single moded at the wavelength λ.

Pulse Propagation in Single Mode Fiber

A monochromatic light wave of infinite duration contains only one frequency component, and propagates according to a single ray path. However, such an optical signal does not carry any information [29]. To transmit information over optical fiber, the optical

carrier has to be modulated. Therefore, the optical signal propagating in the fiber contains of a range of frequency components [29]. Since the propagation constant β is frequency dependent, different frequency components undergo different amounts of delay and arrive at different times at the receiver, leading to pulse broadening [29]. This phenomenon is known as intermodal dispersion.

The propagation constant real part $\beta_r(\omega)$ can be approximated by a Taylor series expansion [29]:

$$\beta_r(\omega) \sim \beta_0 + \beta_1(\omega - \omega_0) + \frac{1}{2}\beta_2(\omega - \omega_0)^2 + \frac{1}{6}\beta_3(\omega - \omega_0)^3$$

Where: $\boldsymbol{\beta_0} = \boldsymbol{\beta_r}(\boldsymbol{\omega_0})$, $\boldsymbol{\beta_1} = \frac{\partial \beta_r}{\partial \omega}(\boldsymbol{\omega_0})$, $\boldsymbol{\beta_2} = \frac{\partial^2 \beta_r}{\partial \omega^2}(\boldsymbol{\omega_0})$, and $\boldsymbol{\beta_3} = \frac{\partial^3 \beta_r}{\partial \omega^3}(\boldsymbol{\omega_0})$.

β_1 is the inverse group velocity which simply causes the optical pulse to be delayed at the fiber output without any change in pulse shape [29]. β_2 is the second order dispersion coefficient and is an important parameters that determines the extent of pulse spreading as the optical signal propagates in the fiber [29]. β_3 is the third order dispersion coefficient and plays a significant role when the second order dispersion coefficient β_2 is null (dispersion-free optical fiber).

The parameters β_2 and β_3 are critical for fiber optic system design.

2.2.5 LOSS AND TRANSMISSION WINDOWS

Loss and Transmission Windows in Optical Fiber

Loss in optical fiber limits the transmission distance between amplifiers or repeaters. The light wave that propagates in the fiber is mainly attenuated due to Rayleigh scattering and material absorption [29].

Rayleigh scattering is the scattering of light by atoms or molecules of size much smaller than the wavelength of the incident light [29].

Material absorption can be segmented in two mutually exclusive types: intrinsic absorption and extrinsic absorption [29]. Intrinsic absorption is caused by the interaction of light with pure silica. Intrinsic absorption results from the fundamental properties of silica [29]. Intrinsic absorption is wavelength dependent and it is about 0.2 dB/km in the vicinity of the C-band. Extrinsic absorption is caused by the interaction of light with impurities in the optical fiber [29].

Other types of loss such as bending losses or fiber splicing operations also affect the overall attenuation of the propagating optical signal in the fiber.

Fig. 2.5 illustrates the measured loss spectrum of a conventional optical fiber and exhibits the principal transmission windows in fiber optic communications.

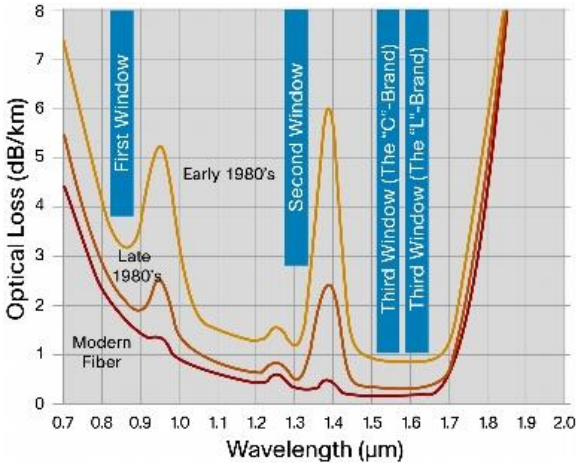

Fig. 2.5. Measured loss spectrum of optical fiber and principal transmission windows in fiber optic communications. Source: [11].

Normalized Loss Parameter

The input optical power P_{in} and output optical power P_{out} level difference after transmitting through a fiber of loss α and distance L is specified by [29]:

$$Loss(dB) = 10log_{10}(\frac{P_{in}}{P_{out}})$$

We have seen that the optical field distribution of the output of a continuous wave laser operating at the angular frequency ω, incident on a single mode optical fiber, which propagates along the +z axis, can be written as:

$$\Psi(x, y, z, t) = \Phi(x, y, \omega).A(\omega).\exp(-\alpha z/2).\exp \mathrm{i}[\omega t - \beta_r(\omega)z]$$

Where α is the attenuation coefficient in units of km^{-1}.

Thus, the optical power, which propagates along the +z axis, can be expressed as [29]:

$$P(z) = |A(\omega).\exp(-\alpha z/2)|^{2}$$

Consequently, at the fiber input (z=0), we have the following expression for the optical power:

$$P_{in} = P(z = 0) = |A(\omega)|^{2}$$

And at the fiber output (z=L), we have the following expression for the optical power:

$$P_{out} = P(z = L) = |A(\omega).\exp(-\alpha L/2)|^{2}$$

Therefore, we can express the fiber loss in dB as a function of the parameter α, which is the attenuation coefficient in units of km^{-1} [29]:

$$Loss(dB) = 10.\alpha.L.log_{10}(e) = 4.343.\alpha.L$$

The normalized loss parameter $\alpha(dB/km)$ in dB/km, is given by [29]:

$$\alpha(dB/km) = 4.343\alpha$$

The normalized loss parameter $\alpha(dB/km)$ is a critical parameter for fiber optic system design. Is it about 0.2 dB/km in the vicinity of the C-band.

2.2.6 INTERMODAL DISPERSION

When the core diameter of the optical fiber is larger than the wavelength of the optical carrier, which is the case for multimode fibers, the optical fiber supports multiple guided modes. This phenomenon is known as intermodal dispersion, and limits considerably the reach of multimode fiber systems. Intermodal dispersion results, at the

output of the optical fiber, in a spatiotemporal stretch of the input optical bit pulses, because the optical signal energy propagates in the optical waveguide by taking simultaneously different optical paths, or modes, of different propagation time.

2.2.7 INTRAMODAL DISPERSION

To transmit information over optical fiber, the optical carrier has to be modulated. Therefore, the optical signal propagating in the fiber contains of a range of frequency components [29]. Since the propagation constant β is frequency dependent, different frequency components undergo different amounts of delay and arrive at different times at the receiver, leading to pulse broadening [29]. This phenomenon is known as intermodal dispersion.

2.2.8 CHROMATIC DISPERSION

CD is the term given to the phenomenon by which different spectral components of a pulse travel at different velocities [28]. The effect of CD can be understood through the significance of the propagation constant $\beta(\omega)$ [28]. We restrict our discussion to single mode fiber. Indeed, in the case of multimode fiber, the effects of intermodal dispersion usually overshadow those of CD [28]. So the propagation constant in our discussions will be that associated with the fundamental mode (LP_{01} guided mode) of the optical fiber.

Let us recall that the real part of the propagation constant can be approximated by a Taylor series expansion [29]:

$$\beta_r(\omega) \sim \beta_0 + \beta_1(\omega - \omega_0) + \frac{1}{2}\beta_2(\omega - \omega_0)^2 + \frac{1}{6}\beta_3(\omega - \omega_0)^3$$

Where: $\boldsymbol{\beta_0} = \boldsymbol{\beta_r}(\boldsymbol{\omega_0})$, $\boldsymbol{\beta_1} = \frac{\partial \beta_r}{\partial \omega}(\boldsymbol{\omega_0})$, $\boldsymbol{\beta_2} = \frac{\partial^2 \beta_r}{\partial \omega^2}(\boldsymbol{\omega_0})$, and $\boldsymbol{\beta_3} = \frac{\partial^3 \beta_r}{\partial \omega^3}(\boldsymbol{\omega_0})$.

β_1 is the inverse group velocity which simply causes the optical pulse to be delayed at the fiber output without any change in pulse shape [29]. β_2 is the second order dispersion coefficient and is an important parameters that determines the extent of pulse spreading as

the optical signal propagates in the fiber [29]. β_3 is the third order dispersion coefficient and plays a significant role when the second order dispersion coefficient β_2 is null (dispersion-free optical fiber).

A medium is dispersive if the group velocity of light changes with the frequency of the optical wave [29]. In other terms, a medium is dispersive if the first order dispersion coefficient β_1 is a function of the angular frequency ω (or the wavelength λ).

Fiber optic system design conventions use the dispersion parameter D, which is proportional to the second order dispersion coefficient β_2, and is defined as:

$$D = \frac{-2\pi c}{\lambda^2}\,\beta_2 = \frac{-2\pi c}{\lambda^2}\,\frac{\partial^2 \beta_r}{\partial \omega^2}\,(\omega_0)$$

The product DL between the dispersion parameter D and the optical fiber length L is called the total accumulated CD, and represents the total amount of CD applied to the propagating optical pulse at the output of the fiber.

CD arises for two reasons: material dispersion and waveguide dispersion [28].

Material dispersion is due to the dispersive nature of the transmission medium, silica [28]. The refractive index of silica is frequency dependent, thus different frequency components travel at different speeds in silica [28].

Waveguide dispersion result from the refractive index profile of the optical fiber [29]. With the example of the step-index optical fiber, we have seen that the light energy of a mode propagates partly in the fiber core and partly in the cladding [28]. And we have seen that the power distribution of a mode between the core and the cladding of the fiber is a function of the wavelength [28]. Consequently, the propagation of the light energy of a mode is a function of the frequency of the optical wave [28].

2.2.9 POLARIZATION MODE DISPERSION

<u>General Solutions to Wave Equations and Polarization Modes</u>

When considering the polarized nature of light while solving the generalized wave equations, it cab be shown that the electric fields associated with the fundamental mode can effectively be assumed to be transverse and linearly polarized [28]. Specifically, when the output of a continuous wave laser operating at the angular frequency ω is incident on a single mode optical fiber, the two possible, independent (and degenerate) propagation modes for the electric field, noted $\overrightarrow{E_x}$ and $\overrightarrow{E_y}$, associated with the fundamental mode, propagating along the +z axis, can be written as:

$$\begin{cases} \overrightarrow{E_x}(x,y,z,t) = E_x(x,y,\omega).A_x(\omega).\exp(-\alpha z/2).\exp \mathrm{i}[\omega t - \beta_r(\omega)z]\,\overrightarrow{e_x} \\ \overrightarrow{E_y}(x,y,z,t) = E_y(x,y,\omega).A_y(\omega).\exp(-\alpha z/2).\exp \mathrm{i}[\omega t - \beta_r(\omega)z]\,\overrightarrow{e_y} \end{cases}$$

Where $\overrightarrow{e_x}$ ($\overrightarrow{e_y}$) is the unit vector of the +x (y) axis, $E_x(x,y,\omega)$ ($E_y(x,y,\omega)$) represents the transverse distribution of the electric field $\overrightarrow{E_x}$ ($\overrightarrow{E_y}$), $A_x(\omega).\exp(-\alpha z/2)$ ($A_y(\omega).\exp(-\alpha z/2)$) represents the $\overrightarrow{E_x}$ ($\overrightarrow{E_y}$) field envelope, and the term $\exp \mathrm{i}[\omega t - \beta_r(\omega)z]$ represents the optical carrier.

The two linearly independent solutions of the wave equations for the electric field are linearly polarized along the x and y directions. Since these two directions are perpendicular to each other, the two solutions are said to be orthogonally polarized [28]. Each solution is qualified as a polarization mode.

The state of polarization (SOP) refers to the distribution of light energy among the two polarization modes [28]. The fiber is still termed single mode because these two polarization modes are degenerate. Indeed, both polarization modes have the same propagation constant $\beta(\omega)$, at least in an ideal, perfectly circularly symmetric fiber [28].

In practical optical fiber systems, the fiber is not perfectly circular. PMD is a linear impairment which describes the pulse broadening and distortion caused by the fiber birefringence properties. PMD is a critical polarization dependent penalty in high data rate long haul transmission systems. PMD is characterized by the differential group delay (DGD) between the two principle SOP.

If we note $\beta_{x,r}(\omega)$ ($\beta_{y,r}(\omega)$) the real part of the propagation constant of the polarization mode $\overrightarrow{E_x}$ ($\overrightarrow{E_y}$), then the time spread $\Delta\tau_{\ DGD}(\omega)$, or DGD, due to PMD after the pulse has propagated through a unit length of fiber is given by:

$$\Delta\tau_{\ DGD}(\omega) = \frac{\Delta\beta_r(\omega)}{\omega} = \frac{|\beta_{x,r}(\omega) - \beta_{y,r}(\omega)|}{\omega}$$

2.2.10 POLARIZATION DEPENDENT LOSS

Polarization dependent loss (PDL) is another critical polarization dependent, linear impairment, in high data rate long haul transmission systems. PDL arises from the polarization dependent nature of the optical components such as the optical fiber, optical amplifiers, attenuators, and filters. It causes imbalance between the two polarization tributes and degrades the optical signal-to-noise ratio (OSNR). For a fixed PDL value, the system penalty varies dramatically because the orientation of the arrived polarization is arbitrary, and because of the interaction between PDL and fiber nonlinear effects.

2.2.11 NONLINEAR EFFECTS

SPM, XPM, and FWM are the primary nonlinear effects in optical fibers. The fundamental understanding of those nonlinear effects necessitates the investigation of the wave propagation in a nonlinear transmission medium.

Assuming that the optical fiber medium has no free charges, has a negligible conductivity, and is a nonmagnetic material, we have shown that:

$$\overrightarrow{curl}\,\overrightarrow{curl}\,\vec{E}(\vec{r},t) = -\mu_0\varepsilon_0\frac{\partial^2\vec{E}(\vec{r},t)}{\partial t^2} - \mu_0\frac{\partial^2\vec{P}(\vec{r},t)}{\partial t^2}$$

Since: $\overrightarrow{curl}\,\overrightarrow{curl}\,\vec{E}(\vec{r},t) = \overrightarrow{grad}\left(div\vec{E}(\vec{r},t)\right) - \Delta\vec{E}(\vec{r},t) = -\Delta\vec{E}(\vec{r},t)$, the equation above can be rewritten as:

$$-\Delta\vec{\mathrm{E}}(\vec{r},t) = -\mu_0\varepsilon_0\frac{\partial^2\vec{\mathrm{E}}(\vec{r},t)}{\partial t^2} - \mu_0\frac{\partial^2\vec{P}(\vec{r},t)}{\partial t^2}$$

Or equivalently:

$$\Delta\vec{\mathrm{E}}(\vec{r},t) - \mu_0\varepsilon_0\frac{\partial^2\vec{\mathrm{E}}(\vec{r},t)}{\partial t^2} = \mu_0\frac{\partial^2\vec{P}(\vec{r},t)}{\partial t^2}$$

Where $\varepsilon_0$the permittivity of vacuum, μ_0 is the permeability of vacuum, $\vec{E}(\vec{r},t)$ the electric field and $\vec{P}(\vec{r},t)$ the electric polarization of the material.

In general, $\vec{P}(\vec{r},t)$ can be expanded in terms of increasing powers of $\vec{E}(\vec{r},t)$ [32]:

$$\vec{P}(\vec{r},t) = \varepsilon_0\left[\chi^{(1)}.\vec{E}(\vec{r},t) + \chi^{(2)}.\left|\vec{E}(\vec{r},t)\right|.\vec{E}(\vec{r},t) + \chi^{(3)}.\left|\vec{E}(\vec{r},t)\right|^2.\vec{E}(\vec{r},t) + \cdots\right]$$

Where $\chi^{(j)}$ is the j[th] order susceptibility and is a tensor of rank j+1 [32]. The first order susceptibility $\chi^{(1)}$ is related to the linear refractive index [32]. The second order susceptibility $\chi^{(2)}$ is responsible for second-harmonic generation [32]. In the case of glass optical fiber, silica is a symmetric molecule and $\chi^{(2)}$ = 0 [32]. The third order susceptibility $\chi^{(3)}$ is responsible for third-harmonic generation and the Kerr effect [32].

Thus, $\vec{P}(\vec{r},t)$ can be re-expressed as follows:

$$\vec{P}(\vec{r},t) = \underbrace{\varepsilon_0\chi^{(1)}.\vec{E}(\vec{r},t)} + \underbrace{\varepsilon_0\chi^{(3)}.\left|\vec{E}(\vec{r},t)\right|^2.\vec{E}(\vec{r},t) + \cdots} = \overrightarrow{P_L}(\vec{r},t) + \overrightarrow{P_{NL}}(\vec{r},t)$$

Where $\overrightarrow{P_L}(\vec{r},t)$ is the linear electric polarization of the material, and $\overrightarrow{P_{NL}}(\vec{r},t)$ is the nonlinear electric polarization of the medium.

Substituting the expression of the electric polarization $\vec{P}(\vec{r},t)$ in the wave equation, we obtain:

$$\Delta\vec{\mathrm{E}}(\vec{r},t) - \mu_0\varepsilon_0{n_0}^2\frac{\partial^2\vec{\mathrm{E}}(\vec{r},t)}{\partial t^2} = \mu_0\frac{\partial^2\overrightarrow{P_{NL}}(\vec{r},t)}{\partial t^2}$$

Where ${n_0}^2 = 1 + \chi^{(1)}$ is the linear refractive index of the medium.

The nonlinearity analysis in optical fibers can be carried out by incorporating the nonlinear polarization $\overrightarrow{P_{NL}}(\vec{r},t)$ into the wave equation.

Because the higher order products of $\vec{E}(\vec{r},t)$ are negligible, it suffices to consider that the nonlinear electric polarization of the medium is given by:

$$\overrightarrow{P_{NL}}(\vec{r},t) = \varepsilon_0\chi^{(3)}.\left|\vec{E}(\vec{r},t)\right|^2.\vec{E}(\vec{r},t)$$

For SPM, we are only interested in the nonlinearity that are caused by the interaction between the input field $\vec{E}(\vec{r},t)$ and itself at the frequency ω. Assume the incident monochromatic electric field is linearly polarized along the x axis, and propagates along the + z axis:

$$\vec{E}(\vec{r},t) = E_0(\vec{r},t).\exp \mathrm{i}[\omega t - \beta_r(\omega)z]\,\overrightarrow{e_x}$$

Therefore the corresponding linear electric polarization is given by [32]:

$$\overrightarrow{P_L}(\vec{r},t) = \varepsilon_0.{\chi_{xx}}^{(1)}.\vec{E}(\vec{r},t)$$

Where ${\chi_{xx}}^{(1)}$ is a component of the second-rank tensor $\chi^{(1)}$ [32].

And the corresponding nonlinear electric polarization is given by [32]:

$$\overrightarrow{P_{NL}}(\vec{r},t) = \frac{3}{4}\varepsilon_0.{\chi_{xxxx}}^{(3)}.|E_0(\vec{r},t)|^{\,2}.\vec{E}(\vec{r},t)$$

Where ${\chi_{xxxx}}^{(3)}$ is a component of the fourth-rank tensor $\chi^{(3)}$ [32].

Consequently, we have:

$$\vec{P}(\vec{r},t) = \varepsilon_0\left({\chi_{xx}}^{(1)} + \frac{3}{4}{\chi_{xxxx}}^{(3)}|E_0(\vec{r},t)|^{\,2}\right).\vec{E}(\vec{r},t)$$

If we note [32]:

$$\vec{P}(\vec{r},t) = \varepsilon_0\chi_{eff}\vec{E}(\vec{r},t)$$

Where χ_{eff} is the effective susceptibility of the medium, we obtain by identification:

$$\chi_{eff} = \left({\chi_{xx}}^{(1)} + \frac{3}{4}{\chi_{xxxx}}^{(3)}|E_0(\vec{r},t)|^{\,2}\right)$$

Since the refraction index $n^{\,2}$ verifies [32]:

$$n^{\,2} = 1 + \chi_{eff} = \underbrace{1 + {\chi_{xx}}^{(1)}} + \frac{3}{4}{\chi_{xxxx}}^{(3)}|E_0(\vec{r},t)|^{\,2} = {n_0}^{2} + \frac{3}{4}{\chi_{xxxx}}^{(3)}|E_0(\vec{r},t)|^{\,2}$$

We conclude that the refraction index of the medium is given by [32]:

$$n = n_0\sqrt{1 + \frac{3}{4\,{n_0}^{2}}{\chi_{xxxx}}^{(3)}|E_0(\vec{r},t)|^{\,2}} \sim n_0 + n_2|E_0(\vec{r},t)|^{\,2}$$

Where ${n_0}^2 = 1 + {\chi_{xx}}^{(1)}$ is the linear refractive index of the medium, and $n_2 = \frac{3}{8{n_0}^2}{\chi_{xxxx}}^{(3)}$ is called the Kerr coefficient [32].

Thus, the electrical field contains an additional time-varying phase term that introduces a new frequency component to the original pulse after propagating through the nonlinear medium.

The analysis of XPM is similar to the analysis of SPM, except that the input pulses contributions come from different frequencies or polarizations.

FWM describes the generation of a fourth frequency tone with the interaction of three fields. The analysis of the FWM can be carried out in a similar manner using the wave equation.

2.3 SYSTEM COMPONENTS

Fundamental fiber optic systems components are the transmitter laser, optical modulators, optical amplifiers, detectors, and passive optical components. These components impose bandwidth and performance limitations in a fiber optic network.

2.3.1 LASERS

Current fiber optic transmitters employ laser sources with an external modulators. Modern laser sources are tunable in frequency and power. Some systems utilize directly modulated lasers, although these are less common.

DFB and external cavity (EC) lasers are the most commonly used types of lasers in telecommunications. DFB lasers meet the power, tunability, and linewidth requirements for 10 Gb/s and 40 Gb/s systems. Recent DFB laser designs enabled applications for 100 Gb/s systems. EC lasers can offer an order of magnitude advantage in linewidth compared to DFB lasers and are the leading choice for deployment in coherent systems (especially for the local oscillator at the coherent receiver side). Multiple systems design parameters affect the choice of type of lasers suited for a particular application, among these

parameters: cost, minimum required quality of transmission, power consumption, life cycle…

2.3.2 OPTICAL MODULATORS

External optical modulators are used to place the electrical message signal inside the optical signal carrier. External modulators for optical telecommunication systems can be manufactured in Lithium Niobate (LN) (LiNbO3). Recent advances in manufacturing techniques for optical communications systems have enabled the utilization of Indium Phosphide (InP) for external modulators.

An applied electric field can induce refraction index changes in the modulator crystal structures, proportional to the strength of the applied field. The modulator crystal is shaped into a waveguide structure with an electrode attached along the length of the waveguide, to control the changes of refractive index. A single waveguide and electrode yields phase-only modulation. By controlling the input electric field, the crystal's output optical signal phase can be modified.

Intensity modulation can be achieved by using a dual parallel path structure called Mach-Zehnder Interferometer (MZI) or Mach-Zehnder Modulator (MZM). By splitting the crystal waveguide into two equivalent paths and then applying electric fields between the electrodes in the two parallel waveguides, constructive or destructive interference can be achieved after recombining the photons from the parallel waveguides.

The electric field transfer function of a MZI is given by:

$$\frac{E_{out}}{E_{in}} = \cos(\frac{\pi V_{in}}{V_{\pi}})$$

Where V_{in} is the driving voltage (electrical modulating signal), E_{in} (E_{out}) is the input (output) electric field of the optical signal, and V_{π} is the half-wave voltage of the modulator (voltage that induces a π phase shift in the photons travelling through the waveguide, resulting in destructive interferences).

Quadrature or I/Q modulation can be achieved by inserting two independent MZIs into the paths of an outer third MZI, Fig. 2.6. The outer MZI is controlled to have a 90 degree relative phase difference between its two arms. The output electric filed of the optical signal is modulated in intensity in both its in-phase and quadrature components.

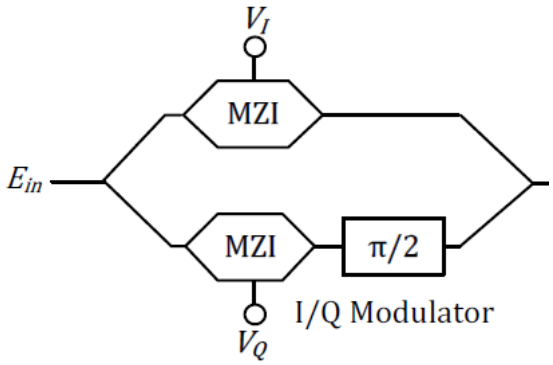

Fig. 2.6. I/Q modulator constructed from three nested Mach-Zehnder interferometers.

2.3.3 OPTICAL AMPLIFIERS

There are two primary amplifier technologies for optical telecommunications: the EDFA and the Raman amplifier.

The EDFA is comprised of a short length of fiber doped with Erbium and pumped by high-power lasers. The pump lasers induce population inversion in the Erbium atoms. The Erbium atoms, at an excited level, decay by emitting extra photons at the same phase, frequency, and direction than the incoming photons from the optical signal. The stimulated emission process is limited to incoming optical signals in the 1520 – 1570 nm frequency band (about the C-band). However, EDFAs also generate spontaneous emission photons that are incoherent with the incoming signal. These emitted incoherent photons are due to the non-stimulated decay of excited Erbium atoms. This phenomenon is called amplified spontaneous emission (ASE) and is one of the performance limiting noise components in

optical communications systems. ASE is responsible for degrading the OSNR of the propagating optical signal.

Fiber Raman amplifiers exploit the Stimulated Raman scattering effect in fiber by pumping the transmission fiber ~14 THz above the desired gain frequency. Raman amplifiers therefore utilize the transmission fiber itself as the gain medium, distributing the total gain along the length of the fiber. For carefully chosen pump power, the gain induced by the pump laser can exactly equal the loss induced by the fiber medium, resulting in the signal to maintain a constant average power along the fiber.

Unlike EDFAs, Raman amplifiers can provide gain at any wavelength, opening the possibility to transport data at other low-loss wavelength bands such as the S-band.

2.3.4 DETECTORS

Once the transmitted signal propagated through the optical link, it is usually selected by an optical filter at the receiver side. The signal may then be detected directly, differentially, or coherently. Since direct and coherent detection are the two most widely deployed methods in fiber optic networks, we cover direct detection and coherent detection receivers in Chapter 2 - Section 5.

2.3.5 PASSIVE OPTICAL COMPONENTS

We review three types of passive optical components, critical to the management of optical signals in fiber optic networks: couplers, isolators and circulators, and multiplexers and filters.

Couplers

A directional coupler is used to combine and split signals in an optical network [33]. A $n \times n$ coupler consists of n input ports and n output ports. In the case of a 2×2 coupler, a fraction α of the power from input 1 and places it on output 1 and the remaining fraction $(1 - \alpha)$ on output 2. Similarly, a fraction $(1 - \alpha)$ of the power from input 2 is

distributed to output 1 and the remaining power to output 2 [33]. The parameter α is called the coupling ratio [33].

Couplers have multiple applications in optical networks [33]. The simplest application is to combine or split signals in the network [33]. Couplers are the building blocks for several other optical devices: MZIs, multiplexers, demultiplexers…

Isolators and Circulators

An isolator allows transmission in one direction but blocks all transmission in the other direction [33]. Isolators are used in systems at the output of optical amplifiers and lasers primarily to prevent reflections from entering these devices, which would otherwise degrade their performance [33].

A circulator is similar to an isolator, except that it has multiple ports, typically three or four [33]. In a three-port circulator, an input signal on port 1 is sent out on port 2, an input signal on port 2 is sent out on port 3, and an input signal on port 3 is sent out on port 1 [33]. Circulators are useful to construct optical add/drop elements [33]. Circulators operate on the same principles as isolators [33].

Multiplexers and Filters

An optical filter is a two-port device that selects one frequency band and rejects all other wavelengths. It may have an additional third port on which the rejected wavelengths can be obtained [33].

A multiplexer combines signals at different wavelengths on its input ports onto a common output port, and a demultiplexer performs the opposite function [Rama 3]. Multiplexers and demultiplexers are critical for WDM systems. Specifically, channels in WDM networks are typically routed using reconfigurable optical add/drop multiplexers (ROADMs). ROADMs are comprised of optical filters that individually select WDM channels to drop or add. ROADMs allow remote configuration and reconfiguration for bandwidth assignment purposes.

2.4 MODULATION

Modulation is the process of placing a message signal (the modulating signal), which contains information to be transmitted, inside a carrier signal, that can be transported in a physical transmission medium. Specifically, the placement of the message inside the carrier is performed by varying one or more properties of the carrier signal (amplitude, frequency, phase, polarization…) in accordance with the message signal.

In fiber optic communications, the modulation process results in the conversion of the electronic data to be transmitted into an optical signal that can be transported over the fiber. Optical modulators are used to convert the data from the electrical domain to the optical domain.

2.4.1 MODULATION SCHEMES

A laser continuous wave output is commonly used as an optical carrier whose properties can be varied in accordance with the message signal. Let the laser output electric field be:

$$E_c(t) = Re\{E_0 . \exp(2\pi i f_c t + \varphi)\}$$

Where E_0 is the amplitude, f_c the carrier frequency, and φ the phase.

On-off Keying (OOK)

The most commonly used modulation format in optical communications is the intensity modulated OOK. In this modulation scheme a ‘1’ bit is encoded by the presence of a light pulse in the bit interval while a ‘0’ bit is encoded by the (quasi-) absence of a light pulse in the bit interval.

Amplitude-Shift Keying (ASK)

When the amplitude E_0 is modified in accordance with a modulating digital signal $m(t)$, while keeping the carrier frequency f_c and phase φ constant, the resulting

modulation scheme is known as amplitude-shift keying (ASK). The amplitude of the carrier is given by:

$$E_0(t) = k_1.m(t)$$

Where k_1 is amplitude sensitivity. The carrier is said to be amplitude modulated and we have:

$$E(t) = Re\{k.m(t).\exp(2\pi i f_c t + \varphi)\}$$

Phase-Shift Keying (PSK)

When the carrier phase φ is varied in accordance with the modulating digital signal $m(t)$, while keeping the amplitude E_0 and carrier frequency f_c constant, the resulting modulation scheme is known as phase-shift keying (PSK). The phase of the carrier is given by:

$$\varphi(t) = k_2.m(t)$$

Where k_2 is phase sensitivity. The carrier is said to be phase modulated and we have:

$$E(t) = Re\{E_0.\exp[2\pi i f_c t + k_2.m(t)]\}$$

Frequency-Shift Keying (FSK)

When the carrier frequency f_c is varied in accordance with the modulating digital signal $m(t)$, while keeping the amplitude E_0 and carrier phase φ constant, the resulting modulation scheme is known as frequency-shift keying (FSK). The frequency of the carrier is given by:

$$f_c(t) = f_0 + k_3.m(t)$$

Where k_3 is the frequency modulation index. The carrier is said to be frequency modulated and we have:

$$E(t) = Re\{E_0.\exp[2\pi i f_0 t + 2\pi i k_3.m(t)t + \varphi]\}$$

Quadrature Amplitude Modulation (QAM)

When the carrier amplitude E_0 and phase φ is modulated in accordance with the modulating digital signal $m(t)$, we obtain the modulation scheme known as quadrature amplitude modulation (QAM) or amplitude and phase-shift keying (APSK).

$$E(t) = Re\{p(t).\exp \mathrm{i}[2\pi f_c t + \theta(t)]\}$$
$$= m_I(\mathrm{t})\cos(2\pi \mathrm{i} f_c t) - m_Q(\mathrm{t})\sin(2\pi \mathrm{i} f_c t)$$

Where $m(\mathrm{t}) = p(t).\exp[\mathrm{i}\,\theta(t)] = m_I(\mathrm{t}) + i m_Q(\mathrm{t})$ is the modulating signal.

The amplitude of the in-phase carrier $\cos(2\pi \mathrm{i} f_c t)$ is modulated by $m_I(\mathrm{t}) = Re\{m(t)\}$ and the quadrature carrier $\sin(2\pi \mathrm{i} f_c t)$ is modulated by $m_Q(\mathrm{t}) = Im\{m(t)\}$. This modulating scheme is known as QAM.

2.4.2 SPECTRAL EFFICIENCY

The SE of a digital signal is defined as the ratio of the bit rate to the bandwidth used by the signal:

$$SE = \frac{f_{bit}}{B}$$

Where f_{bit} is the bit rate (bit/s), and B is the bandwidth used by the signal (Hz).

The SE also depends on the modulation format and coding scheme used [34]. OOK modulated digital signals can theoretically achieve a SE of 1 b/s/Hz. On the other hand, 64-QAM modulated digital signals can theoretically achieve a SE of 6 b/s/Hz.

Higher order modulation formats can be used to increase the SE. Indeed, higher order formats can help augment the bit rate. Alternatively, higher order formats can decrease the bandwidth used by the signal for the same amount of information transmitted.

2.4.3 PULSE SHAPING

Pulse shaping is used to facilitate the transmission of the signal of interest in the communication channel. It enables to control the bandwidth used by the transmitted signal, as well as the profile of the digital signal's spectrum. Since pulse shaping can be used to control the bandwidth occupied by the transmitted signal, it can thus be used to modify the

SE of the digital signal. Ultimately, pulse shaping helps control the amount of inter-symbol interference (ISI) and inter-channel interference (ICI) in the transmission channel.

The widely used pulse shapes are non-return-to-zero (NRZ), and return-to-zero (RZ). In the case of NRZ, the signal does not return to the zero level between two consecutive ‘1’s in a bit stream. For RZ signals, the signal returns to the zero level at the end of every bit slot. As a result, RZ signals occupy a larger spectral bandwidth than NRZ signals. The RZ signal duty cycle can help control the bandwidth occupied by the transmitted signal.

Ideal Nyquist pulse shaping enables the cancellation of ICI by maintaining spectral orthogonality between the sub-carriers in the transmission channel, as well as the cancellation of ISI by maintaining temporal orthogonality between time-domain pulses. Indeed, in theory, when sampling at the zero-crossing points of the ideal Nyquist pulses, the resulting sampled signal is ISI free and the entire transmitted information can be recovered without any distortion. Practically, it is very hard to maintain both spectral and temporal orthogonality due to hardware limitations. Raised cosine (RC) and root raised cosine (RRC) shaped Nyquist pulses are used to limit and control the amount of ISI and ICI in the transmission channel. Both RC and RRC shaped Nyquist pulses maintain orthogonal temporal shapes while controlling the spectral spreading via the roll-off factor. When RC spectra are used at the transmitter and a matched filter is used at the receiver, the overall system response is not RC and might cause the received signals to lose temporal orthogonality. Therefore, in practical communication systems, RRC shape is usually used. To maintain an overall RC response, the receiver matched filter is also RRC shaped and resembles the transmitter pulse shaping.

2.4.4 CHANNEL MULTIPLEXING TECHNIQUES

Channel multiplexing techniques attempts to achieve high SE by using dense channel spectra while retaining both spectral and temporal orthogonality (inter-channel and

ISI free). Two related schemes are CO-OFDM and Nyquist-wavelength division multiplexing (Nyquist-WDM).

Coherent Orthogonal Frequency-Division Multiplexing (CO-OFDM)

In CO-OFDM systems, multiple sub-carriers are shaped as cardinal sine functions in the frequency domain. Each sub-carrier is 'spaced' in the frequency domain exactly at the symbol rate from its adjacent sub-carrier neighbors to obtain a high SE system. Symbol transitions are time-aligned for all the sub-carriers. Ideally, this achieves both ICI and ISI free operation if proper filtering and sampling is performed. Nonetheless, the realization is challenging because of the stringent requirement of perfect rectangular temporal pulse shaping and large receiver bandwidth with fast ADCs.

Nyquist Wavelength Division Multiplexing (Nyquist-WDM)

Nyquist-WDM systems requires cardinal sine shaped time domain pulses and thus an ideal rectangular shaped spectrum with a bandwidth equal to the symbol rate. Since the spectra of the sub-channels are not overlapped, the ICI effects can be limited. Nyquist-WDM systems also achieve ISI free transmission by maintaining temporal orthogonality between time-domain pulses.

Nyquist-WDM systems relax the bandwidth requirement of the receiver compared with CO-OFDM systems.

2.5 DEMODULATION

Modulated signals are transmitted over the optical fiber where they undergo a variety of impairments. At the receiver, the transmitted data must be recovered with an acceptable bit error rate (BER). Recovering the transmitted data involves a number of steps. In general, the first step consist in converting the received optical signal into an electrical current with a photodetector. In an optical communication system, the photodetector can be configured either as direct (or incoherent) detector, or as a coherent detector. Because

the electrical current amplitude is low, a front-end amplifier is used to amplify it. Then, the amplified electrical current undergoes a variety of signal processing routines to mitigate transmission impairments and recover the transmitted data.

In this section, we cover all the steps involved in the demodulation of a received optical signal.

2.5.1 DIRECT DETECTION RECEIVER

In a direct (or incoherent) detection system, a photodiode converts the incoming radiation into an electrical signal. The electrical signal is proportional to the power of the incident light. There is no phase, frequency or polarization information, and the photo-signal is then processed electronically by signal processing circuits to mitigate transmission impairments and recover the transmitted data.

The main challenge in recovering the transmitted data is that, in addition to the desired photo-signal, there are usually three other additional noise currents [34]. The first is the thermal noise current due to the random motion of electrons. Thermal noise is always present at any finite temperature [34]. The second is the shot noise current due to the random distribution of the electrons generated by the photodetection process. Shot noise occurs even when the input light intensity is constant [34]. The third source of noise is the spontaneous emission due to optical amplifiers that may be used between the source and the photodetector [34].

Because of the inaccessibility to phase or frequency information, direct detection systems are only suited to simple intensity modulated signals. This type of detection is usually cost effective. However, as the phase, frequency or polarization information is not retained, all the channel impairments like CD and PMD have to be minimized before detection, limiting the deployment of spectrally efficient modulation formats.

In the case of direct detection systems, amplification of the electrical signal is followed by low-pass filtering. The low-pass filter is used to truncate the noise spectrum.

Since the variance of the receiver noise is proportional to the receiver bandwidth [35], it is best to keep the bandwidth of the low-pass filter low enough to minimize the noise level in the received signal, but high enough in order to minimize the truncation of the received signal spectrum. Low-pass filter bandwidth optimization results in an optimization of the signal-to-noise ratio (SNR).

After low-pass filtering, data recovery consists of a clock (or timing) recovery circuit and a decision circuit. Timing recovery aims at determining the symbol boundaries. Usually, both the clock frequency and phase are recovered simultaneously by a single circuit. Once the bit boundaries are recovered, the decision circuit identifies the symbol stream in the received signal.

2.5.2 COHERENT DETECTION RECEIVER

In contrast to direct detection, coherent detection has a more complicated receiver structure that enables the detection of the amplitude, phase, and, in some conditions, the SOP of the optical electric field. This information can be used to realize advanced electrical signal processing for impairment compensation.

Coherent detection provides gain to the signal by mixing it with another light signal from a local laser (the local oscillator). At the same time, the dominant noise in the receiver becomes the shot noise due to the local oscillator (LO), allowing the receiver to achieve the shot noise limited sensitivity [34].

Coherent detection can be implemented for single polarization or PDM systems. We represented the structure of the X polarization branch of a coherent receiver implemented for PDM systems, Fig. 2.7.

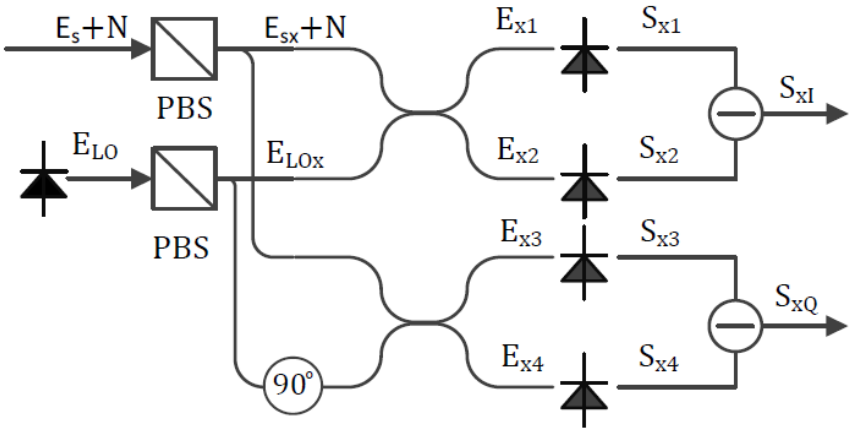

Fig. 2.7. X polarization branch of a coherent receiver implemented for polarization division multiplexing systems.

The received optical signal (E_S) and LO signal (E_{LO}) are filtered through polarization beam splitters to isolate the components along the X and Y polarizations of the coherent receiver. Then the resulting optical signal field in the X polarization (E_{SX}) is mixed with the resulting LO signal in the same polarization (E_{LOX}) using a ε/(1- ε) coupler which has a power transmission of ε and (1- ε) in each output branch. The electric fields at the coupler outputs are represented in the following equations:

$$E_{X1}(t) = \sqrt{1-\varepsilon}\,[\,E_{SX}(t) + N(t)] + \sqrt{\varepsilon}\,E_{LOX}(t)$$

$$E_{X2}(t) = -\sqrt{\varepsilon}\,[\,E_{SX}(t) + N(t)] + \sqrt{1-\varepsilon}\,E_{LOX}(t)$$

$$E_{X3}(t) = \sqrt{1-\varepsilon}\,[\,E_{SX}(t) + N(t)] + i\sqrt{\varepsilon}\,E_{LOX}(t)$$

$$E_{X4}(t) = -\sqrt{\varepsilon}\,[\,E_{SX}(t) + N(t)] + i\sqrt{1-\varepsilon}\,E_{LOX}(t)$$

The output electrical signals $S_{Xk}(t)$ of the photodetectors are obtained according to the square law detection formula:

$$S_{Xk}(t) = R_k|E_{Xk}(t)|^2$$

Where R_k is the responsivity of each photodetector.

$$S_{X1} = R_1\left[(1-\varepsilon)(|E_{SX}|^2 + |N|^2 + 2Re\{E_{SX}\overline{N}\}) + \varepsilon|E_{LOX}|^2 + 2\sqrt{\varepsilon(1-\varepsilon)}Re\{E_{SX}\overline{E_{LOX}} + N\overline{E_{LOX}}\}\right]$$

$$S_{X2} = R_2\left[\varepsilon(|E_{SX}|^2 + |N|^2 + 2Re\{E_{SX}\overline{N}\}) + (1-\varepsilon)|E_{LOX}|^2 - 2\sqrt{\varepsilon(1-\varepsilon)}Re\{E_{SX}\overline{E_{LOX}} + N\overline{E_{LOX}}\}\right]$$

$$S_{X3} = R_3\left[(1-\varepsilon)(|E_{SX}|^2 + |N|^2 + 2Re\{E_{SX}\overline{N}\}) + \varepsilon|E_{LOX}|^2 + 2\sqrt{\varepsilon(1-\varepsilon)}Im\{E_{SX}\overline{E_{LOX}} + N\overline{E_{LOX}}\}\right]$$

$$S_{X4} = R_4\left[\varepsilon(|E_{SX}|^2 + |N|^2 + 2Re\{E_{SX}\overline{N}\}) + (1-\varepsilon)|E_{LOX}|^2 - 2\sqrt{\varepsilon(1-\varepsilon)}Im\{E_{SX}\overline{E_{LOX}} + N\overline{E_{LOX}}\}\right]$$

For an ideal balanced receiver, where ε=0.5 and $R_k = r$, the outputs of the coherent receiver become:

$$S_{XI} = S_{X1} - S_{X2} = 2rRe\{E_{SX}\overline{E_{LOX}} + N\overline{E_{LOX}}\}$$
$$S_{XQ} = S_{X3} - S_{X4} = 2rIm\{E_{SX}\overline{E_{LOX}} + N\overline{E_{LOX}}\}$$

Both the in-phase and quadrature components are detected, enabling DSP. These electrical signals are sampled using ADCs and then forwarded for DSP circuits which mitigate transmission impairments and recover the transmitted data.

The advantages of coherent detection systems compared to direct detection systems are as follows:

- The coherent receiver offers the received signal gain, which is proportional to the LO power, therefore lowering the receiver sensitivity.
- The output electrical photocurrent is a linear transformation of the optical signal field. Photo-signals contains amplitude and phase information, and to a certain extent, information on the SOP of the received signal.
- The coherent receiver enables DSP.

2.5.3 DIGITAL SIGNAL PROCESSING

A polarization-diverse coherent optical receiver provides four analog voltage waveforms (I and Q on each polarizations) to the digitizer. After digitization the samples are fed into signal processing circuits to recover the original transmitted data. Digitization and recovery of electric field phase information simplifies reception of complex-valued modulation formats, and provides a common receiver front end. The coherent receiver also enables compensation of both linear and nonlinear fiber channel impairments.

Regardless of the modulation format, a digital coherent optical receiver must perform several specific tasks to properly recover the transmitted data. In general order, these steps are; digitization, CD compensation, timing recovery, polarization demultiplexing, and carrier phase recovery. Each of these steps requires substantial information about the transmitted signal to optimally function and in some cases to function at all.

We presented, Fig. 2.8, the general DSP architecture for polarization-diverse coherent optical receivers.

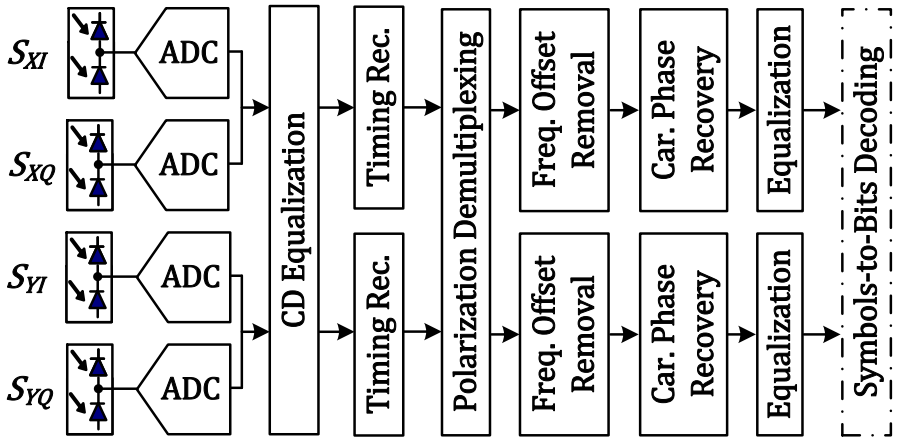

Fig. 2.8. General digital signal processing architecture for coherent optical receivers. Each processing step is implemented individually and independently. The cascade of steps is operated module-by-module.

Chromatic Dispersion Equalization

The first stage of the coherent demodulation is to compensate the total accumulated CD. The CD is a linear transmission channel impairment that causes a parabolic phase change in the transmitted signal with the frequency domain transfer function modeled as [36]:

$$H_{CD}(f) = \exp(-i\frac{\pi cDL}{(f_c-f)^2}f^2)$$

Where L is the fiber length, and D is the fiber CD coefficient. fc is the carrier frequency and f is the symbol rate of the modulating electrical signal ($-F_s/2 \leq f \leq F_s/2$, with F_s: the sampling rate of the ADC). Since $fc \gg f$, $(f_c - f)^2$ can be approximated by ${f_c}^2$, we thus obtain a simplified frequency domain transfer function for CD:

$$H_{CD}(f) \cong \exp(-i\frac{\pi cDL}{{f_c}^2}f^2)$$

The minimum tap length of $H_{CD}\ (f)$ is estimated by $cLDf_{max}F_s/{f_c}^2$, where f_{max} is the frequency of the spectrum edge of the transmitted signal [36]. The most straightforward way to implement this linear filter is to convolve it with the baseband signals. However, the computation complexity is proportional to the square of the filter tap length. The other approach is to implement this filter in the frequency domain using the overlap-save method [36] which significantly reduces the implementation complexity.

For an unknown transmission system, the total accumulated dispersion DL can be estimated blindly via various approaches (See Chapter 4 - Section 5.1).

Timing Recovery

Because the detected signal is received without any timing reference, an estimate of the timing phase must be made prior to polarization demultiplexing. Complete demodulation requires identification of the optimum timing for proper symbol detection. Timing recovery aims at determining the symbol boundaries in the CD compensated received signal. Specifically, the algorithm aims at removing the sampling jitter of the

transmitter and receiver clock sources by extracting the periodic clock tone from the received signal spectrum. Ultimately, timing recovery enables the extraction of adequate samples corresponding to the maximum eye opening (optimum timing). Numerous works reported non-data aided (or blind) timing phase estimator algorithms to mitigate the receiver sampling clock timing error and jitter [37 - 46]. In our work, we implemented the timing recovery method with the feedforward digital filter and square method [37].

The absolute timing phase offset is extracted from the spectral component of the squared signal at the symbol rate (f) tone, Fig. 2.9. This algorithm enables efficient timing recovery at high symbol rates for all modulation format of interest.

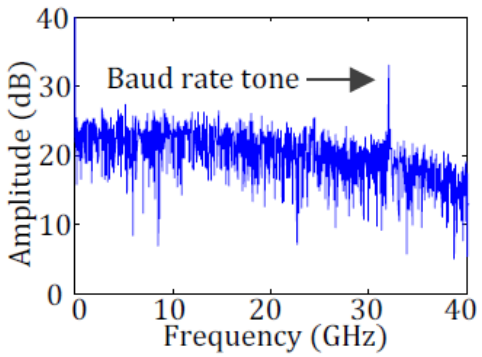

Fig. 2.9. Frequency-domain representation of timing phase offset extraction of a 32 Gbaud PDM-QPSK signal.

For a block length of L samples, the normalized timing phase error in the X polarization is estimated by:

$$\hat{\varepsilon}_x = -\frac{1}{2\pi}\arg\left(\sum_{k=mL}^{(m+1)L-1} x[k]e^{-2\pi jk\, f/F_s}\right) \; for\; m \in \mathbf{Z}$$

Where x is the X polarization digital signal.

L is properly chosen such that it is sufficient long to average out the channel noise and is able to track the timing variation. $\hat{\varepsilon}_x$ and $\hat{\varepsilon}_y$ deliver a time error that is normalized to the oversampling rate and has a value between $[-1/2,1/2]$. Because the timing error is

continuous, the estimated timing phase errors $\hat{\varepsilon}_x$ and $\hat{\varepsilon}_y$ have to be unwrapped before being used for sampling error correction.

Polarization Demultiplexing

In a PDM system, the incident signals on the coherent receiver are separated into two linearly polarized components with a polarization beam splitter. Because the signals have an arbitrary SOP, the detected signals contain mixed information from both polarizations. The transmission channel can be modeled by the Jones matrix $\boldsymbol{J}$, with the input and output electrical filed relation described by:

$$\begin{pmatrix} E_{Xout} \\ E_{Yout} \end{pmatrix} = \boldsymbol{J} \begin{pmatrix} E_{Xin} \\ E_{Yin} \end{pmatrix} = \begin{pmatrix} \sqrt{\varepsilon}\exp(i\delta) & -\sqrt{1-\varepsilon} \\ \sqrt{1-\varepsilon} & \sqrt{\varepsilon}\exp(-i\delta) \end{pmatrix} \begin{pmatrix} E_{Xin} \\ E_{Yin} \end{pmatrix}$$

Where E_{Xin} (E_{Yin}) are the channel input electrical fields in the X (Y) polarizations. ε and δ denote the power splitting ratio and the phase difference between the two polarization. The goal of the polarization demultiplexing process is to identify the inverse of the Jones matrix $\boldsymbol{J}^{-1}$ such that $\boldsymbol{J}^{-1}E_{Xout}$ ($\boldsymbol{J}^{-1}E_{Yout}$) approximates E_{Xin} (E_{Yin}).

Polarization demultiplexing may be performed with a 2×2 MIMO system. The following relationship between the digital input signals to the polarization demultiplexing algorithm ($x_{in};\ y_{in}$) and digital output signals to the polarization demultiplexing algorithm ($x_{out};\ y_{out}$), models the polarization unscrambling process:

$$\begin{pmatrix} x_{out} \\ y_{out} \end{pmatrix} = \boldsymbol{J}^{-1} \begin{pmatrix} x_{in} \\ y_{in} \end{pmatrix} \Leftrightarrow \begin{pmatrix} x_{out} \\ y_{out} \end{pmatrix} = \begin{pmatrix} p_{xx} & p_{xy} \\ p_{yx} & p_{yy} \end{pmatrix} \begin{pmatrix} x_{in} \\ y_{in} \end{pmatrix}$$

The goal of the polarization demultiplexing process is to identify the inverse of the Jones matrix $\boldsymbol{J}^{-1}$ such that the output signals x_{out} and y_{out} of the polarization demultiplexing algorithm become equal to the input signals to the fiber link.

The elements in the matrix are complex valued coefficients. To ensure proper convergence, the following coefficients constrains must apply $p_{xx} = \overline{p_{yy}}$ and $p_{xy} = \overline{p_{yx}}$.

Different modulation formats have different optimum polarization demultiplexing algorithms. The Constant Modulus Algorithm (CMA) [47] while often functional is not optimum for constellations that do not have constant modulus. On the other hand, the Independent Component Analysis (ICA)-based polarization demultiplexing technique [48], although optimum for quadrature phase-shift keying (QPSK), 16-QAM and many other higher-order constellations, is not optimum for OOK and binary phase-shift keying (BPSK).

Constant Modulus Algorithm (CMA)-Based Polarization Demultiplexing

For constant modulus modulation formats, such as M-PSK, the CMA-based polarization division demultiplexing algorithm provides a set of adaptive equations to update the matrix elements of the inverse Jones matrix $\boldsymbol{J}^{-1}$. The matrix elements are updated symbol by symbol according to the equation:

$$\begin{pmatrix} p_{xx}[n+1] \\ p_{xy}[n+1] \end{pmatrix} = \begin{pmatrix} p_{xx}[n] \\ p_{xy}[n] \end{pmatrix} + \mu . e_x[n] . \begin{pmatrix} \overline{x_{in}[n]} \\ \overline{y_{in}[n]} \end{pmatrix}$$

Where e_x[n] = $(C^2 - |x_{out}[n]|^2)x_{out}[n]$ is the X polarization error signal, C is a constant modulus, and μ the step-size parameter. The conventional CMA-based polarization demultiplexing algorithm uses a constant modulus C = 1, thus obtaining the Godard algorithm [49]. A similar equation is used for updating p_{yx} and p_{yy}.

The CMA algorithm uses one constant ring value C for computing the error signals e_x and e_y of M-PSK signals. The CMA-based polarization demultiplexing algorithm can be modified to improve the demultiplexing performance when dealing with non-constant modulus higher order modulation formats. Algorithms such as the multi-modulus algorithm or weighted multi-modulus algorithm provide polarization demultiplexing solutions for non-constant modulus higher order modulation formats.

Independent Component Analysis (ICA)-Based Polarization Demultiplexing

The CMA does not perform polarization demultiplexing optimally for modulation formats that are not constrained to a constant modulus, such as M-QAM (for $M \neq \{2, 4\}$). An alternate method of separating polarization is ICA. ICA is based on the assumption that the two orthogonal polarization modes are statistically independent and uncorrelated. ICA attempts to maximize the "non-Gaussianity" (entropy) of the signal. The advantage to this approach is that an ICA equalizer can separate any two signal sources regardless of modulation format provided that they are each, in general, not Gaussian-distributed [50]. The tap update rule is based on the Natural Gradient method. The Natural Gradient method possesses the equivariance property: it converges asymptotically based on the stochastic properties of the source signals and regardless of the channel (or mixing) description [50]. Let $\vec{s}[k]$ be a two-dimensional vector comprised of $s_1[k]$ and $s_2[k]$, two statistically independent, non-Gaussian digital signals.

$$\vec{s}[k] = \begin{pmatrix} s_1[k] \\ s_2[k] \end{pmatrix}$$

The convolutive mixture of the two signals is given by:

$$\vec{x}[k] = \begin{pmatrix} x_1[k] \\ x_2[k] \end{pmatrix} = \sum_{p=0}^{L} \boldsymbol{H}_p \vec{s}[k-p]$$

Where $\boldsymbol{H}_p$ is the 2x2 channel matrix at the pth tap and L is the filter length.

The Natural Gradient method can be used to iteratively compute the tap weights of $\boldsymbol{W}_p$, the 2x2 compensating matrix at the pth tap, such that:

$$\sum_{p=0}^{L} \boldsymbol{W}_p \vec{x}[k-p] = \vec{s}[k]$$

The update equation to calculate the coefficients of the 2x2 compensating matrix $\boldsymbol{W}_p$ at the pth tap, is given by:

$$\boldsymbol{W}_p[k+1] = \boldsymbol{W}_p[k] + \mu(\boldsymbol{W}_p[k] - \boldsymbol{g}(\vec{y}[k-L]) + \boldsymbol{v}^T[k-p])$$

Where:

$$\vec{y}[k] = \sum_{p=0}^{L} \boldsymbol{W}_p \vec{x}[k-p]$$

$$\boldsymbol{v}[k] = \sum_{p=0}^{L} \boldsymbol{W}_{L-p}{}^{H} \vec{y}[k-p]$$

$$\boldsymbol{g}(\vec{y}) = \frac{\vec{y}}{|\vec{y}|}$$

$\boldsymbol{g}(\vec{y})$ is the chosen nonlinear function for sub-Gaussian signals [50].

For optical communication systems where the two convolved signals are the orthogonal polarization modes, the polarization demultiplexing equalizer is required to compensate for PMD. While a single-tap ICA equalizer can asynchronously separate sampled data, to compensate for PMD the equalizer needs more than one tap to cover the time walk-off of the polarization modes. Note that timing recovery must be performed prior to the polarization mode separation via ICA.

Frequency Offset Removal

In practical transmission systems, the LO laser is generally not strictly phase locked to the transmitter laser and is slowly drifting over time. As a result, the received signal is penalized by two type of impairments: the residual frequency offset and the carrier-LO phase noise.

The residual frequency offset can be considered constant over a certain time interval, which length depends on the linewidths of the transmitter and LO lasers. The carrier-local oscillator phase noise is the phase noise difference between the transmitter and the LO lasers.

The frequency offset between the source and the receiver (LO) lasers results in a continuously increasing or decreasing phase in the received signal. As a consequence, the received constellation is spinning in time. This offset can be minimized using a conventional approach [51].

Specifically, examination of the signal in the Fourier domain reveals the nearly constant frequency offset between the transmitter and the LO lasers. This method requires the neutralization of the phase modulation contribution prior to the Fourier analysis, which typically, can be achieved by raising the signal to a specific power p which depends on the modulation format.

Since frequency offset removal aims at neutralizing the bulk of the residual frequency offset in the received signal, the process does not have to be perfectly accurate as impact of imperfect neutralization of the residual frequency offset can be corrected in the next step of the demodulating algorithm. Specifically, carrier phase recovery can adjust imperfect correction carried in the residual frequency offset removal stage.

Therefore, usually p=4 provides a sufficiently robust estimation of the residual frequency offset. Indeed, most constellations present two orthogonal axis of symmetry (the I axis and the Q axis).

For polarization multiplexed, signals the frequency offset removal algorithm is applied on both demultiplexed X and Y polarizations; otherwise it is only applied on one polarization and the other is ignored.

Carrier Phase Recovery

There are a plethora of works in the fiber optic communication community providing solutions for the carrier phase recovery problem. We present two carrier phase recovery algorithms commonly used: the Viterbi-Viterbi algorithm and the 'phase integrator' algorithm derived from the 'Stop-and-go' algorithm.

The Viterbi-Viterbi Carrier Phase Recovery Algorithm

The Viterbi-Viterbi carrier phase recovery algorithm estimates the phase noise in the received signal. Similar to the conventional approach used for frequency offset removal algorithm, the Viterbi-Viterbi carrier phase recovery algorithm requires the neutralization

of the phase modulation contribution, which typically can be achieved by raising the signal to a specific power p, which in returns depends on the modulation format.

To illustrate the mechanics of the Viterbi-Viterbi carrier phase recovery algorithm, we use QPSK signals as an example. Consider a sequence of QPSK symbols $x[k]$ in a polar representation with phase noise $\varphi[k]$.

$$x[k] = \exp(i\theta[k] + \varphi[k]) + N[k]$$

Where $N[k]$ is complex Gaussian noise, and $\theta[k]$ is the phase modulation signal, specifically, for QPSK signals, we have $\theta[k] \in \{\pi/4, 3\pi/4, 5\pi/4, 7\pi/4\}$.

The phase noise $\varphi[k]$ is assumed to be constant over L consecutives symbols. The Viterbi-Viterbi phase estimator computes the phase by raising $x[k]$ to the power p=4 to remove data modulation and then sums them over the M symbols to remove the channel noise. The phase of the resulting signal is considered as the estimated phase noise $\tilde{\varphi}[k]$, and is given by:

$$\tilde{\varphi}[k] \cong \frac{1}{4}\arg\left(\sum_{n=0}^{L-1} x^4[n]\right)$$

The estimated phase noise $\tilde{\varphi}[k] \in [-\pi/4; \pi/4]$ has to be unwrapped before compensating. The phase unwrapping process is described as [52]:

$$\tilde{\varphi}[k] = \tilde{\varphi}[k] + \frac{2\pi}{4} f(\tilde{\varphi}[k] - \tilde{\varphi}[k-1])$$

Where $f(x)$ is defined as:

$$f(x) = \begin{cases} 1 \; if \; x < -\pi/4 \\ 0 \; if \; |x| \leq \pi/4 \\ -1 \; if \; x > \pi/4 \end{cases}$$

The 'Phase Integrator' Carrier Phase Recovery Algorithm

The 'phase integrator' carrier phase recovery algorithm is derived from the 'stop-and-go' decision-directed carrier phase recovery algorithm [53]. The algorithm effectively tracks the carrier phase instead of estimating it, as in the case of the Viterbi-Viterbi carrier

phase recovery algorithm. The algorithm employs a decision-directed update equation to estimate the carrier phase in the X polarization with the rule:

$$\tilde{\varphi}[k+1] = \tilde{\varphi}[k] - \mu_\theta Im\{x[k]\overline{e_x[k]}\}$$

Where: $e_x[k] = x[k] - a[k]$ is the X polarization error signal, x is the X polarization signal, a is the decision signal, and μ_φ the step-size parameter.

Equalization

The last stage of the coherent demodulation process is the linear equalization, which compensates the residual inter-channel-interferences and CD in the link, producing the optimum estimation of the transmitted data symbols. It assumes that the channel is stationary (time invariant) over a long period of time. Although different linear equalization structures and coefficients update algorithms are available, we implemented the decision-directed Least Mean Square (DD-LMS) algorithm based on steepest descent method. The equalizer is implemented in a blind fashion, where the Euclidean distance between the filter output and the reference constellation point is used to update the tap weights. Equalization is performed on X and Y polarization separately. The linear equalizer in this work operates at one sample/symbol and can be extended to multiple samples/symbol operation.

2.5.4 ERROR DETECTION AND CORRECTION

An error-correcting code is a method for decreasing the BER in a communication channel. It involves sending additional bits, called redundancy, along with the data bits [34]. These additional bits carry redundant information and are used at the receiver end to correct most of the errors in the transmitted data [34]. This method of reducing the error rate by having the transmitter send redundant information (using an error-correcting code) is called forward error correction (FEC). FEC codes are advantageous in that they can correct bit errors, which ultimately reduces the transmission BER [34]. This is especially important for optical communication systems that are expected to operate at a very low

residual BER: 10^{-12} or lower [34]. The coding gain of a forward-error correction (FEC) code is defined as the decrease in the receiver sensitivity that it provides for the same BER compared to the uncoded system (for similar system conditions). Codes with substantial coding gains, that is, which decrease the BER substantially for the same system conditions as in the uncoded system, have been designed by mathematicians and communication engineers over the last 50 years [34]. A popular and powerful family of such codes called Reed-Solomon codes.

CHAPTER 3

STATE OF THE ART

3.1 COGNITIVE NETWORKS

"A cognitive network has a cognitive process that can *perceive* current network conditions, and then *plan, decide,* and *act* on those conditions. The network can learn from these adaptations and use them to make future decisions, all while taking into account end-to-end goals" [54].

While cognitive radio concepts [55] were introduced within the last decade, cognitive optical networks is a topic of actual research [56, 57]. Borkowski's Doctoral dissertation [56] identifies the key critical technologies required to enable cognitive optical networks. His work envisions cognitive optical networks to provide solutions to the increasing complexity and heterogeneity of future optical networks.

Regardless of the physical layer, a cognitive network is an autonomous, self-optimizing, self-configuring, and self-healing network [56]. In order to *perceive, plan, decide,* and *act,* a cognitive network requires three critical components [56]:

- Network monitors, which enable *awareness* of the network.
- Software adaptable elements, which enable *adaptivity* of the network.
- Cognitive processes, which enable *cognition* of the network.

These three critical components enabling cognitive networks can be supported by the following technologies [56]:

- Flexible and elastic transmission systems, which aim at un-constraining spectrum and bandwidth allocation on the transport grid.
- Digital and software-defined transceivers, which can be dynamically reconfigured to transmit/receive any signal by modifying, at need, the DSP algorithms capabilities in the transmitter/receiver.

- Reprogrammable networks elements, which enable the fine control and management of transported signal spectrums.
- Performance monitoring, which aims at observing signals parameters (link impairments parameters and signal parameters).
- Machine learning algorithms, which provides the intelligence to the network.

3.2 FIBER OPTIC COMMUNICATIONS

3.2.1 CAPACITY

In this sub-section, we first study through Shannon's theorem the theoretical parameters limiting the fiber optic channel capacity. Then, we review the current state-of-the-art in fiber optic communication systems.

Shannon's Theorem

The following derivation of Shannon's theorem [58] is inspired from the work of Essiambre et al. [13].

Let X and Y be continuous complex random variables. X is the input to an additive white Gaussian noise channel, Fig. 3.1. Y is the output with: Y = X + N, where the noise N is a continuous complex Gaussian random variable, independent from X, with zero-mean, and variance $\sigma_N^2/2$. The probability density function (PDF) of N is given by the distribution:

$$p_N(n) = \frac{1}{\pi\sigma_N^2} e^{-|n|^2/\sigma_N^2}$$

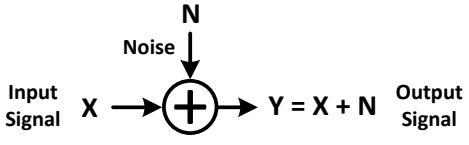

Fig. 3.1. Schematic representation of the additive white Gaussian noise channel.

The channel capacity $\tilde{C}$, in bits per modulation symbols, is the maximum *mutual information* $I(X;Y)$ across all possible input PDF distributions p_X. For limited power inputs X ($E[|X|^2] \leq P$), we have:

$$\tilde{C} = \max_{p_X:\, E[|X|^2] \leq P} I(X;Y)$$

The *mutual information* $I(X;Y)$ between two random variables X and Y is a quantity that measures the variables' mutual dependence, that is defined as:

$$I(X;Y) = h(Y) - h(Y|X)$$

Where $h(Y)$ is the differential entropy of the continuous random variable Y, and $h(Y|X)$ is the conditional entropy of Y given the knowledge of X.

The differential entropy $h(Y)$ is defined as: $h(Y) = \int - p_Y(y) log_2\, p_Y(y) dy$.

The conditional entropy $h(Y|X)$ is defined as: $h(Y|X) = \int - p_{XY}(x,y) log_2\, p_{Y|X}(y|x) dy$.

In the additive white Gaussian noise channel case, Shannon showed that the input PDF distributions p_X maximizing the *mutual information* $I(X;Y)$ are given for continuous complex Gaussian random variables [58], with PDF distributions of the form:

$$p_X(x) = \frac{1}{\pi P} e^{-|x|^2/P}$$

Therefore, if X and N are Gaussian random variables, then Y = X + N is also a Gaussian random variable with the variance ($P/2 + \sigma_N^2/2$). Consequently, we obtain:

$$h(Y|X) = h(X+N|X) = h(N|X) = h(N) = log_2(\pi e \sigma_N^2)$$

$$h(Y) = h(X+N) = log_2(\pi e P + \pi e \sigma_N^2)$$

The resulting channel capacity $\tilde{C}$, in bits per modulation symbols, is:

$$\tilde{C} = log_2\left(1 + \frac{P}{\sigma_N^2}\right)$$

Where P/σ_N^2 is referred as the SNR.

Assuming a signal occupying a bandwidth *B* is transmitted in the channel, and the noise power is equal to $\sigma_N^2 = N_0 B$, then the channel capacity, in bits per second, is:

$$\tilde{C} = Blog_2(1 + \frac{P}{N_0 B})$$

Capacity Limits of Optical Fiber

Regardless of the transmission medium, Shannon's theorem provides an upper bound on the capacity of a communication channel (assuming it follows the additive white Gaussian noise model):

$$C = B\ log_2(1 + SNR)$$

Where C is the channel capacity limit, B is the available bandwidth and *SNR* is the signal-to-noise ratio. Therefore, an upper bound on the SE is given by:

$$SE = \frac{C}{B} = log_2(1 + SNR)$$

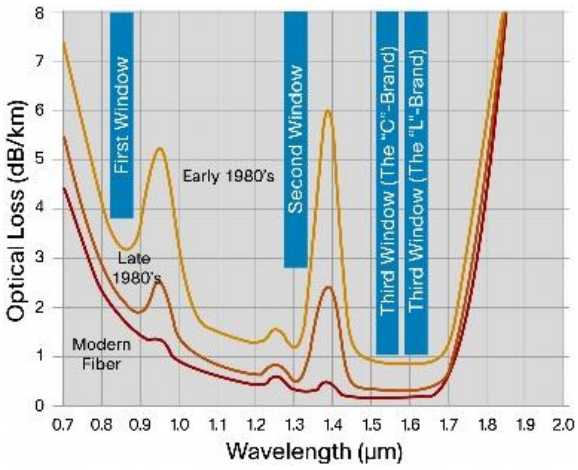

Fig. 3.2. Principal transmission windows in fiber optic communications. Source: [11].

As an illustration, across the three principal transmission windows for fiber optic communications (the O band: 1260-1360 nm, the C band or 'erbium window': 1530-1565 nm, and the L band: 1565-1625 nm), Fig. 3.2, the available bandwidth *B* is about 365 nm or about 54 THz. For modern optical networks, depending on the system application and reach, a typical value of the SNR is between 10-40dB, or 10-10,000 in linear scale. Accordingly, the corresponding capacity limit is about 700 Tb/s, and the SE limit is about

14 b/s/Hz. As a comparison, PDM-QPSK systems spectral efficiencies are 4 b/s/Hz and PDM-64QAM systems spectral efficiencies are 12 b/s/Hz.

Practically, modern long-haul optical systems operate at high power levels to overcome fiber losses and noise introduced by optical amplifiers. At these power levels, nonlinear effects, such as Kerr effect induced SPM, XPM, FWM, and Raman scattering, come into play. These nonlinear effects act similarly as additional noise, which increases as the transmitted power is increased. Therefore nonlinear effects impose additional limits on channel capacity [34].

Nonlinear effects limiting the fiber channel capacity were considered for various transmission distances ranging from 500 km to 8000 km, Fig. 3.3. Since higher capacities are achieved using higher order modulation formats, and since signals modulated with dense constellations are more sensitive to nonlinear distortions, higher order modulation formats systems prevent raising the signal power significantly, even when the transmission distance is shortened [13].

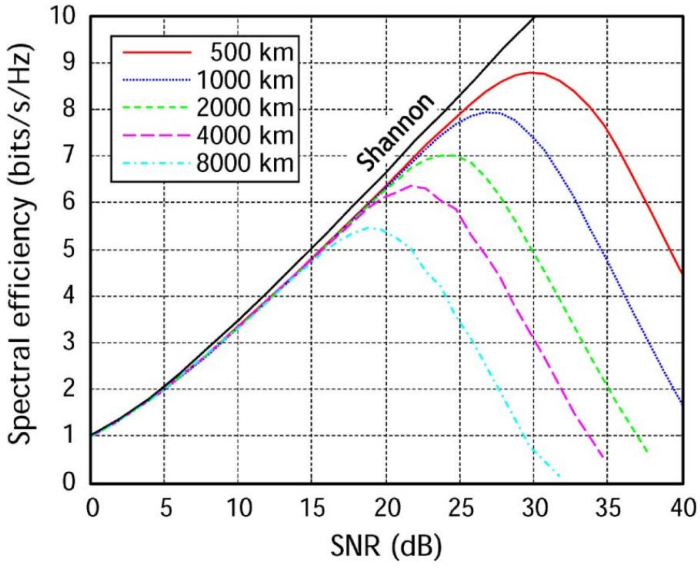

Fig. 3.3. Nonlinear capacity curves for several transmission distances. Source: [13].

Fig. 3.3 shows that for every doubling in the distance, the corresponding SNR at which the capacity peaks decreases by about 2.65 dB. But the ASE noise power doubles (or increases by 3 dB) for every doubling in the distance. Thus, the optimum signal power decreases by 0.35 dB for every doubling in the distance. Over the considered transmission distances ranging from 500 km to 8000 km, this represents a mere decrease in optimum signal power by only 1.4 dB. Therefore, optimal signal power has a weak dependence on distance [13].

As a conclusion, although Shannon theorem's upper bound on the capacity of a communication channel does not quantitatively indicates the limiting impact of nonlinear effects, it provides a simple tool to understand how to increase the fiber optic channel capacity, which is particularly reliable in regimes where nonlinear effects are negligible (linear regimes). Increasing the available bandwidth *B*, reducing the noise level *N* in the system, and reducing the effects of nonlinear effects contribute to increasing the fiber optic channel capacity.

State of the Art in Fiber Optic Communication Systems

The success of 100 Gb/s per channel transponders has been made possible with uninterrupted improvements in high-speed electronics, ameliorations of fiber optic network optical elements, and the utilization of advanced signaling techniques such as elaborate coding techniques and modulation formats [59].

While most of earlier progress in fiber optic communication systems have been related to capacity and reach with the development of Erbium-Doped Fiber Amplifier (EDFA) and WDM technologies, coherent detection has improved the transmission SE of fiber optic links by unlocking additional degrees of freedom for encoding of information. Indeed, polarization diverse coherent receivers enabled PDM and the retrieval of in-phase and quadrature signals of the electrical field in both orthogonal polarizations, thus making

phase, amplitude, and polarization recovery of the received full electrical field a possibility [12, 14].

Continuous development in high-speed electronics, specifically in ASICs, have made the advent of high-speed digital-to-analog converters (DACs), coupled with higher-speed ADCs and DSP techniques, a reality in commercial optical transmission systems [4]. Indeed, current commercial coherent optical receivers are generally followed by DSP routines designed to mitigate transmission impairments, recover polarization multiplexed signals, and subsequently encoded information. Typically, compensated transmission impairments are CD, ADC's sampling clock timing error and jitter, PMD, frequency offset, and carrier phase noise [14].

However, currently deployed transceivers are commonly designed for specific signal parameters (symbol rate, the number of multiplexed polarizations, and the modulation format) that are presumed known or knowable at the receiver, along with other link impairments parameters. Although in fiber optic communications, link impairments parameters are numerous resulting from transmitter contributions (modulators' I/Q imbalance, timing jitter, band limitations), fiber optic link contributions (CD, change in SOP, PMD, PDL , ICI , ASE noise, and Kerr-induced nonlinear effects such as SPM, XPM, and FWM), and receiver contributions (transmitter laser-LO frequency offset and phase noise contribution, ADC's sampling clock timing error and jitter, shot noise); only the knowledge of a small set of critical link impairments parameters is sufficient to proceed to the demodulation of the received signal. In general, the knowledge of both critical link impairments parameters and signal parameters can be communicated to the receiver through the supervisory control layer of the fiber optic network.

In order to drive optical communications beyond 100 Gb/s per channel, a better use of the available channel bandwidth is required. This can be made possible by deploying flexible optical transceivers that support multiple transmission schemes, modulation formats, data rates, FEC protocols, and subcarriers [60]. One way to realize flexible optical

transceivers is to implement the hardware in a way that can be dynamically reconfigured through a software interface. The concept of software-defined architecture applied to optical transceivers lies in the substitution of some or the entire physical layer functions of the transceiver analog circuit with a reprogrammable digital circuits. As for software-defined radio communication systems, the digital platform enables the use of signal processing technologies to implement conventional hardware operating functions in an adjustable manner [61].

Therefore, flexible optical transceivers technology enables the implementation of software-defined networking (SDN) in the optical domain. SDN combined with elastic grid optical networks [62] is expected to considerably enhance the capacity and fluidity of fiber optic communication networks, enabling network operators and cloud service providers to reduce additional capital and operational costs required for hosting new services by tailoring their infrastructure dynamically to user and application specifications [63].

De facto, with greater dynamic flexibility in capacity and reach, fiber optic transmission systems, historically suited for long-haul and submarine communication links, will accelerate the phagocytosis of the metro and regional terrestrial communication links at the cost of a higher network complexity.

While current state-of-the-art fiber optic communication systems have already reached a state of greater signal waveform flexibility and higher single-channel data rates that now exceed 200 Gb/s [4], the next generation of fiber optic communication systems will reach a further degree of dynamic adaptability in reach, data rate, or spectral occupancy [5] and aim at providing 400 Gb/s per channel transponders.

3.2.2 SOFTWARE-DEFINED OPTICAL TRANSCEIVERS

Software-defined radio is a radio communication system in which the transceiver hardware has been implemented in a fashion which can be dynamically modified through a software interface. This flexibility results from the substitution of some or entire physical

layer functions of the radio transceiver analog circuit with a reprogrammable digital circuit. The digital platform enables the use of signal processing technologies to implement conventional hardware operating functions in an adjustable manner [61].

The concept of Software-defined radio can be applied to optical communication systems. Software-defined optical transceivers are flexible optical transceivers whose characteristics can be modified in real time through a software interface. Software-defined optical transceivers rely on a hybrid analog/digital hardware implementation, DSP techniques, and flexible electro-optical hardware to adjust the signal reception channel or to select the transmission channel. Software-defined optical transceivers flexibility depends on the number of physical layer functions implemented digitally; cross-functionality increases directly with this number.

We distinguish two potentially collaborative components within a software-defined optical transceiver: the transmitter and the receiver that can indirectly interact through an intermediate control layer. The control layer is the decision source and is responsible for imposing the determined software-defined optical transceiver parameters.

Software-defined optical transceiver's autonomy is defined by its level of subordination to the control layer. A fully *dependent* software-defined optical transceiver, Fig. 3.4, is a transceiver whose characteristics are tuned according to decisions made at the control layer only. Conversely, a fully *autonomous* software-defined optical transceiver is a transceiver whose characteristics are adapted entirely on internally-based decisions without any influence of the control layer. Such architectures require a dynamic assessment of the communication channel status and real time collaboration between the transmitter and the receiver. Dynamic assessment of the communication channel status can be realized at the receiver with the combined implementation of channel probing techniques and blind DSP methods that enable the self-determination of the channel and signal transmission parameters. Software-defined optical transceivers can also be *semi-autonomous*, with a balanced submission to the control layer. Semi-autonomous transceiver architectures

contain some blind physical layer functions that are implemented to operate in an agnostic processing fashion, freeing subordinating processes towards the control layer.

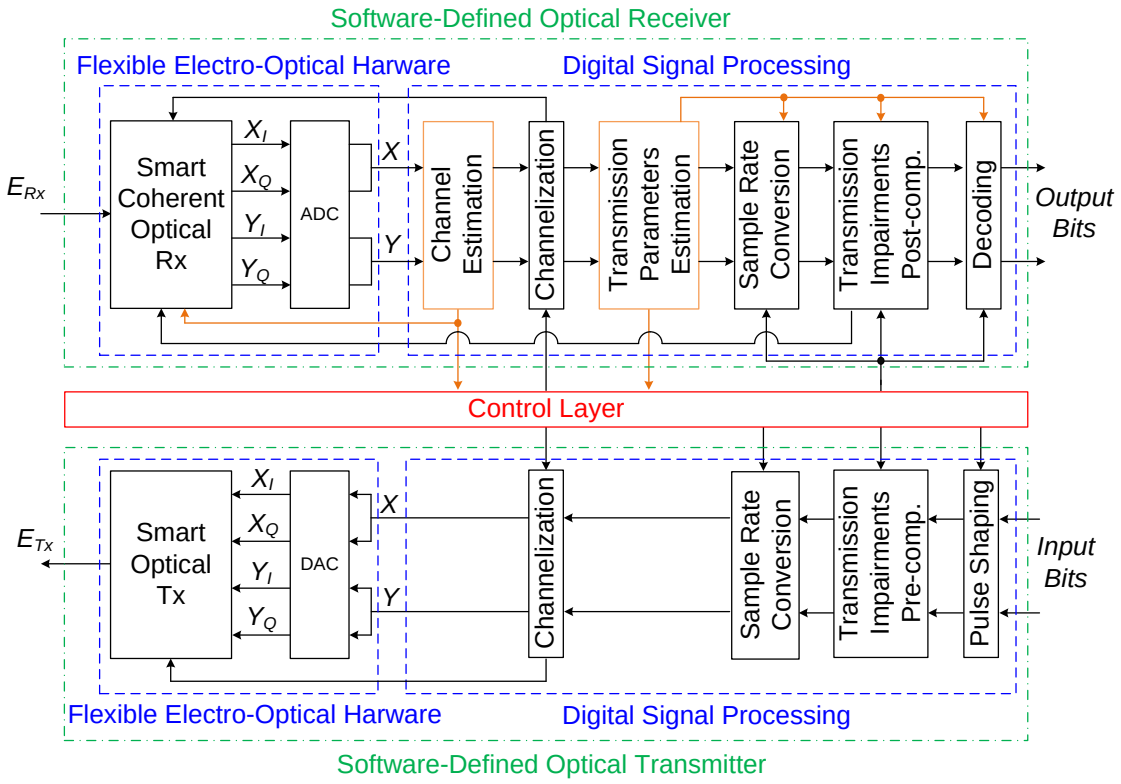

Fig. 3.4. Software-defined optical transceiver architecture. The orange processing blocks in additions to the traditional processing architecture are critical for enabling autonomy on the receiver-side.

Traditionally, within an optical receiver, channelization (selection and isolation of a single WDM channel), sample rate conversion, link impairments compensation and decoding require extensive knowledge of the received signal: channel location, bandwidth, symbol rate, polarization multiplexing state, modulation format, and total accumulated CD. The link impairments parameters and signal parameters are communicated by the omniscient control layer to the dependent software-defined optical transceiver. These four processing steps can be implemented to operate blindly without any a priori knowledge of the reception channels and signals.

In order to perform blind channelization, it is required to estimate the channel occupancy. A recent experimental demonstration of blind channel estimation [64] reported the successful use of a digital coherent optical receiver with a fast switching digital supermode distributed Bragg reflector tunable laser as the LO to perform fast spectrum estimation across the C-band.

Implementation of semi-autonomous software-defined optical receivers, based on coherent detection technology, performing blind sample rate conversion, link impairments compensation and decoding, is investigated in details in Chapter 4.

3.2.3 TRAINING-AIDED DIGITAL SIGNAL PROCESSING

Currently deployed optical transceivers require strong knowledge of link impairments parameters and signal parameters to be available at the receiver side - including cognition of the modulation format, nominal symbol rate, and the number of multiplexed polarizations - to digitally mitigate link impairments and demodulate the received signal.

In most applications, the knowledge of both link impairments parameters and signal parameters can be communicated to the receiver by the network supervisory control layer, resulting in real-time synchronization between a link transmitter and receiver. Such situations are suitable to training-aided signaling methods, in which pilot signals are inserted in the transmitted optical signal, and used to probe the communication link status, estimate existing transmission impairments, and mitigate them.

Numerous works report the use of data-aided signaling techniques. These methods can be used to estimate CD and DGD [65 - 67], estimate PDL and in-band OSNR [68], estimate the signal frequency offset [69, 70], estimate and equalize the 2x2 MIMO transmission channel [71], or enable format-flexible single-carrier reception and demodulation [72] in coherent optical transmission systems.

3.2.4 BLIND DIGITAL SIGNAL PROCESSING

There are circumstances where the receiver cannot be synchronized with the transmitter via the network supervisory control layer, thus making acquisition of the properties of the incoming signal impossible and rendering training-aided communication techniques inapplicable. Consequently, in some applications, it is valuable to be able to detect the incoming optical signal link impairments parameters and signal parameters without any prior knowledge of its properties.

By exploiting the power of dynamic DSP, algorithms can be designed to first blindly retrieve both link impairments parameters and signal parameters, and then blindly mitigate transmission impairments without cognition of the incoming signal properties. However, there are tradeoffs to acknowledge when switching from training-aided to blind processing. In general, blind algorithms exhibit slower adaptation, worse performance for low SNR, and are less stable than training-aided methods. Additionally, blind receivers have higher complexity [73].

In this subsection, we investigate state-of-the-art work on blind identification and mitigation of link impairments parameters and blind identification of signal parameters.

Blind Link Impairments Parameters Identification and Mitigation

Some equalization functions of coherent optical receivers have been implemented in a partially blind fashion. However most of the basic transmission parameters such as the modulation format, the symbol rate, and the number of multiplexed polarizations are presumed known at the receiver.

Blind adaptive CD estimation and equalization algorithms have been reported by M. Kuschnerov et al. [74]. The algorithms principles are based on the concept that a perfectly dispersion-compensated optical signal exhibits a minimum amplitude variance.

Numerous works reported blind timing phase estimator algorithms to mitigate the receiver sampling clock timing error and jitter [37 - 46].

K. Kikuchi introduced a blind polarization demultiplexing and PMD equalization algorithm based on the CMA [47]. However, the CMA, while often functional, is not optimum for constellations that do not have a constant modulus, for example, square M-QAM signals for $M \neq \{2;4\}$. Additionally, conventional CMA equalization can fail for BPSK signals [75]. To account for non-constant modulus constellations, blind multi-modulus algorithms [76] can be used to perform polarization demultiplexing. S. Amari et al. presented a blind deconvolution and equalization algorithm implemented with the natural gradient method [50]. This algorithm, developed to solve the problem of blind source separation, can be used for demultiplexing optical signals polarizations.

Blind adaptive estimation and compensation of carrier phase noise is also subject to extensive research. Various algorithms for carrier phase recovery (CPR) have been proposed for wireless communications and subsequently adopted in optical coherent systems, such as the famous Viterbi-Viterbi algorithm proposed by A.J. Viterbi and A.M. Viterbi [77]. G. Picchi et al. introduced the Stop-and-Go decision-directed algorithm, which is a blind decision-directed equalizer that can interrupt adaptation when the reliability of the self-decided output error is too low. The Stop-and-Go technique can be applied to carrier phase recovery [53], obtaining a more flexible adaptation rule than the one introduced in the classic decision-directed mean-square error (MSE) iterative algorithm - also known as the phase integrator. Other works propose and validate novel carrier phase recovery algorithms by introducing different cost functions [78, 79].

Blind Signal Parameters Identification

Numerous investigations report the development of methods that enable to detect the incoming optical or wireless signal transmission parameters without any prior knowledge of its properties.

A blind estimation technique of the symbol rate for M-PSK and QAM optical signals based on utilizing the standard deviation of the signal spectrum has been presented

and experimentally validated by M.V. Ionescu et al. [80]. Other works in the Radio Frequency (RF) communication domain have reported methods to estimate the symbol rate of a received wireless signal exploiting the cyclostationary random process nature of the signal [81], or the Haar wavelet transform [82].

A blind channel estimation method enabling to perform fast spectrum estimation across the C-band using a fast switching digital supermode distributed Bragg reflector (DSDBR), a coherent optical receiver, and DSP was reported by H.-M. Chin et al. [64].

Q. Sui et al. presented a method to monitor OSNR using polarization diversity and DSP in the presence of first-order PMD [83].

MFR is of high interest for the next generation of optical networks. In general, a modulation format adaptive optical receiver has to perform MFR in order to ensure proper demodulation. Multiple works have investigated various optical modulation format identification techniques. Gonzalez et al. introduced a likelihood-based approach that monitors the constellation diagram with the use of k-means, which utilizes probabilistic and hypothesis testing to identify the incoming signal modulation format [84]. Khan et al. presented a feature-based method that uses artificial neural networks (ANN) based on direct detection amplitude histograms (which requires prior training to obtain correct classification results) to extract prominent features from the received signal that are utilized for the identification of signal modulation format [85]. Borkowski et al. proposed a method based exclusively on Stokes space analysis that uses statistical signal processing techniques to extract the modulation format signature [86, 87]. OSNR limitations encountered in this method, inherent to Stokes space mapping which distorts the noise PDF [88, 89], were mitigated by revising the statistical signal processing methods [89]. Liu et al. proposed a feature-based approach that uses the statistical distribution of the received signal's power [90]. Tan et al. presented a novel technique for simultaneous identification of the bit-rate and the modulation format using principal component analysis (PCA) [91]. Cui et al.

introduced a feature-based approach that uses an improved method for asynchronous amplitude histogram (AAH) [92].

The majority of the work on MFR require some prior knowledge of the transmission parameters such as the symbol rate, or the number of multiplexed polarizations.

3.3 WIRELESS PHOTONICS COMMUNICATIONS

Photonic assisted wireless signal generation is based on direct up-conversion of optical baseband signals using photonic techniques, Fig. 3.5.

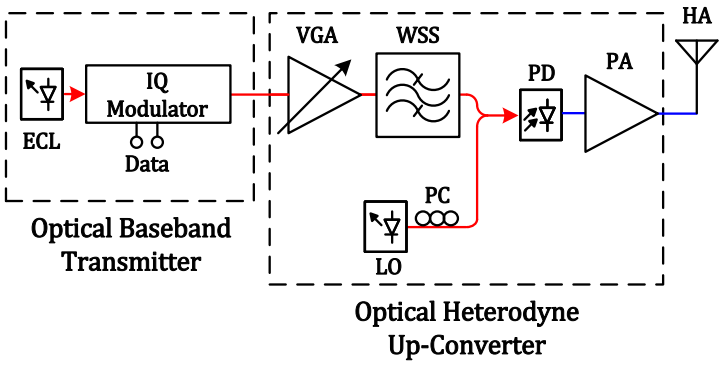

Fig. 3.5. Principle of photonic assisted wireless signal generation.

This technology can be seamlessly integrated to the fiber optic network. Extending the combined photonic transmitter and optical channel with the wireless channel results in a hybrid fiber-wireless transmission system capable of transporting multi-gigabit signals in a wireless band of interest, whose frequency boundaries are determined by the transmission link design and components capabilities. We refer such links as multi-gigabit photonic assisted wireless communication links, Fig. 3.6.

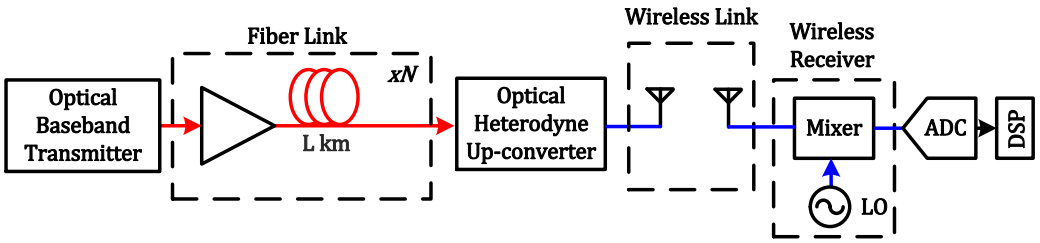

Fig. 3.6. Multi-gigabit photonic assisted wireless communication link.

Numerous works report the integration of a wireless photonic transmitter to a wireless channel to transport high data rate signals at different carrier frequencies spanning microwave to high mm-wave frequency bands. H.-C. Chien et al. demonstrated the encoding of OOK signals onto radio-over-fiber (RoF) mm-wave in the 60 GHz band [93]. A. Hirata et al. detailed the successful transmission of a 10 Gb/s OOK signal at 120 GHz over 250m [94]. Koenig et al. transmitted a 20 Gb/s OOK signal at 220 GHz [6]. H.-J. Song et al. transported a 8 Gb/s OOK signal at 250 GHz over 0.5m [95].

To increase the SE and the link capacity, conventional optical methods such as PDM, higher modulation formats, Orthogonal Frequency Division Multiplexing (OFDM), and WDM can be implemented at the RF photonic transmitter. On the wireless transmitter side, orthogonal antenna polarization multiplexing, multi RF band multiplexing coupled with MIMO technologies can be deployed in the same sense. A. Kanno et al. reported the transmission of a 40Gb/s 16-QAM RoF signal over 30mm in the W-band [96]. The first demonstration of a 100 Gb/s single-input single-output (SISO) wireless link carrying a 25 Gbaud 16-QAM signal at 237.5 GHz over 20m was presented by Koenig et al. [97]. X. Li et al. described the transport of a 108 Gb/s PDM-QPSK signal at 100 GHz (W-band) with air transmission distance of 0.5m using wireless MIMO transmission [98]. X. Pang et al. transmitted a 100 Gb/s PDM-16-QAM signal at 87.5 GHz (W-band) over 120cm [99]. Multiple investigations report the successful encoding of multi-gigabit OFDM RoF signals at different data rates and carrier frequencies in the RF band [6, 100 - 104]. More recently

the highest capacity fiber-wireless link was reported to date with a bit rate exceeding 400 Gb/s using electrical heterodyne detection at a lower intermediate frequency (IF), multi-band multiplexing on two mm-wave bands (Q-band and W-band), orthogonal antenna polarizations and MIMO to transmit 2×112 Gb/s PDM-16QAM at 37.5GHz over 1.5m and 2×108 Gb/s PDM-QPSK at 100GHz over 0.7m [105].

Regardless of the method used for generating the incoming wireless signal, a heterodyne wireless communication link receiver must perform several specific tasks to properly recover the transmitted data. In general order, these steps are; digitization, digital down conversion, timing recovery, polarization demultiplexing, and carrier phase recovery. Each of these steps requires substantial information about the transmitted signal to optimally function and in some cases to function at all.

By exploiting the flexibility of wireless receivers, coupled with DSP, algorithms can be designed to blindly retrieve the optical-wireless link impairments and signal parameters, including the modulation format. Once these parameters have been identified, optimal demodulation of the received signal can be performed.

CHAPTER 4

BLIND SIGNAL IDENTIFICATION

4.1 CONCEPT OF AUTONOMOUS RECEIVER

The concept of autonomous receiver consists of a universal intelligent receiver, that can operate fully autonomously, requiring no intervention from a network operator or a supervisory control layer, and which can identify and demodulate, without prior knowledge and with negligible acquisition delay, any signal including: legacy optical signals not requiring coherent detection, modern high SE optical signals that require coherent detection technology, or even multi-gigabit photonic assisted wireless signals generated at an optical transmitter, transported in a wireless link and received at a wireless gateway.

4.2 MOTIVATION AND APPLICATIONS

With an independence towards the supervisory control layer, autonomous receivers have multiple applications.

Autonomous receivers enable rapid recovery from network failures without the need for slower supervisory control layer coordination. For example, these events occur when: the network elements are not properly synchronized with the flowing signal, the monitoring elements have failed, or when the supervisory channel is disrupted.

For short-lived connections, lasting the order of seconds, the delay incurred by the supervisory control layer may constitute a considerable overhead. Thus, autonomous receivers are well suited to applications when the supervisory channel is deemed too slow to allow fast and flexible provisioning.

Autonomous receivers can also be used for performance monitoring, where a dedicated receiver is used to acquire information about channels present in a link, and monitor channel performance in real-time.

Furthermore, autonomous receivers can be used for network diagnostic, and other surveillance applications involving noncooperating transmitters.

In the following sections, we present in details the designs of different architectures of autonomous receivers for fiber optic communication links (Chapter 4 - Section 3) and photonic assisted wireless communication links (Chapter 4 - Section 4).

4.3 ARCHITECTURES FOR FIBER OPTIC COMMUNICATION LINKS

Regardless of the modulation format, a digital coherent optical receiver must perform several specific tasks to properly recover the transmitted data. In general order, these steps are; digitization, CD compensation, timing recovery, polarization demultiplexing, and carrier phase recovery. Each of these steps requires substantial information about the transmitted signal to optimally function and in some cases to function at all.

By exploiting the flexibility of digital coherent receivers, algorithms can be designed to blindly retrieve the optical link impairments and signal parameters, including the modulation format. Once these parameters have been identified, optimal demodulation of the received signal can be performed.

Addressing the challenges raised by the next generation of fiber optic communication systems, which will involve a larger degree of dynamic adaptability in reach, data rate, and spectral occupancy, we designed two architectures of autonomous receivers that can recognize conventional modulation formats, including legacy OOK signals, M-PSK, M-PAM and M-QAM signals, and time domain-domain hybrid modulation formats, composed with M-PSK and/or M-QAM modulation formats.

Regardless of the modulation format, the proposed autonomous receiver architectures for fiber optic communications are structured in two consecutive modules. First, in the fully blind processing module, optical link impairments parameters (total accumulated CD) and signal parameters (symbol rate, number of multiplexed polarizations,

modulation format) are blindly estimated. Note that some of the parameters estimated in the first processing module can require to be performed only once (at system startup for example) and hence do not contribute significantly to the overall computational complexity. Second, in the format-optimized module, polarization demultiplexing, frequency offset removal, carrier phase recovery and equalization are performed, enabling the retrieval of additional optical link impairments parameters (frequency offset between the transmitter laser and the LO, phase noise contribution from the transmitter laser and the LO). The processing steps performed in the second module utilize an optimized set of algorithms chosen accordingly to the identified parameters in the first module.

With minimum prior knowledge of the transmitted optical signal, the proposed autonomous receiver architectures operate on the digitized version of the received IF signal. Currently we only assume that the signal is single carrier and that the approximate optical carrier frequency is known at the receiver (practically, sufficiently accurate to enable the signal of interest to be down-converted by intradyne mixing with the LO and fully captured by the bandwidth limitations of the receiver). We also assume that polarization division multiplexed (PDM) signals use the same format and symbol rate on both polarizations. This is certainly the case for all standard transmission systems using PDM.

4.3.1 PERFORMING CONVENTIONAL MODULATION FORMAT RECOGNITION

The proposed autonomous receiver architecture designed for performing conventional MFR, including legacy OOK signals, M-PSK, M-PAM and M-QAM signals, Fig. 4.1, consists in two consecutive modules. First, in the fully blind processing module, symbol rate estimation, CD estimation and equalization, and symbol timing recovery are performed on each detected polarization without knowledge of, or regard to any signal parameter. Furthermore, in the first module, we determine the number of multiplexed polarizations and the signal modulation format.

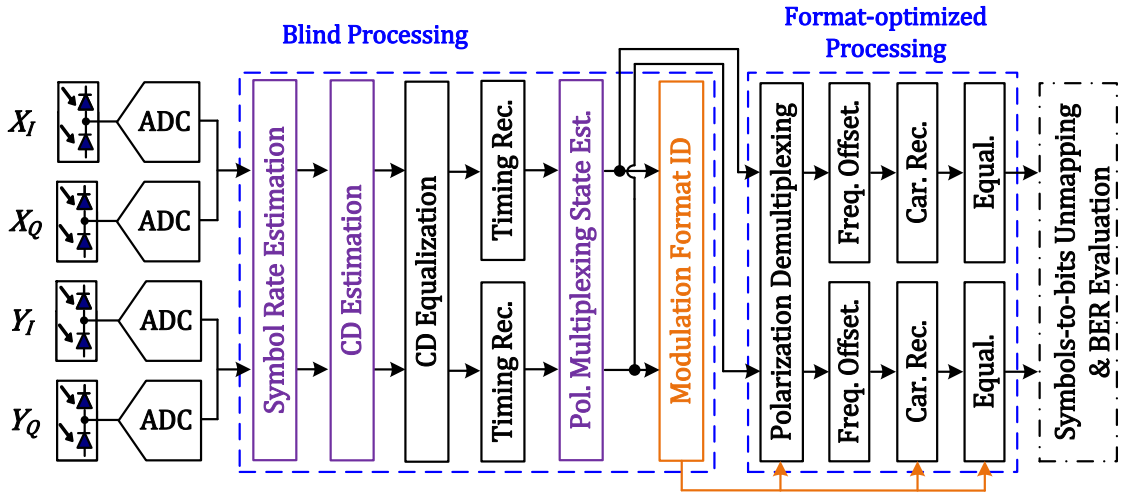

Fig. 4.1. Architecture of the autonomous receiver for fiber optic communication links performing conventional modulation format recognition.

Second, in the format-optimized module, polarization demultiplexing, frequency offset removal, carrier recovery and equalization are performed using an optimized set of algorithms chosen according to the identified parameters by the first module. Importantly, only the polarization demultiplexing requires implementation of distinct modulation format dependent algorithms. On the contrary, a single implementation of the frequency offset removal, the carrier phase recovery and the equalization algorithms is suitable as the knowledge of the modulation format constellation is sufficient for decision-directed equalizations, thus simplifying the overall complexity of the architectural design. Some of the algorithms, particularly in the second format specific module, may be similar to what might be expected in a conventional receiver.

This Chapter focuses on the blind parameters estimation algorithms contained in the blind processing module, such as symbol rate estimation, CD estimation, number of multiplexed polarizations estimation, and MFR. Blind parameters estimation algorithms are discussed in Chapter 4 Section 4.5. Other algorithms performed in the blind processing modules (CD equalization, timing recovery) and in the format-optimized processing

module (polarization demultiplexing, frequency offset removal, carrier phase recovery and equalization) are detailed in Chapter 2 - Section 5.3.

4.3.2 PERFORMING TIME-DOMAIN HYBRID MODULATION FORMAT RECOGNITION

A time-domain hybrid modulation format (TDHMF) consists in two different modulation formats interleaved in the time domain. TDHMFs can be generated with DAC enabled transmitters, and linear modulators and drivers. The receiver-side DSP architecture required to demodulate a TDHMF signals can be designed of equal complexity as for conventional single format signals [106]. Figure 4.2 illustrates the transmitted pattern of a TDHMF in the time domain.

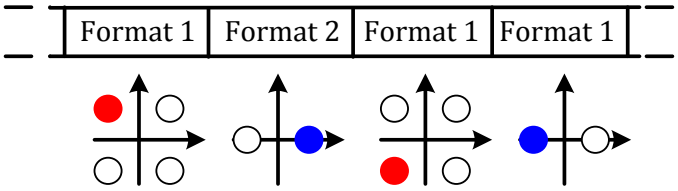

Fig. 4.2. Transmitted pattern of a time-domain hybrid modulation format. Here, the pattern is BPSK1-QPSK1, and is composed with one BPSK and one QPSK symbol.

TDHMFs are highly variable formats. TDHMFs enable to tune transmission links' attributes within a continuum of trade-offs between capacity, spectral occupancy and reach [106, 107], thus providing a solution for the next generation of fiber optic communication systems, which aims at providing a larger degree of dynamic adaptability in reach, data rate, and spectral occupancy. TDHMFs also increase the complexity in traffic patterns, specifically with regards to transceivers coordination.

The proposed autonomous receiver architecture designed for performing time-domain hybrid MFR, Fig. 4.3, is implemented with blind and flexible algorithms to achieve universal demodulation of any TDHMF composed with M-PSK and/or M-QAM formats. The architecture consists of two stages. First, in the fully blind processing module, symbol

rate estimation, CD estimation and equalization, and symbol timing recovery are performed on each detected polarization without knowledge of, or regard to any signal parameter. Furthermore, in the first module, we determine the number of multiplexed polarizations. The frame length is then estimated to determine the number of symbol in the TDHMF's pattern. The first module ends with blind polarization demultiplexing and time-domain hybrid modulation format recognition (TDHMF recognition). Polarization separation is performed blindly prior to MFR using an independent-component-analysis (ICA) based polarization demultiplexing algorithm.

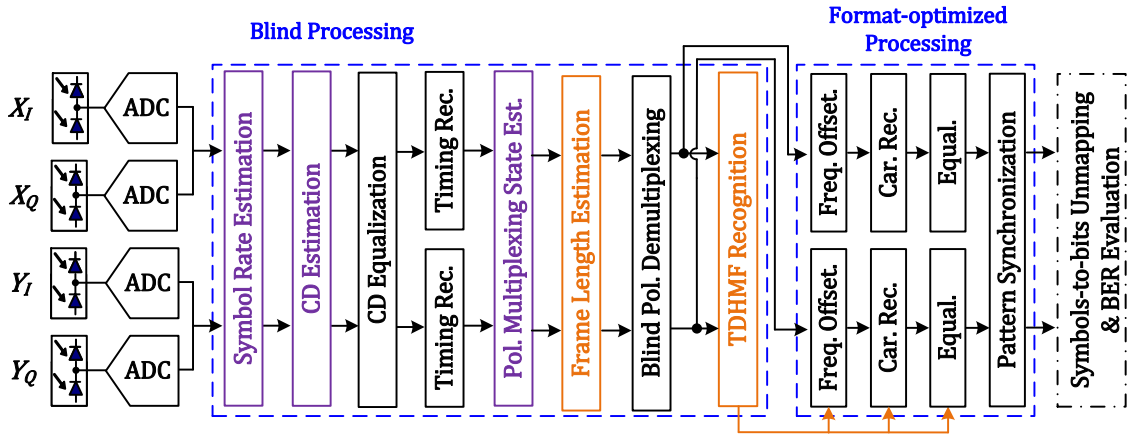

Fig. 4.3. Architecture of the autonomous receiver for fiber optic communication links performing time-domain hybrid modulation format recognition.

In the second stage, format-specific processing occurs to remove the transmitter laser-LO frequency offset, the transmitter laser-LO phase noise contribution, and mitigate ISI and residual channel effects. The second module ends with the pattern synchronization step, which consists in locking the received symbol stream with the TDHMF pattern for accurate symbol-to-bits unmapping. The frequency offset removal algorithm was revised to consider the TDHMF pattern since the conventional method (spectral analysis of the 4th power raise of the signal time-series, see Chapter 2 - Section 5.3) yields multiple spectral tones in the Fourier domain, corresponding to the desired frequency offset component scrambled with an undesired tones inherent to pattern periodicity. Note that a single

implementation of the frequency offset removal, the carrier phase recovery and the equalization algorithms is suitable as the knowledge of the TDHMF constellation is sufficient for decision-directed equalizations, thus simplifying the overall complexity of the architectural design.

This Chapter focuses on the blind parameters estimation algorithms contained in the blind processing module, such as symbol rate estimation, CD estimation, number of multiplexed polarizations estimation, frame length estimation, and TDHMF recognition. Blind parameters estimation algorithms are discussed in Chapter 4 - Section 4.5. Other algorithms performed in the blind processing modules (CD equalization, timing recovery, blind polarization demultiplexing) and in the format-optimized processing module (carrier phase recovery and equalization) are detailed in Chapter 2 - Section 5.3.

4.3.3 PERFORMING CONVENTIONAL AND TIME-DOMAIN HYBRID MODULATION FORMAT RECOGNITION

Combining the autonomous architecture designed for performing conventional MFR (Chapter 4 - Section 3.1), and the autonomous architecture designed for performing time-domain hybrid modulation format recognition (Chapter 4 – Section 3.2), we obtain the proposed autonomous architecture, Fig. 4.4, which without any prior knowledge of the transmitted signal, is capable of: identifying optical link impairments and signal parameters, including the modulation format, and optimally demodulating the received signal. The modulation format can be conventional, including OOK, M-PSK, M-PAM and M-QAM formats, or time-domain hybrid, composed with M-PSK and/or M-QAM formats.

The architecture is organized in two stages. First, in the fully blind processing module, symbol rate estimation, CD estimation and equalization, and symbol timing recovery are performed on each detected polarization without knowledge of, or regard to any signal parameter. Furthermore, in the first module, we determine the number of multiplexed polarizations. The frame length is then estimated to determine the number of

symbol in the TDHMF's pattern. Frame length estimation enables to determine if the modulation format is conventional (unit frame length) or time-domain hybrid. In each case, a different MFR algorithm is applied. Indeed, for TDHMF recognition, polarization demultiplexing is performed prior the MFR step; whereas for conventional modulation formats, MFR is performed before polarization demultiplexing, since polarization demultiplexing requires the implementation of distinct modulation format dependent algorithms.

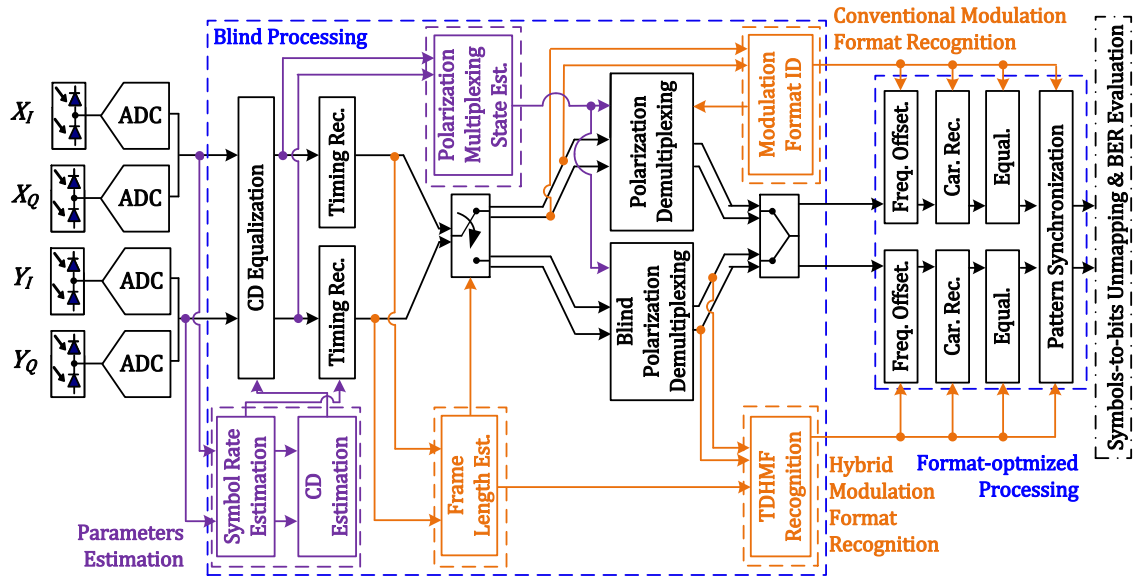

Fig. 4.4. Architecture of the autonomous receiver for fiber optic communication links performing conventional and time-domain hybrid modulation format recognition.

In the second stage, format-specific processing occurs to remove the transmitter laser-LO frequency offset, the transmitter laser-LO phase noise contribution, and mitigate ISI and residual channel effects. The second module ends with the pattern synchronization step, which consists in locking the received symbol stream with the TDHMF pattern for accurate symbol-to-bits unmapping. Note that a single implementation of the frequency offset removal, the carrier phase recovery and the equalization algorithms is suitable as the knowledge of the modulation format constellation is sufficient for decision-directed equalizations, thus simplifying the overall complexity of the architectural design.

This Chapter focuses on the blind parameters estimation algorithms contained in the blind processing module, such as symbol rate estimation, CD estimation, number of multiplexed polarizations estimation, frame length estimation, conventional and time-domain hybrid modulation format recognition. . Blind parameters estimation algorithms are discussed in Chapter 4 - Section 4.5. Other algorithms performed in the blind processing modules (CD equalization, timing recovery, polarization demultiplexing) and in the format-optimized processing module (frequency offset removal, carrier phase recovery and equalization) are detailed in Chapter 2 - Section 5.3.

4.4 ARCHITECTURE FOR PHOTONIC ASSISTES WIRELESS COMMUNICATION LINKS

Photonic assisted wireless signal generation is based on direct up-conversion of optical baseband signals using photonic techniques, Fig. 4.5.

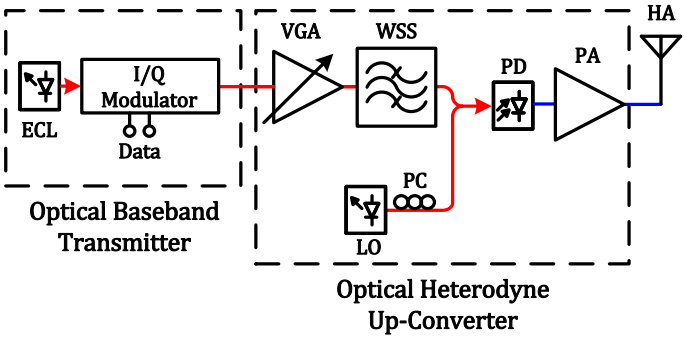

Fig. 4.5. Principle of photonic assisted wireless signal generation.

This technology can be seamlessly integrated to the fiber optic network. Extending the combined photonic transmitter and optical channel with the wireless channel results in a hybrid fiber-wireless transmission system capable of transporting multi-gigabit signals in a wireless band of interest, whose frequency boundaries are determined by the

transmission link design and components capabilities. We refer such links as multi-gigabit photonic assisted wireless communication links, Fig. 4.6.

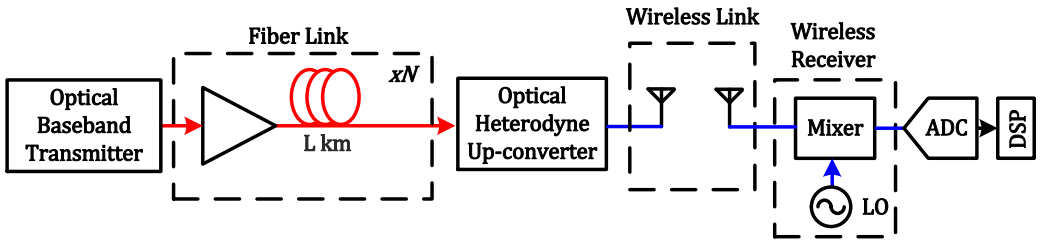

Fig. 4.6. Multi-gigabit photonic assisted wireless communication link.

Regardless of the method used for generating the incoming wireless signal, a heterodyne wireless communication link receiver must perform several specific tasks to properly recover the transmitted data. In general order, these steps are; digitization, digital down conversion, timing recovery, polarization demultiplexing, and carrier phase recovery. Each of these steps requires substantial information about the transmitted signal to optimally function and in some cases to function at all.

By exploiting the flexibility of wireless receivers, coupled with DSP, algorithms can be designed to blindly retrieve the optical-wireless link impairments and signal parameters, including the modulation format. Once these parameters have been identified, optimal demodulation of the received signal can be performed.

Therefore, we designed an autonomous receiver architecture for multi-gigabit photonic assisted wireless links, Fig. 4.7, that can identify the received wireless signal's modulation format amongst M-PSK and M-QAM and demodulate it.

With minimum prior knowledge of the transmitted wireless signal, the proposed autonomous receiver architecture operates on the digitized version of the received IF signal. Currently we only assume that the signal is single carrier and that the approximate wireless carrier frequency is known at the receiver (practically, sufficiently accurate to enable the signal of interest to be down-converted by heterodyne mixing with the LO and

fully captured by the bandwidth limitations of the receiver). We also assume that the signal is single polarized.

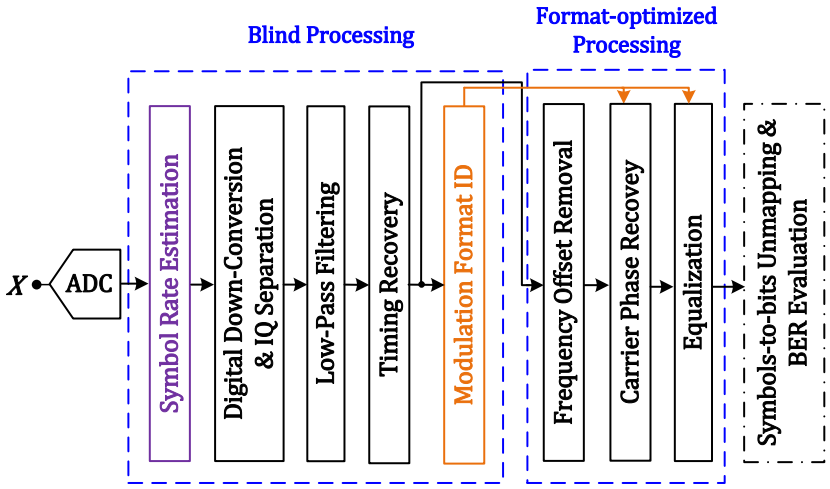

Fig. 4.7. Architecture of the autonomous receiver for photonic assisted wireless communication links performing modulation format recognition.

Note that photonic assisted wireless communication links can be designed to transport PDM optical signals, thus doubling the fiber-wireless transmission system capacity. One implementation consist in transporting the optical signal's orthogonal components (polarization scrambled or not) in orthogonally polarized wireless signals for transmission in the wireless link, Fig. 4.8. Consequently, wireless receivers need to be polarization diverse, and detect incoming wireless signals in each orthogonal polarization. The proposed autonomous receiver architecture for multi-gigabit photonic assisted wireless links, Fig. 4.7, can be modified without difficulty, to identify and demodulate PDM signals. By adding a *Polarization Demultiplexing* processing step between *Timing Recovery* and *Modulation Format ID* in the proposed architecture, Fig. 4.9, and by leveraging the methodology developed for autonomous receivers architectures for fiber optic communication links (see Chapter 4 - Section 3.1), PDM signals can be handled by the autonomous receiver architecture. The assumption necessary is that the same

modulation format and symbol rate are used on both polarizations, which is certainly the case for all standard transmission systems using PDM.

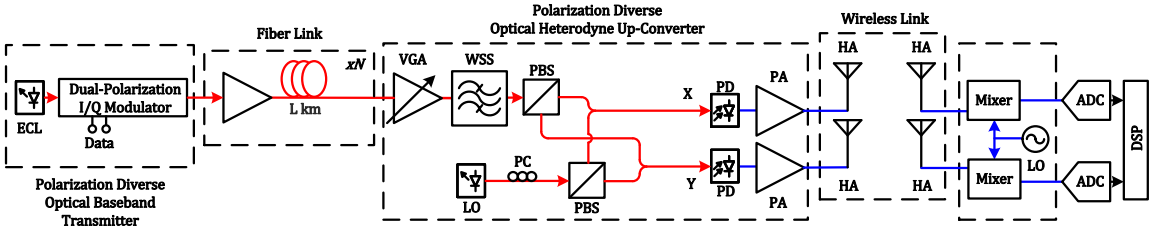

Fig. 4.8. Polarization division multiplexing multi-gigabit photonic assisted wireless communication link.

The proposed autonomous receiver architectures for multi-gigabit photonic assisted wireless links and designed for performing MFR, including M-PSK and M-QAM formats, Figs. 4.7 and 4.9, are based on heterodyne wireless reception technology. The architectures are organized in two consecutive modules. First, in the fully blind processing module, symbol rate estimation, digital down-conversion, and symbol timing recovery are performed without knowledge of, or regard to any signal parameter. In the case of PDM enabled systems, the number of polarization multiplexing states is also estimated.

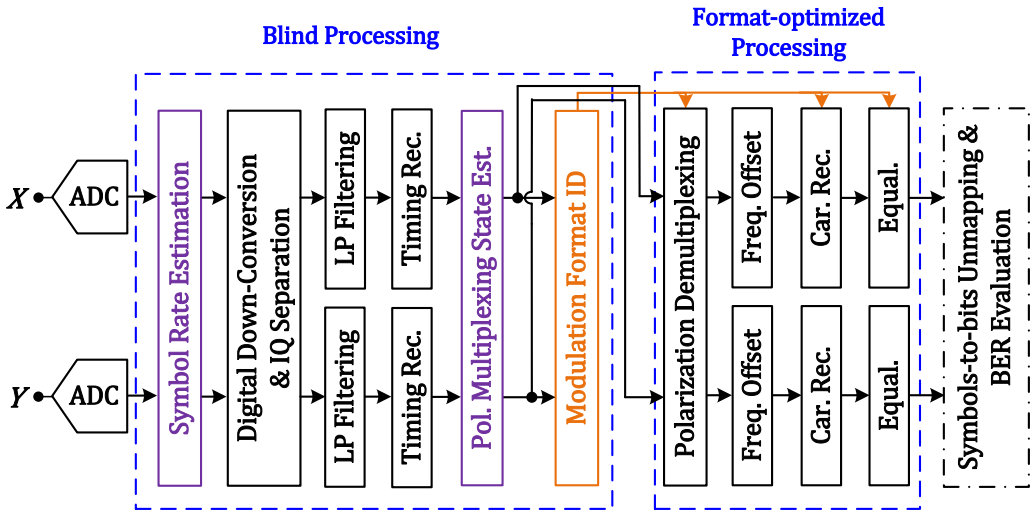

Fig. 4.9. Architecture of the autonomous receiver for polarization division multiplexing photonic assisted wireless communication links performing modulation format recognition.

Second, in the format-optimized module, polarization demultiplexing is first performed in the case of PDM enabled systems. Then, the processing steps are identical whether dealing with PDM enabled systems or not. These steps are: frequency offset removal, carrier phase recovery and equalization.

Note that a single implementation of the frequency offset removal, the carrier phase recovery and the equalization algorithms is suitable as the knowledge of the modulation format constellation is sufficient for decision-directed equalizations, thus simplifying the overall complexity of the architectural design.

This Chapter focuses on the blind parameters estimation algorithms contained in the blind processing module, such as symbol rate estimation, and MFR. Blind parameters estimation algorithms are discussed in Chapter 4 - Section 4.5. Other algorithms performed in the blind processing modules (timing recovery) and in the format-optimized processing module (polarization demultiplexing, frequency offset removal, carrier phase recovery and equalization) are detailed in Chapter 2 - Section 5.3. Digital-down conversion and I/Q separation algorithm is extensively covered in the literature.

4.5 BLIND PARAMETERS ESTIMATION ALGORITHMS

This Chapter focuses on the blind parameters estimation algorithms contained in the blind processing modules of autonomous receiver architectures designed for fiber optic communication links (Chapter 4 - Section 3) and for photonic assisted wireless communication links (Chapter 4 - Section 4).

Parameters estimated in the autonomous receivers' blind processing modules can be structured in two exclusive sets: link impairments parameters and signal parameters. Optical link impairments parameters consist of CD. This work does not cover blind estimation of wireless link impairments parameters. Signal parameters comprise of the symbol rate, the number of multiplexed polarizations, and the modulation format.

In this section, we investigate in details the blind parameters estimation algorithms. Chapter 4 - Section 5.1 studies the link impairments parameters estimation algorithms (CD estimation in the case of fiber optic links). Chapter 4 - Section 5.2 studies the signal parameters estimation algorithms (symbol rate, number of multiplexed polarizations). Chapter 4 - Section 5.3 investigates the different MFR algorithms.

4.5.1 LINK IMPAIRMENTS PARAMETERS ESTIMATION

Since this work does not cover blind estimation of wireless link impairments parameters, we will focus solely on optical link impairments parameters. Specifically, we investigate how to blindly estimate the total accumulated CD.

Blind Estimation of the Total Accumulated Chromatic Dispersion

To blindly identify the total accumulated CD, we used the low complexity estimation method described in [74]. The blind CD estimation algorithm is based on the principle that a perfectly dispersion-compensated optical signal exhibits a minimum amplitude variance.

In this method, the error criterion $\varepsilon_{\mathrm{CD}}$, which is a function of the signal variance, is evaluated for the signal compensated over a range of total accumulated CD values on both polarizations. The optimum CD compensation is found when the error criterion $\varepsilon_{\mathrm{CD}}$ is minimized, equivalently when the corresponding compensated optical signal yields a minimum BER. The error criterion ε_{CD} is given by:

$$\varepsilon_{CD} = \sum_{n} \left\{ \left| |x_{CD}[2n+1]|^2 - R_{x,1} \right| + \left| |x_{CD}[2n]|^2 - R_{x,2} \right| \right\}$$

$$+ \sum_{n} \left\{ \left| |\mathrm{y_{CD}}[2\mathrm{n}+1]|^2 - \mathrm{R_{y,1}} \right| + \left| |\mathrm{y_{CD}}[2\mathrm{n}]|^2 - \mathrm{R_{y,2}} \right| \right\}$$

Where x_{CD} and y_{CD} are CD compensated signals in the X and Y polarizations, and $R_{x,1}$, $R_{x,2}$, $R_{\mathrm{y},1}$, and $R_{\mathrm{y},2}$ are constants estimated from the power of odd and even samples in the

X and Y polarizations. Specifically, $R_{x,1} = \mathbf{E}[\,|x_{CD}[2n+1]|^{2}\,]$, $R_{x,2} = \mathbf{E}[\,|x_{CD}[2n]|^{2}\,]$, $R_{y,1} = \mathbf{E}[\,|y_{CD}[2n+1]|^{2}\,]$, and $R_{y,2} = \mathbf{E}[\,|y_{CD}[2n]|^{2}\,]$.

The block diagram of the total accumulated CD blind estimation algorithm is shown in Fig. 4.10.

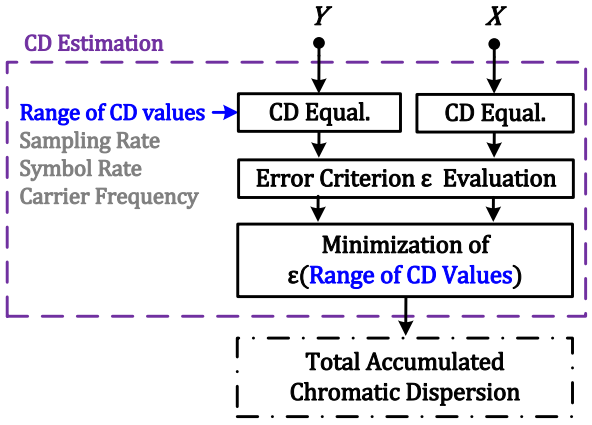

Fig. 4.10. Total accumulated chromatic dispersion blind estimation algorithm.

To minimize computational complexity, the CD compensation algorithm was implemented in the frequency domain using the overlap frequency domain equalization approach [36], which is based on the CD compensation in the frequency domain of overlapping blocks of data. The CD compensation algorithm implemented in the frequency domain using the overlap frequency domain equalization approach is detailed in Chapter 2 - Section 5.3.

Figure 4.11 illustrates the correlation between BER and the error criterion ε_{CD} over a range of compensated CD values near the expected total dispersion.

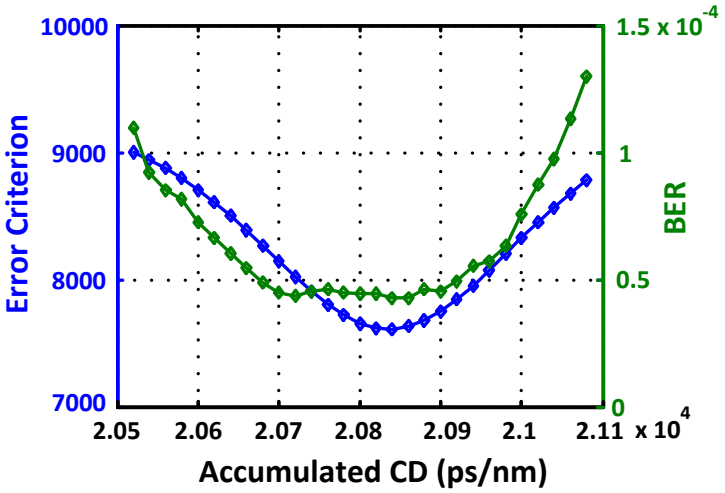

Fig. 4.11. Correlation between BER and signal amplitude variance over a range of compensated CD near the expected accumulated dispersion for a 32 GBaud-PDM-QPSK experimental signal after 1056 km transmission in large area fiber (OSNR = 22.4dB, launch power = 0dBm).

4.5.2 SIGNAL PARAMETERS ESTIMATION

We investigate how to blindly estimate the received signal's symbol rate and the number of multiplexed polarizations.

Blind Estimation of the Symbol Rate

To blindly estimate the received signal's symbol rate, we use a cyclic correlation based algorithm [81, 82].

Since our initial architecture presumes both polarizations are modulated at the same baud rate, then the algorithm only needs to be applied to one polarization. Typically the choice can be arbitrary however in the case of single polarization formats there is the possibility that one detected polarization possesses larger SNR and it is preferred to use this polarization. We use relative total signal power as a proxy for relative SNR. Hence, assuming noise power is the same in each polarization, the identification of the larger SNR polarization is done by calculating the polarization with the largest relative signal power.

The symbol rate is estimated by exploiting the cyclostationary random process nature of the signal. For the signal $x[k]$, digitized version of the received signal in the X polarization, the empirical estimate of the cyclic-correlation function at normalized frequency α and delay τ is given by:

$$\hat{r}_T{}^{(\alpha)}[\tau] = \frac{1}{T}\sum_{n=0}^{T-1} x[n+\tau]\,\bar{x}[n]e^{j2\pi\alpha n}$$

Where T is the number of $x[k]$ samples considered for calculating the cyclic-correlation function estimate, F_s is the sampling rate, and $\alpha = \frac{f}{F_s}$ is the normalized frequency.

The classical estimator $\hat{R}_T{}^{(\alpha)}$ is a vector whose components are estimates of the cyclic-correlation function of the signal evaluated over a range of delays $\tau \in [0;2N]$ at a fixed α. It is given by:

$$\hat{R}_T{}^{(\alpha)} = [\hat{r}_T{}^{(\alpha)}[0], \ldots, \hat{r}_T{}^{(\alpha)}[2N]]^{\,t}$$

For low excess bandwidth transmitter, the classical estimator can be inaccurate. Therefore, in such situations, a weighted version of the classical estimator can be defined with enhanced accuracy. The weighted version of the classical estimator $\hat{R}_T{}^{(\alpha)}$ is a vector given by:

$$\hat{S}_T{}^{(\alpha)} = \Gamma(\alpha)^{\,-1/2}\,\hat{R}_T{}^{(\alpha)}$$

Where $\Gamma(\alpha)$ is the asymptotic covariance matrix of the classical estimator $\hat{R}_T{}^{(\alpha)}$. In practice, the weighting matrix $\Gamma(\alpha)$ is estimated from the cyclic statistics of the observation at cyclic frequency 0. The coefficient (i, j) of the estimate $\hat{\Gamma}(a)$ of the weighting matrix is given by:

$$[\hat{\Gamma}(\alpha)]_{i,j} = z_1{}^{(\alpha)} * z_{2-}[j-i] \qquad \text{for i,j} \in [1;2N+1]$$

Where, for n ∈ [1, L]:

$z_1{}^{(\alpha)}$[n] = w[n]. $\overline{\hat{r}_T{}^{(0)}[n]}.\,e^{2\pi j\alpha n}$

$z_2[n]$ = w[n]. $\hat{r}_T{}^{(0)}[n]$

z_{2-}[n] = z_2[-n]

with w[n] the n^{th} sample of the Blackman window W_L of length L = 8N +1, i.e. W_L = [w[1],…,w[L]] ^{t}.

In wireless communication systems, the classical symbol rate estimator $\hat{R}_T{}^{(\alpha)}$ is based on the cyclic correlation function of the signal; however, we found it insufficient for optical communication systems due to the low excess bandwidth of the transmitter [81]. Consequently, we employ a weighted version of the classical estimator which includes corrective weights that are estimated from the cyclic statistics of the signal at cyclic frequency 0 [82]. The corrective weights used in the modified estimator $\hat{S}_T{}^{(\alpha)}$ are hardware dependent are primarily impacted by transmitter properties.

Maximization of the estimator's squared norm identifies the normalized symbol rate

$\alpha_0 = \frac{f_{symbol}}{F_s}$, and therefore the symbol rate. The maximization process is performed assuming that the symbol rate f_{symbol} is the only non-zero positive cyclic frequency.

We improve the robustness of the algorithm by first performing a coarse estimation and compensation of the CD followed by a rough resampling process to ensure that $\frac{f_{symbol}}{F_s} \in]0; 1/2[$. Imperfect coarse CD compensation has limited impact on the symbol rate estimation. However, large residual CD combined with low-OSNR regimes stress the estimation of the symbol rate.

We illustrate the maximization process of the squared norm of the classical estimator $\hat{R}_T^{(\alpha)}$, Fig. 4.12.a, and the weighted estimator $\hat{S}_T^{(\alpha)}$, Fig. 4.12.b, for an experimental 32Gb/s PDM-BPSK signal, with a 11 dB OSNR, acquired after 1056 km transmission in large-area fiber (LAF), and launched at +0dBm. The symbol rate peak detection fails in the case of the classical estimator but is non-ambiguous using the weighted estimator approach, demonstrating the superiority of the weighted estimator in the case of modern optical signals.

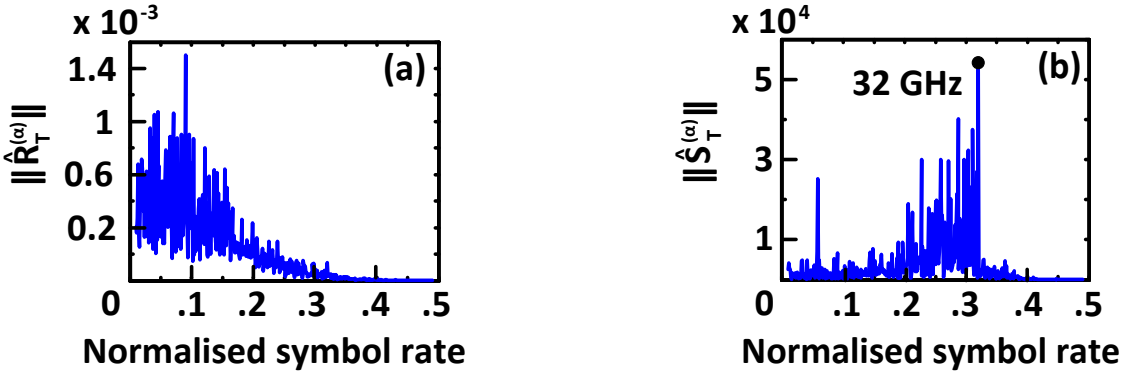

Fig. 4.12. Symbol rate peak detection for 32 Gb/s-PDM-BPSK experimental signal after 1056 km transmission in large area fiber (OSNR = 11 dB, launch power = 0 dBm) with: (a) Classical estimator; (b) Weighted estimator.

Importantly, the weighted estimator is robust over a wide range of formats and symbol rates. Indeed, by increasing the sweeping resolution of the normalized frequency α (decreasing the step size), finer symbol rates can be identified with increasing detectability (symbol rate peak amplitude increases as the sweeping step size decreases).

Blind Estimation of the Number of Multiplexed Polarizations

We have implicitly assumed that distinct data streams have been transmitted on each orthogonal polarization of the optical field although none of the prior steps is influenced by the number of modulated polarizations. However, before proceeding to MFR and to polarization demultiplexing, it is necessary to estimate if the signal is polarization

multiplexed or not. The number of multiplexed polarizations can be determined by performing a cross correlation between the received X and Y polarizations. If the cross correlation has a maximum at zero lag and several symmetric secondary maxima, Fig. 4.13.a, then the received signal is modulated on a single polarization and the polarization demultiplexing step can be skipped. Else, if the cross correlation signal displays multiple peaks for non-zero lags and a lack of symmetry, Fig. 4.13.b, then the received signal is polarization multiplexed and descrambling of the received polarizations is necessary.

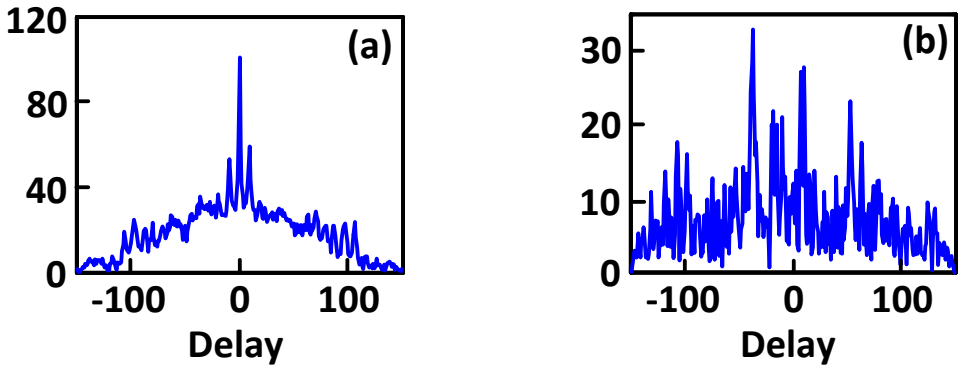

Fig. 4.13. Cross-correlation of received X and Y polarizations for experimental back-to-back signals. a) 28 Gb/s single-polarization OOK signal with a 19 dB OSNR. b) 32 Gb/s PDM-BPSK signal with a 17dB OSNR.

4.5.3 MODULATION FORMAT RECOGNITION

In the previous sections of this Chapter, we have investigated in details the designs of different architectures of autonomous receivers for fiber optic communication links (Chapter 4 - Section 3) and photonic assisted wireless communication links (Chapter 4 - Section 4). Depending on the incoming signal's modulation format category, we proposed an autonomous receiver architecture design that performs conventional MFR for fiber optic communication links, Fig. 4.1 (Chapter 4 - Section 3.1), and for photonic assisted wireless communication links, Figs. 4.7 and 4.9 (Chapter 4 - Section 4). Alternatively, we also proposed an autonomous receiver architecture design that performs time-domain hybrid

modulation format recognition for fiber optic communication links, Fig. 4.3 (Chapter 4 - Section 3.2).

In this section, we further examine how to blindly identify the modulation format of the incoming signal.

We segment MFR algorithms in two exclusive sets: conventional MFR and time-domain hybrid modulation format recognition. The conventional modulation format category is comprised of OOK, M-PSK, M-PAM, and M-QAM formats. The time-domain hybrid modulation formats category is comprised of all the possible TDHMFs composed with M-PSK and M-QAM.

Regardless of the modulation format, and whether referring to autonomous architectures for fiber optic communication links or photonic assisted wireless communication links, MFR occurs after the following processing steps have been performed: symbol rate estimation, CD estimation and equalization (in the case of fiber optic communication links), symbol timing recovery and estimation of the number of multiplexed polarizations.

We designed two distinct algorithms for performing conventional MFR. The first algorithm, called *higher order statistics-based modulation format recognition*, is exclusively based on higher order statistics (HOS). The second algorithm, called *Stokes space-based modulation format recognition*, uses Stokes space analysis and HOS.

For performing time-domain hybrid modulation format recognition, we designed one algorithm. The algorithm is based on the statistical distribution of the received signal's radius.

Conventional Modulation Format Identification: HOS-Based Modulation Format Recognition

Conventional MFR occurs in the autonomous architecture at a stage where signals are still polarization scrambled, Fig. 4.1. However, MFR must be performed on demultiplexed polarization for robust results.

The proposed MFR method is based on fourth-order cumulants which are characteristic signatures based on HOS of the received signal. It is designed to identify four modulation formats of interest (OOK, BPSK, QPSK, 16-QAM) although, in principle, the approach can be extended to any additional modulation format.

Each modulation format possess a distinct signature in the two dimensional I/Q plane. The goal is to recognize these format specific patterns to uniquely identify multiple modulation formats based only on the received signal samples. MFR is all the more challenging as format recognition and polarization demultiplexing are strongly interdependent. Furthermore format identification is dependent on the accuracy of the previous steps (CD estimation and compensation, timing recovery, estimation of the number of multiplexed polarizations).

However, at this point in the demodulation, the pattern of the symbols in the I/Q plane is neither organized nor reliable because, the polarizations are still scrambled in the case of PDM signals, and the received signal still contains undesired phase errors such as the frequency offset between the transmitter and the receiver LO lasers or the transmitter laser-LO phase noise contribution.

Therefore, our proposed HOS-based conventional MFR algorithm is organized in three consecutives steps: i) Blind Polarization Demultiplexing, ii) Frequency Offset Removal and Carrier Phase Recovery, and iii) Modulation Format Identification.

For the case of PDM signals, we perform a preliminary polarization demultiplexing stage prior to identifying the received signal's modulation format unique signature. The polarization demultiplexing method allows effective, although not optimal demultiplexing for a wide range of possible modulation formats.

In the case of single-polarization signals, the SOP of the received signal can be aligned using the maximal-ratio polarization combining process [108].

Then frequency offset removal and carrier phase recovery are performed to minimize the deterministic phase offset and the impact of phase noise.

The major steps of the HOS-based MFR method for PDM signals are summarized in Fig. 4.14.

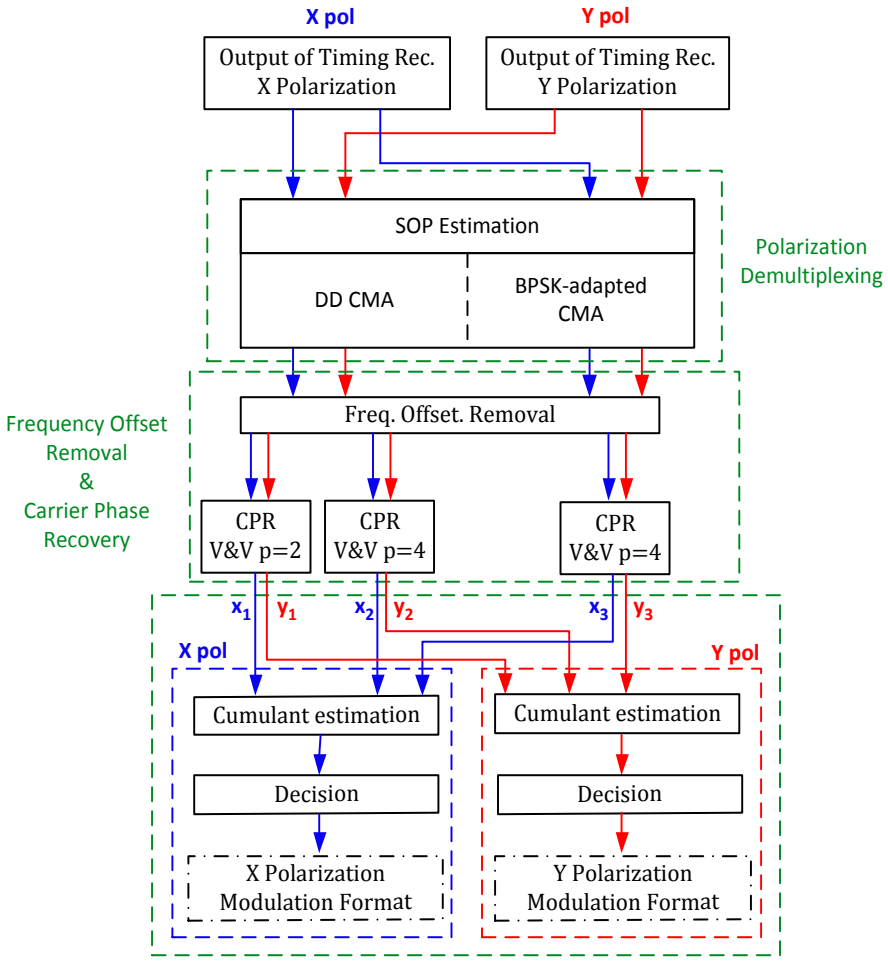

Fig. 4.14. Higher order statistics-based conventional modulation format recognition method for polarization division multiplexing signals.

Blind Polarization Demultiplexing

Different modulation formats have different optimum polarization demultiplexing algorithms. The CMA [47] while often functional is not optimum for constellations that do not have constant modulus. Additionally, conventional CMA equalization can fail for BPSK signals [75]. On the other hand, the ICA-based polarization demultiplexing technique [48], although optimum for QPSK, 16-QAM and many other higher-order constellations, is not optimum for OOK and BPSK. We note that we ensure that each sampled data stream is normalized to have unit energy to improve performance of all formats.

The conventional CMA-based polarization demultiplexing algorithm [47] aims at estimating the inverse $\boldsymbol{J}^{-1}$ of the Jones matrix $\boldsymbol{J}$, such that the output signals x_{out} and y_{out} of the algorithm become equal to the input signals to the fiber link. The following relationship between the input signals (x_{in}; y_{in}) and output signals (x_{out}; y_{out}) of the CMA-based polarization demultiplexing algorithm, models the polarization unscrambling process:

$$\begin{pmatrix} x_{out} \\ y_{out} \end{pmatrix} = \boldsymbol{J}^{-1} \begin{pmatrix} x_{in} \\ y_{in} \end{pmatrix} \Leftrightarrow \begin{pmatrix} x_{out} \\ y_{out} \end{pmatrix} = \begin{pmatrix} p_{xx} & p_{xy} \\ p_{yx} & p_{yy} \end{pmatrix} \begin{pmatrix} x_{in} \\ y_{in} \end{pmatrix}$$

The matrix elements are updated symbol by symbol according to the equation:

$$\begin{pmatrix} p_{xx}[n+1] \\ p_{xy}[n+1] \end{pmatrix} = \begin{pmatrix} p_{xx}[n] \\ p_{xy}[n] \end{pmatrix} + \mu . e_x[n] . \begin{pmatrix} \overline{x_{in}[n]} \\ \overline{y_{in}[n]} \end{pmatrix}$$

Where e_x[n] = $(C^2 - |x_{out}[n]|^2)x_{out}[n]$ is the X polarization error signal, C is a constant modulus, and μ the step-size parameter. The conventional CMA-based polarization demultiplexing algorithm uses a constant modulus C = 1, thus obtaining the Godard algorithm [49]. A similar equation is used for updating p_{yx} and p_{yy}.

The BPSK-adapted CMA-based polarization demultiplexing algorithm [75] utilizes the same model as the conventional CMA equalizer but different update equations and

different error signals. Additionally, the constant modulus coefficient is modified to account for the frequency offset between the transmitter and the receiver lasers.

For optimum format identification we first perform a polarization demultiplexing method which is not optimum for BER performance but can robustly manage any format. Specifically, we run a pair of "complementary" CMA-inspired methods in parallel to cover all possible modulation formats.

The first method ("SOP Estimation: DD CMA", Fig. 4.14) is a decision-directed implementation of the CMA equalizer. Adaptive filtering decisions are made depending on X & Y polarizations' equalized output symbols. Specifically, we define an adaptation threshold T controlling the matrix elements update equation:

$$\text{If } \begin{cases} |x_{out}[n]| \geq T, \text{then } \begin{pmatrix} p_{xx}[n+1] \\ p_{xy}[n+1] \end{pmatrix} = \begin{pmatrix} p_{xx}[n] \\ p_{xy}[n] \end{pmatrix} + \mu . e_x[n] . \begin{pmatrix} \overline{x_{in}[n]} \\ \overline{y_{in}[n]} \end{pmatrix} \\ |x_{out}[n]| < T, \text{then } \begin{pmatrix} p_{xx}[n+1] \\ p_{xy}[n+1] \end{pmatrix} = \begin{pmatrix} p_{xx}[n] \\ p_{xy}[n] \end{pmatrix} \end{cases}$$

A similar equation is used for updating p_{yx} and p_{yy}.

Decision-directed adaptation avoids severe distortion of the OOK constellation that may compromise the subsequent MFR. The implemented method uses 5 tap filters with an adaption threshold T = 1/2. The algorithm is not optimal but gives robust results for demultiplexing the X and Y polarizations for OOK, QPSK, and 16-QAM formats.

The second method ("SOP Estimation: BPSK-adapted CMA", Fig. 4.14) is a decision-directed implementation of the adaptive equalizer for BPSK signals. The approach is identical to the decision-directed implementation of the CMA equalizer previously described. The implemented method uses 5 tap filters with an adaption threshold T = 1/2. This algorithm is exceedingly robust for BPSK signals and typically fails for OOK, QPSK and 16-QAM.

Frequency Offset Removal and Carrier Phase Recovery

The frequency offset between the source and the receiver (LO) lasers results in a continuously increasing or decreasing phase; normalized constellation is spinning in time. This offset is minimized using a conventional approach [51].

Specifically, examination of the signal in the Fourier domain reveals the nearly constant frequency offset between the transmitter and the LO lasers. This method requires the neutralization of the phase modulation contribution prior to the Fourier analysis, which typically, can be achieved by raising the signal to a specific power p which depends on the modulation format.

For polarization multiplexed, signals the frequency offset removal algorithm is applied on both demultiplexed X and Y polarizations; otherwise it is only applied on one polarization and the other is ignored.

Despite these efforts a phase error remains due to the imperfect estimation of the frequency offset and the random phase difference between the transmitter and the LO lasers. This phase error is conventionally tracked using the Viterbi-Viterbi algorithm [77] which requires efficient prior polarization demultiplexing.

Based on this observation, we apply selectively the Viterbi-Viterbi algorithm on parallel output signals of the frequency offset removal algorithm and obtain multiple signals for each possible choice of blind polarization demultiplexing algorithm combined with different choices of power p in the carrier phase recovery algorithm (Fig. 4.14).

The selection of the appropriate blind polarization demultiplexing algorithm combined with the correct choice of power p in the Viterbi-Viterbi algorithm enables the recovery of a quasi-stationary constellation hence unlocking the modulation format signature.

Modulation Format Identification

The modulation format is identified using a two-step scheme based on a hierarchical approach using HOS [109] and is applied independently on each polarization of the output signal of the frequency offset removal algorithm.

(1) Generation of normalized estimates of fourth-order cumulants

Firstly, we use HOS to generate a set of statistics, specifically fourth-order cumulants, that enable the distinction between the possible signal modulation formats. For noiseless, stationary and normalized constellations, the ith fourth-order cumulants $C_{4,i}$ of the signal (assuming a complex valued stationary random process) take unique values for a given modulation format (Table 4.1).

Table 4.1. Theoretical Fourth-Order Cumulant Values for noiseless, stationary, and normalized constellations of interest.

	$\|\|C_{4,0}\|\|$	$\|\|C_{4,1}\|\|$	$\|\|C_{4,2}\|\|$
OOK	1	1	1
BPSK	2	2	2
QPSK	1	0	1
16-QAM	0.68	0	0.68

In our architecture, fourth-order cumulants are estimated from the different output signals of the carrier phase recovery algorithms.

Specifically, consider the X polarization output signals $x_1[k]$, $x_2[k]$ and $x_3[k]$ of the carrier phase recovery algorithms in the blind processing stage of the architecture (see Fig. 4.14). $x_1[k]$ is obtained after executing the DD CMA-based blind polarization demultiplexing algorithm, the frequency offset removal and the Viterbi-Viterbi carrier phase recovery algorithm with the power p chosen equal to 2. $x_2[k]$ is obtained after executing the DD CMA-based blind polarization demultiplexing algorithm, the frequency offset removal and the Viterbi-Viterbi carrier phase recovery algorithm with the power p chosen equal to 4. $x_3[k]$ is obtained after executing the BPSK-adapted CMA-based blind

polarization demultiplexing algorithm, the frequency offset removal and the Viterbi-Viterbi carrier phase recovery algorithm with the power p chosen equal to 4.

To mitigate the effects of ASE noise, we use a corrective term in the fourth-order cumulant estimates. The normalized estimate $\tilde{C}_{4,i}{}^{n}$ of the ith fourth-order cumulant $C_{4,i}{}^{n}$ of $x_n[k]$ (assuming a complex valued stationary random process) is expressed as:

$$\tilde{C}_{4i}{}^{n} = \frac{\hat{C}_{4i}{}^{n}}{(\hat{C}_{21}{}^{n} - \hat{C}_{21,\ g}{}^{n})^{2}}$$

Where: the sub-index i is the fourth-order cumulant index (i= 0,1,2) and the super-index n is the carrier phase recovery output signal label (n = 1,2,3 – Fig. 4.14); $\hat{C}_{4i}{}^{n}$ is the estimator of the ith fourth-order cumulant $C_{4,i}{}^{n}$ [109]; $\hat{C}_{21}{}^{n}$ is the estimator of the second-order moment $C_{21}{}^{n}$ and is given by: $\hat{C}_{21}{}^{n} = \frac{1}{N}\sum_{k=1}^{N} |x_n[k]|^2$; N is the length of $x_n[k]$; $\hat{C}_{21,\ g}{}^{n}$ is the estimator of the additive white Gaussian noise average power in the signal $x_n[k]$, and can be expressed as:

$$\hat{C}_{21,\ g}{}^{n} = \hat{C}_{21}{}^{n} . 10^{-\frac{SNR^{Xpol}{}_{dB}}{10}}$$

With: $SNR^{Xpol}{}_{dB}$ the SNR in the X polarization expressed in dB.

To estimate $SNR^{Xpol}{}_{dB}$ (and $SNR^{Ypol}{}_{dB}$), we use the following ideal relation linking the SNR and the OSNR [13] in the linear scale:

$$OSNR_{lin} = \frac{f_{symbol}}{2B_{ref}} SNR_{\ lin} = \frac{q}{2}\frac{f_{symbol}}{B_{ref}} SNR^{Xpol}{}_{lin}$$

Where: q is the number of SOP of the signal (q=2 for PDM signals, or q=1 for single polarization signals); f_{symbol} is the symbol rate (Baud); B_{ref} is the reference bandwidth (12.5 GHz); *lin* is the index for expression in linear scale.

The relationship between SNR and OSNR assumes matched filtering and that the noise energy is equivalent to the spectral density of ASE in one polarization.

Note that only knowledge of the approximate OSNR of the signal is required for the fourth-order cumulants generation.

(2) Decision process and identification of the modulation format

The second step uses the generated normalized estimates $\{\{\tilde{C}_{4,i}{}^{n}\}_{i=0,1,2}\}_{n=1,2,3}$ to make a sequence of decisions to uniquely identify the modulation format in each polarization using the hierarchical approach of Fig. 4.15. Our decision thresholds are those for noiseless, stationary and normalized constellations.

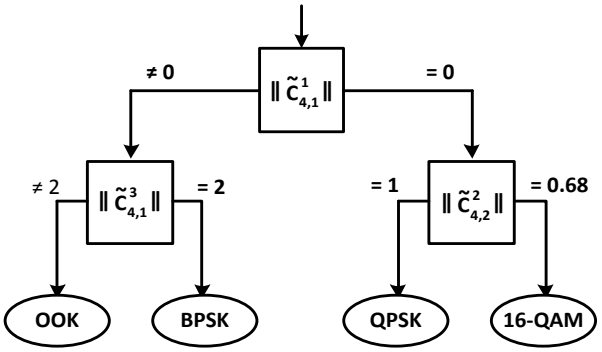

Fig. 4.15. Cumulants-based decision process used in the higher order statistics-based conventional modulation format recognition method.

The execution of the modulation format identification algorithm terminates the HOS-based conventional MFR algorithm.

As a conclusion to this section, it should be noted that HOS-based conventional MFR will be all the more challenged as residual CD, PDL, channel nonlinearities and/or DGD increase, in particular if CMA-inspired methods are not properly calibrated, in terms of tap length and/or tap weights, to the expected amount of DGD applied to the incoming signal.

<u>Conventional Modulation Format Identification: Stokes Space-Based Modulation Format Recognition</u>

Conventional MFR occurs in the autonomous architecture at a stage where signals are still polarization scrambled, Fig. 4.1. However, MFR must be performed on demultiplexed polarization for robust results.

The proposed MFR method is based on a hybrid method combining Stokes space analysis with HOS. It is designed to identify OOK, M-PSK, M-PAM, and M-QAM signals.

The Stokes space-based conventional MFR algorithm operates on the digitized X (signal 1) and Y polarizations (signal 2), resampled after timing recovery to 1 sample/symbol at maximum eye opening, of the incoming PDM signal, Fig. 4.16.

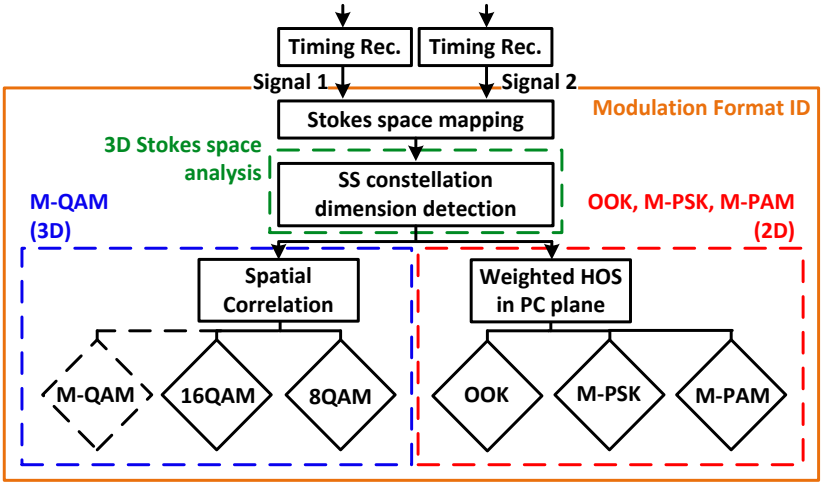

Fig. 4.16. Stokes space-based modulation format recognition method. First, the incoming signal is mapped to Stokes space. Second, the constellation dimension is used to distinguish between {M-QAM} ($M \neq \{2, 4\}$) and {OOK + M-PSK + M-PAM}. Third, {OOK + M-PSK + M-PAM} formats are further distinguished using higher order statistics, whereas {M-QAM} formats are separately distinguished via a spatial cross-correlation method.

In the case of a received single polarization signal, the MFR algorithm operates on an emulated PDM signal. Specifically, the even symbols are used to create a virtual X polarization (signal 1) while the virtual Y polarization contains the odd symbols (signal 2). For optimum performance, the virtual X and Y polarizations signals are truncated over a time period during which the SOP of the received single polarization signal is fixed.

Thus, to identify formats amongst OOK, M-PSK, M-PAM, and M-QAM, the Stokes space-based conventional MFR method, Fig. 4.16, operates in three consecutive steps: i) Stokes space mapping, ii) estimation of the Stokes space constellation dimension, and iii) format recognition among either {OOK + M-PSK + M-PAM} formats or {M-QAM} formats.

Stokes space mapping

Stokes parameters fully describe the electric field properties, including total power and SOP. Stokes parameters can be calculated from samples (to include symbols transitions information), or from symbols of the received signal. Noting $x[k]$ ($y[k]$) the X (Y) polarization received digital signal, the 4-dimensional Stokes vector $\vec{s}$, which contains the Stokes parameters, is determined in the conventional manner:

$$\vec{s}[k] = \begin{pmatrix} s_0[k] \\ s_1[k] \\ s_2[k] \\ s_3[k] \end{pmatrix} = \begin{pmatrix} x[k]^2 + y[k]^2 \\ x[k]^2 - y[k]^2 \\ 2Re\{x\bar{y}\} \\ 2Im\{x\bar{y}\} \end{pmatrix}$$

The 3-dimensional sub-vector $(s_1\ s_2\ s_3)^t$ is used to visualize the received signal SOP on the Poincaré sphere. Stokes space constellations are the representation of the sub-vector $(s_1\ s_2\ s_3)^t$ in a 3-dimensional space, and are contained in a lens-like surface [110].

The proposed MFR method maps the received signals' symbols to Stokes space, obtaining a Stokes space constellation comprised of clusters corresponding to the nominally discrete set of allowed electric fields.

There are multiple advantages for performing MFR in Stokes space: first, the mapping process is unique to a modulation format whose signature is expanded in a 3-dimensional space, allowing unique identification. Second, the polarization demultiplexing process is bypassed because the Stokes space constellation is independent of the received SOP, since the variation of the received SOP will simply cause a rotation of the Stokes space constellation with time [110]. Finally, the mapping process is independent of the

residual carrier-LO frequency and phase offsets contained in the received signal.

On the other hand, performing MFR in Stokes space presents some challenges. Indeed, Stokes space constellations are sensitive to noise, since Stokes space mapping distorts the noise PDF [88]. Moreover, Stokes space constellations are perturbed by PMD, and PDL [110, 111], which are common within optical fiber systems. Channel nonlinearities also impact Stokes space constellations.

Note that in the case of a received single polarization signal, the emulated PDM signal satisfies the first and third properties of Stokes space-based MFR mentioned above. Additionally, the emulation of the PDM signal waives the limitations resulting from PMD or PDL.

Stokes space constellation dimension estimation

In theory, each Stokes space constellation has a plane of symmetry. The study of ideal noiseless Stokes space constellations leads to a natural distinction between 2-dimensional constellations that are wholly contained in a symmetry plane in Stokes space (OOK, M-PSK, M-PAM) and 3-dimensional constellations (M-QAM with $M \neq \{2, 4\}$), Fig. 4.17.

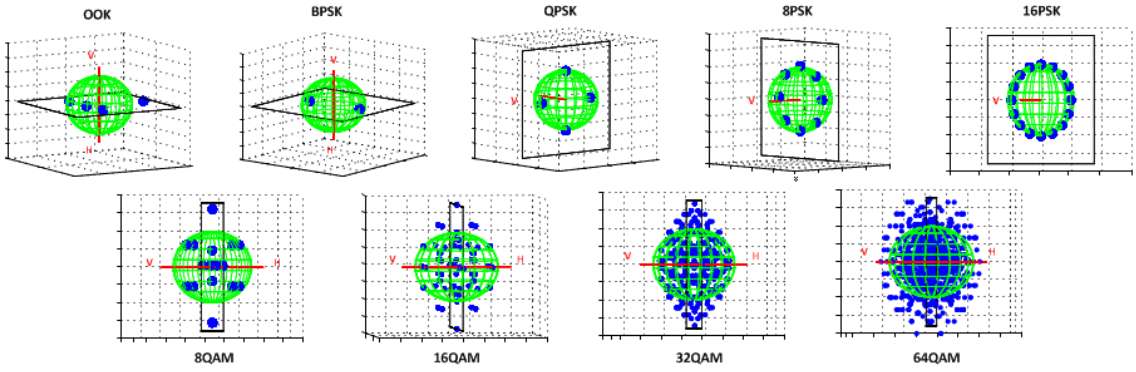

Fig. 4.17. Ideal noiseless Stokes space constellations for different modulation formats. OOK, M-PSK, and M-PAM are 2-dimensional, whereas M-QAM (with $M \neq \{2, 4\}$) are 3-dimensional.

We use this property to distinguish 2-dimensional from 3-dimensional Stokes space constellations by evaluating the absolute distance of Stokes space constellation clusters' mean positions relative to the symmetry plane P.

Hence, the first decision of the proposed MFR algorithm is to detect the dimension of the Stokes space constellation to distinguish if the received signal modulation format is amongst {OOK + M-PSK + M-PAM} or {M-QAM}.

To first estimate the 2-dimensional linear plane P, we implemented the PCA method. In Stokes space, projected clusters on P have the characteristic of exhibiting a maximized variance. So, using PCA, we search for the principal components that maximize the projected data variance. The main advantage of PCA lies in its robustness to noise variance. Consequently, the plane Q spanned by the first two principal components enables a better estimation of the symmetry plane P than the least-squares plane (we found the existence of degenerate cases using the least-squares method, Fig. 4.18).

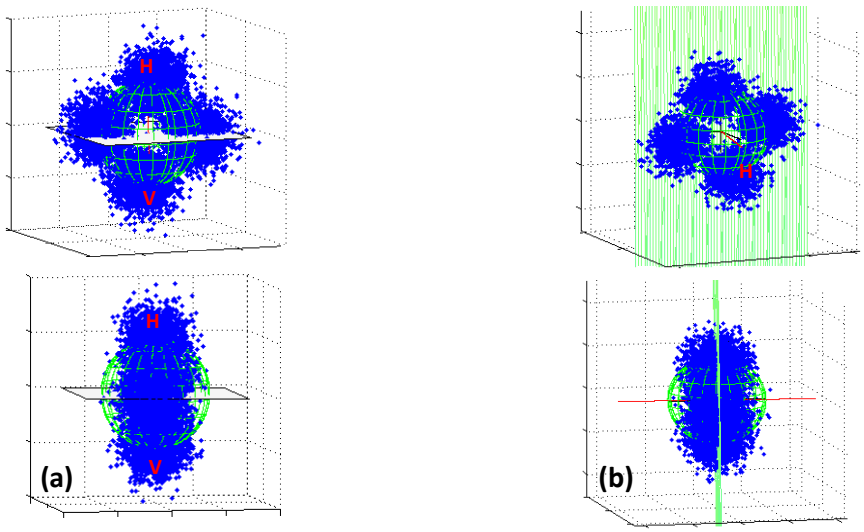

Fig. 4.18. 32 Gbaud-PDM-QPSK signal in the back-to-back configuration with a received OSNR of 20dB represented in Stokes space with the estimate of its symmetry plane using: (a) the least-squares method; (b) the principal component analysis method.

After having identified the estimate Q of the symmetry plane P, we define a coefficient d that serves as a proxy to estimate the dimension of the Stokes space constellation.

In a similar approach as the one introduced by Borkowski et al. [86, 87], we assume that the 3-dimensional Stokes space constellation cluster distribution follows a Gaussian mixture model (GMM), and identify the 3-dimensional Stokes space clusters parameters (mean position $\vec{\mu}_i$ and Dirichlet concentration parameter λ_i of the ith cluster) by applying a machine learning algorithm (variational Bayesian expectation maximization for GMMs) [112], Fig. 4.19.a.

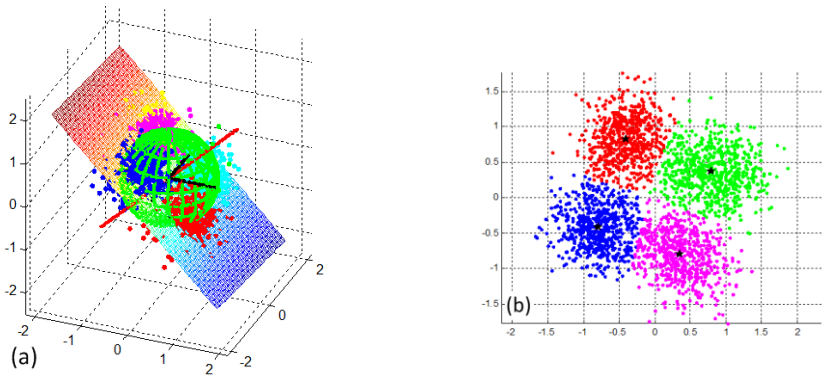

Fig. 4.19. 32 Gbaud-PDM-QPSK signal after 810 km transmission in large area fiber at 0dBm launch power with a received OSNR of 22dB: (a) represented in Stokes space with the estimate Q of its symmetry plane; (b) represented after projection on the plane Q.

The coefficient d evaluates the aggregate squared distance of projected clusters mean positions on the straight line Q $^{\perp}$ orthogonal to the plane Q spanned by the first two principal components, and is given by: $d = \sum_{cluster\ i} \alpha_i | < \vec{\mu}_i, \vec{u} > |^2$, where: $\vec{u}$ is the unitary vector of Q $^{\perp}$, $\vec{\mu}_i$ and α_i (= λ_i / $\sum_i \lambda_i$) the mean position and the weight of the ith cluster respectively.

Theoretical values of the coefficient d for ideal noiseless Stokes space constellation are summarized in Table 4.2, showing that, 2-dimensional Stokes space constellations (OOK,

M-PSK, M-PAM) exhibit $d = 0$, thus allowing discrimination from 3-dimensional constellations (M-QAM with $M \neq \{2, 4\}$) which exhibit $d \neq 0$.

Table 4.2. Theoretical values of the coefficient d for ideal noiseless Stokes space constellations.

Format	OOK	M-PSK	M-PAM	8QAM	16QAM	64QAM
d	0	0	0	0.1648	0.1720	0.1966

Format recognition

At this point in the MFR algorithm, we have mapped the received signal to Stokes space, identified the estimate Q of the symmetry plane P of the Stokes space constellation, and determined if the latter is 2-dimensional (OOK, M-PSK, M-PAM) or 3-dimensional (M-QAM with $M \neq \{2, 4\}$).

Next, we need to identify in each situation the final modulation format of the received signal.

(1) Amongst {OOK + M-PSK + M-PAM}

To discriminate modulation formats within {OOK + M-PSK + M-PAM} (2-dimensional Stokes space constellations), we developed a method based on HOS and GMMs.

HOS provides a statistical toolset that enables the identification of a signal's modulation format by capturing its unique statistical signature in the signal constellation diagram. Conventionally, the statistical signature of the modulation format is captured from the signal constellation represented in the I/Q plane. But in our method, the modulation format statistical signature is captured from the signal constellation represented in the estimate Q of the symmetry plane P of the Stokes space constellation.

We initiate the method with the orthogonal projection of 3-dimensional Stokes space data points on the plane Q, and obtain a distribution of 2-dimensional projected

clusters. Each projected cluster can be considered as a symbol with complex-valued coordinates in the plane Q. We assume that the 2-dimensional projected clusters coordinates in the plane Q is a stationary random process, with zero-mean.

Then, assuming the 2-dimensional projected clusters coordinates distribution follows a GMM, we identify their parameters in the plane Q (mean position $\vec{\mu}_{Q,i}$ and Dirichlet concentration parameter $\lambda_{Q,i}$ of the ith cluster) by applying the same machine learning algorithm as previously, Fig. 4.19.b.

Conventional normalized estimates $\{\tilde{C}_{4,i}\}$ of fourth-order cumulants $\{C_{4,i}\}$ can be calculated to make a sequence of decisions to uniquely identify the modulation format.

We can express the normalized estimate $\tilde{C}_{4,i}$ of the ith fourth-order cumulant $C_{4,i}$ of the 2-dimensional projected clusters coordinates in the plane Q as:

$$\tilde{C}_{4,i} = \hat{C}_{4,i} / \hat{C}_{2,1}{}^{2}$$

Where: $\hat{C}_{21}$ is the estimator of the second-order moment $C_{2,1}$ and is given by: $\hat{C}_{2,1} = \frac{1}{N}\sum_{k=1}^{N} |z[k]|^2$; with $z[k]$ the complex-valued coordinate of the kth 2-dimensional projected cluster in the plane Q, and *N* the number of considered 2-dimensional projected clusters in the plane Q.

In the general case, we can define estimators $\hat{C}_{4,i}$ as a function of the complex-valued coordinates $\{z[k]\}$ of the *N* 2-dimensional projected clusters in the plane Q. For example, the estimate $\hat{C}_{4,2}$ of the 2nd fourth-order cumulant $C_{4,2}$ is expressed as: $\hat{C}_{4,2} = \frac{1}{N}\sum_{k=1}^{N} |z[k]|^4 - |\hat{C}_{2,0}|^2 - 2\hat{C}_{2,1}{}^{2}$, where: $\hat{C}_{2,0} = \frac{1}{N}\sum_{k=1}^{N} z[k]^2$; with $z[k]$ the complex-valued coordinate of the kth 2-dimensional projected cluster in the plane Q, and *N* the number of considered 2-dimensional projected clusters in the plane Q.

We improve the performance of the cumulants-based modulation format identification method by reformulating conventional normalized estimates $\{\tilde{C}_{4,i}\}$ in order to take into account of the 2-dimensional projected clusters mean positions $\{\vec{\mu}_{Q,i}\}$ and

weights $\{\alpha_{Q,i}\}$ ($\alpha_{Q,i} = \lambda_{Q,i} \,/\, \sum_i \lambda_{Q,i}$). The modified statistics, introduced as normalized weighted estimates $\{\tilde{C}_{4,i,w}\}$ of fourth-order cumulants $\{C_{4,i}\}$, provide a more reliable interpretation of the statistics of the distribution of the projected constellation in the plane Q.

We express the normalized weighted estimate $\tilde{C}_{4,i,w}$ of the i[th] fourth-order cumulant $C_{4,i}$ of the 2-dimensional projected clusters coordinates in the plane Q as:

$$\tilde{C}_{4,i,w} = \hat{C}_{4,i,w} / \hat{C}_{2,1,w}^{\,2}$$

Where: $\hat{C}_{4,i,w}$ is the weighted estimate of the i[th] fourth-order cumulant $C_{4,i}$; $\hat{C}_{2,1,w}$ is the weighted estimate of the second-order moment $C_{2,1}$ and is given by: $\hat{C}_{2,1,w} = \sum_{cluster\ i} \alpha_{Q,i} \left|\mu_{Q,i}\right|^2$.

We can define estimators $\hat{C}_{4,i,w}$ as a function of the complex-valued coordinates $\{z[k]\}$ of the N 2-dimensional projected clusters in the plane Q, and the 2-dimensional projected clusters mean positions $\{\vec{\mu}_{Q,i}\}$ and weights $\{\alpha_{Q,i}\}$. For example, the normalized weighted estimate $\tilde{C}_{4,2,w}$ of the 2[nd] fourth-order cumulant $C_{4,2}$ can be express as:

$$\tilde{C}_{4,2,w} = \hat{C}_{4,2,w} / \hat{C}_{2,1,w}^{\,2}$$

Where: $\begin{cases} \hat{C}_{4,2,w} = \sum_{cluster\ i} \alpha_{Q,i} \left|\mu_{Q,i}\right|^4 - \left|\hat{C}_{2,0,w}\right|^2 - 2\hat{C}_{2,1,w}^{\,2} \\ \hat{C}_{2,0,w} = \sum_{cluster\ i} \alpha_{Q,i}\, \mu_{Q,i}^{\,2};\ \hat{C}_{2,1,w} = \sum_{cluster\ i} \alpha_{Q,i} \left|\mu_{Q,i}\right|^2 \end{cases}$

Finally, to identify the signal modulation format among OOK, M-PSK, and M-PAM, normalized weighted estimates $\tilde{c}_{4,i,w}$ of fourth-order cumulants are employed in a hierarchical classification scheme, similar to the approach presented by Swami et al. [109]. Figure 4.20 illustrates the normalized weighted estimates $\tilde{c}_{4,i,w}$ involved in the hierarchical classification scheme used to identify OOK, BPSK, and QPSK. The theoretical magnitudes of the normalized weighted estimates $\tilde{c}_{4,i,w}$ of fourth-order cumulants are summarized in Table 4.3 for OOK, BPSK, and QPSK.

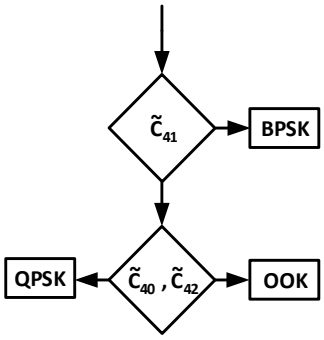

Fig. 4.20. Decision metrics used in the proposed Stokes space-based modulation format recognition method for identifying OOK, BPSK, and QPSK.

Table 4.3. Theoretical magnitudes of the normalized weighted estimates of fourth-order cumulants for ideal noiseless Stokes space constellations.

Format	OOK	BPSK	QPSK
$\lvert\tilde{C}_{4,0,w}\rvert$	~0.56	2	1
$\lvert\tilde{C}_{4,1,w}\rvert$	0	2	0
$\lvert\tilde{C}_{4,2,w}\rvert$	~0.72	2	-1

(2) Amongst {M-QAM} ($M \neq \{2, 4\}$)

To discriminate modulation formats within {M-QAM} with $M \neq \{2, 4\}$ (3-dimensional Stokes space constellations), we use a cross-product statistic Γ_{XY}, defined as spatial cross-correlation index, inspired from spatial autocorrelation models [113]. The

spatial cross-correlation index Γ_{XY} evaluates, in the 3-dimensional Stokes space, the correlation between the mapped signal (observation X) and a given reference M-QAM Stokes space constellation (observation Y). Γ_{XY} is based on the deviation between the two sets of observations X and Y, and is given by: $\Gamma_{XY} = \sum_{i,j} d_{i,j} \; / \; \sum_{i,j} \frac{1}{d_{i,j}}$, where $d_{i,j}$ is the Euclidian distance between observations $(x_i, y_j) \in$ (X,Y).

Spatial observations sets X and Y are highly correlated as the spatial cross-correlation index Γ_{XY} tends to 0.

Because the variation of the received SOP will cause a rotation of the Stokes space constellation (observation X) with time, we need to ensure observations sets X and Y are spatially synchronized (i.e. have a maximum of overlap in space) prior calculating Γ_{XY}. Overlapping observations sets X and Y in space is performed in two steps: first by aligning the observations sets respective symmetry planes, and then, by rotating one observation set with respect to the other one, around the normal to the aligned symmetry planes, to minimize the sum of squared errors between each pair of observations (x_i, y_k) (with y_k = arg $\min_{y_j}\{d_{i,j}\}$ = { $y_j \mid \forall\, y_l : d_{i,j} \leq d_{i,l}$ } : the closest observation $y_k \in$ Y to $x_i \in$ X).

After having calculated the cross-correlation indices Γ_{XY} between the mapped signal and multiple reference M-QAM Stokes space constellations, the identification of the M-QAM format is given by the minimization of the multiple normalized cross-correlation indices.

As a conclusion to this section, it should be noted that, because the proposed MFR method is based in Stokes space, accurate format identification will be all the more challenged as residual CD, DGD, PDL, and/or channel nonlinearities increase.

Time-Domain Hybrid Modulation Format Recognition

Unlike conventional MFR which occurs in the autonomous architecture at a stage where signals are still polarization scrambled, Fig. 4.3, time-domain hybrid modulation

format recognition occurs in the autonomous architecture on polarization demultiplexed signals, Figs. 4.7 and 4.9.

To demodulate a received TDHMF signal, the receiver requires knowledge of the pattern length, composing modulation formats, their ratio in the pattern, and the pattern arrangement in time. For example, if the TDHMF is BPSK2-QPSK3, then the frame length is 5, the constituent modulation formats are BPSK and QPSK, their ratio on the hybrid pattern are (2,3) and the hybrid pattern time-arrangement can be BPSK-BPSK-QPSK-QPSK-QPSK, or BPSK-QPSK-BPSK-QPSK-QPSK.

The proposed algorithm for time-domain hybrid modulation format recognition, Fig. 4.21, is based on the statistical distribution of the received signal's radius. It proceeds in three phases: i) first, the pattern length of the TDHMF is determined, ii) the composing modulation formats and their ratio in the pattern are estimated, and iii) the pattern arrangement in time is identified.

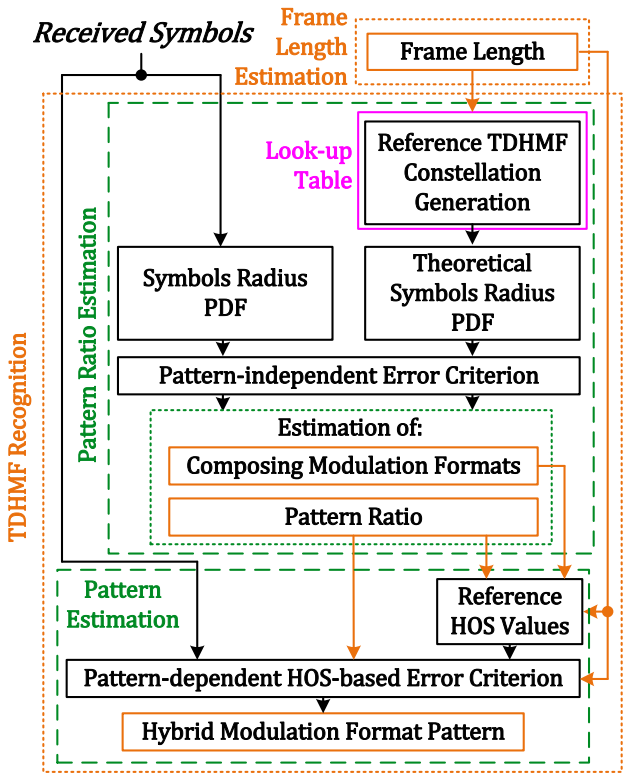

Fig. 4.21. Block diagram of the time-domain hybrid modulation format recognition algorithm.

Time-domain hybrid modulation format pattern length estimation

TDHMF pattern length estimation determine the number of symbol in the TDHMF's pattern.

The estimation of the format pattern length can be performed before polarization demultiplexing, Fig. 4.3. As a matter of fact, we use this feature in the autonomous receiver architecture performing conventional and time-domain hybrid modulation format recognition, Fig. 4.21, to not only determine the number of symbol in the TDHMF's pattern, but also to determine if the modulation format is conventional (unit frame length) or time-domain hybrid.

The proposed algorithm to estimate the frame length is shown in Fig. 4.22. By evaluating the modulus of the received signal time-series in the Fourier domain, the frequency-offset tone resulting from the imperfect locking of the transmitter laser and the LO vanishes. Remaining is a significant tone resulting from the pattern periodicity that we use to estimate the TDHMF frame length. The absence of a significant tone indicates that the modulation format is not hybrid but conventional (unit frame length).

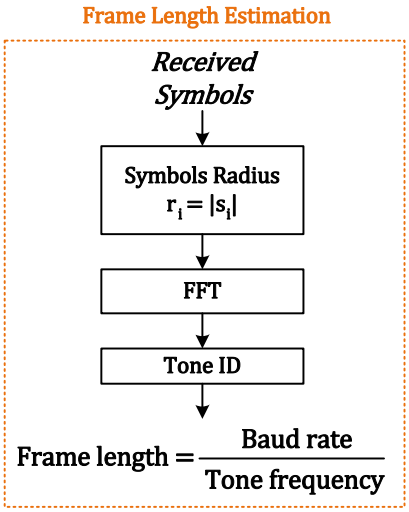

Fig. 4.22. Block diagram of the time-domain hybrid modulation format frame length estimation algorithm.

Figure 4.23 illustrates the frame length estimation process for experimental transmitted signal modulated with QPSK3-8QAM2, received in the back-to-back configuration with an OSNR of 32dB.

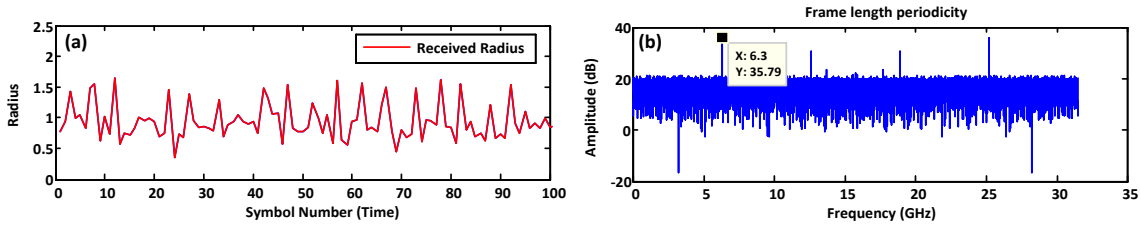

Fig. 4.23. Frame length estimation for a received QPSK3-8QAM2 signal in the back-to-back,
OSNR = 32dB: (a) Modulus of the received signal time-series; (b) Fast Fourier transform of the modulus of the received signal time-series.

Note that in deployed links, additional tones resulting from the data-link frames periodicity can be avoided by selecting appropriate block lengths (the data-link frame rate is much slower than the line rate whereas the TDHMF frame rate is only a fraction of the line rate).

Identification of the composing modulation formats and their ratio in the pattern

Recognizing a TDHMF involves identifying the pattern length (known at this point), the composing modulation formats, their ratio in the pattern, and the pattern arrangement in time.

Composing modulation formats and their ratio in the pattern are assessed by minimizing the mean square error between the received signal's symbol radius PDF and reference TDHMFs' symbol radius PDFs. The received signal's symbol radius PDF is assessed assuming that it follows a GMM, and by applying a machine learning algorithm (variational Bayesian expectation maximization for GMMs) [112] to identify the mean radius of each mixture composing the signal's symbol radius histogram. The knowledge of the pattern length significantly reduces the processing time by comparing the received

signal's symbol radius distribution with a reduced set of TDHMFs. TDHMFs' symbol radius distribution contains more information than homogeneous modulation format's, even after constellations normalization.

Figure 4.24 shows the received signal's symbol radius PDF estimation process using the variational Bayesian expectation maximization algorithm for GMMs. The illustrated signal is an experimental transmitted signal modulated with QPSK3-8QAM2, received in the back-to-back configuration with an OSNR of 32dB.

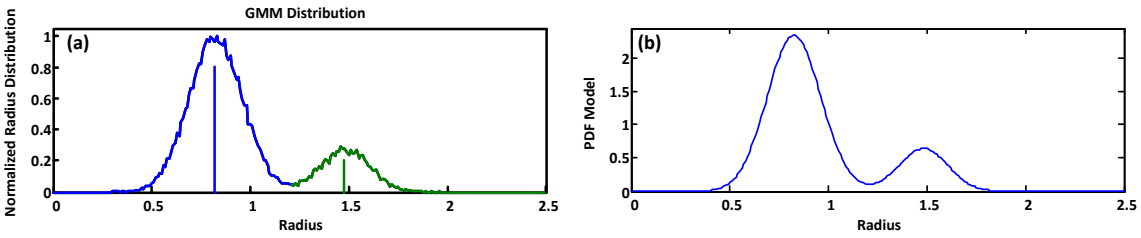

Fig. 4.24. Received symbols radius PDF estimation for a received QPSK3-8QAM2 signal in the back-to-back, OSNR = 32dB: (a) Gaussian mixtures identification associated to the received symbols radius histogram; (b) Corresponding PDF associated to the received symbols radius histogram.

Figure 4.25-4.27 shows the overlap of the estimated received signal's symbol radius PDF with theoretical symbol radius PDFs for different type of reference TDHMFs (BPSKp-QPSKq, QPSKp-8QAMq, 8QAMp-16QAMq). The estimated received signal's symbol radius PDF result from an experimental transmitted signal modulated with QPSK3-8QAM2, received in the back-to-back configuration with an OSNR of 32dB.

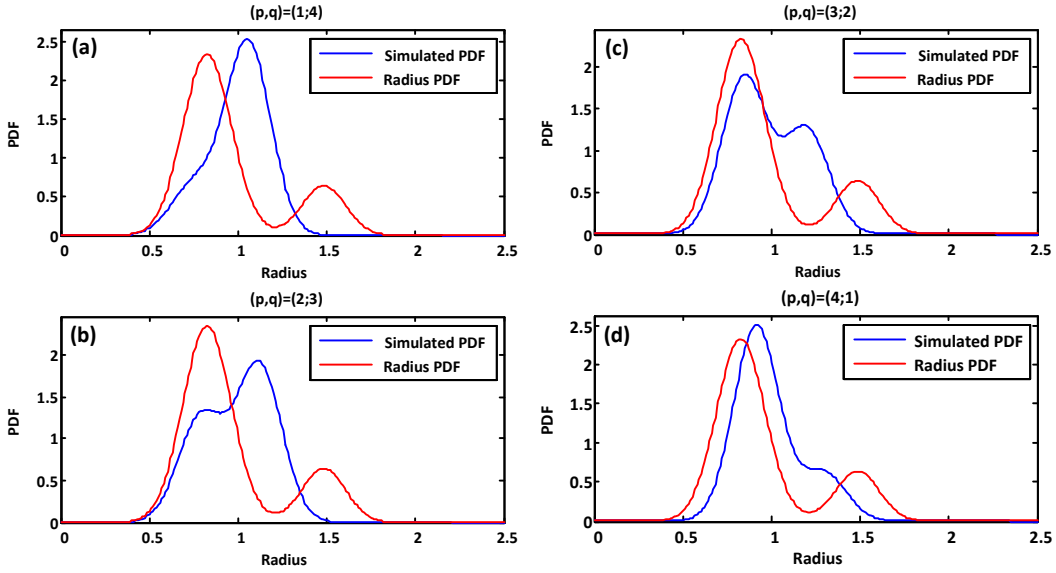

Fig. 4.25. In red, the estimated received symbols radius PDF for the received QPSK3-8QAM2 signal in the back-to-back, OSNR = 32dB. In blue, the theoretical symbols radius PDF for a BPSKp-QPSKq signal: (a) For (p,q) = (1,4); (b) For (p,q) = (2,3); (c) For (p,q) = (3,2); (d) For (p,q) = (4,1).

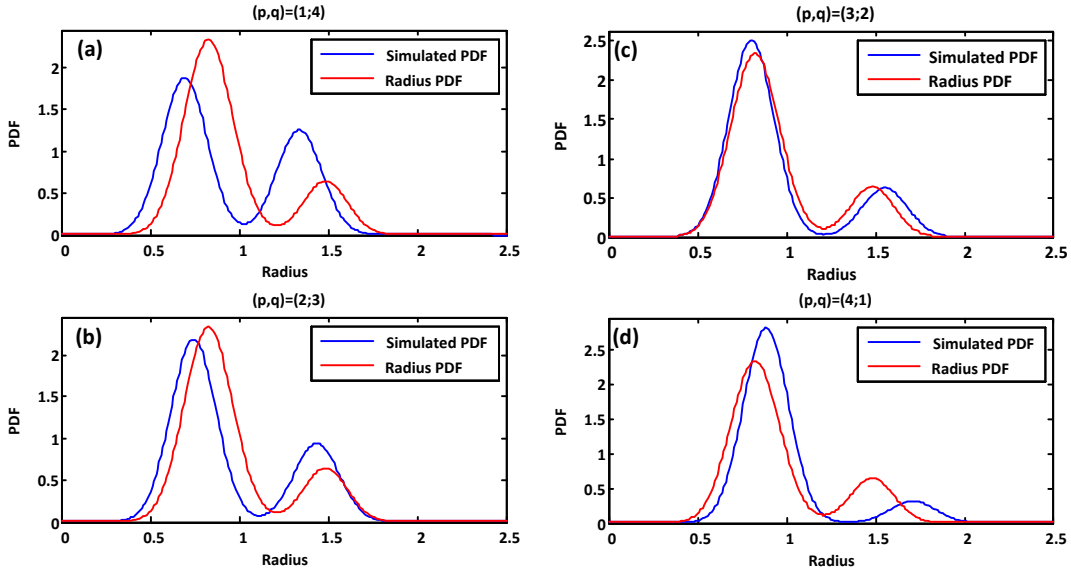

Fig. 4.26. In red, the estimated received symbols radius PDF for the received QPSK3-8QAM2 signal in the back-to-back, OSNR = 32dB. In blue, the theoretical symbols radius PDF for a QPSKp-8QAMq signal: (a) For (p,q) = (1,4); (b) For (p,q) = (2,3); (c) For (p,q) = (3,2); (d) For (p,q) = (4,1).

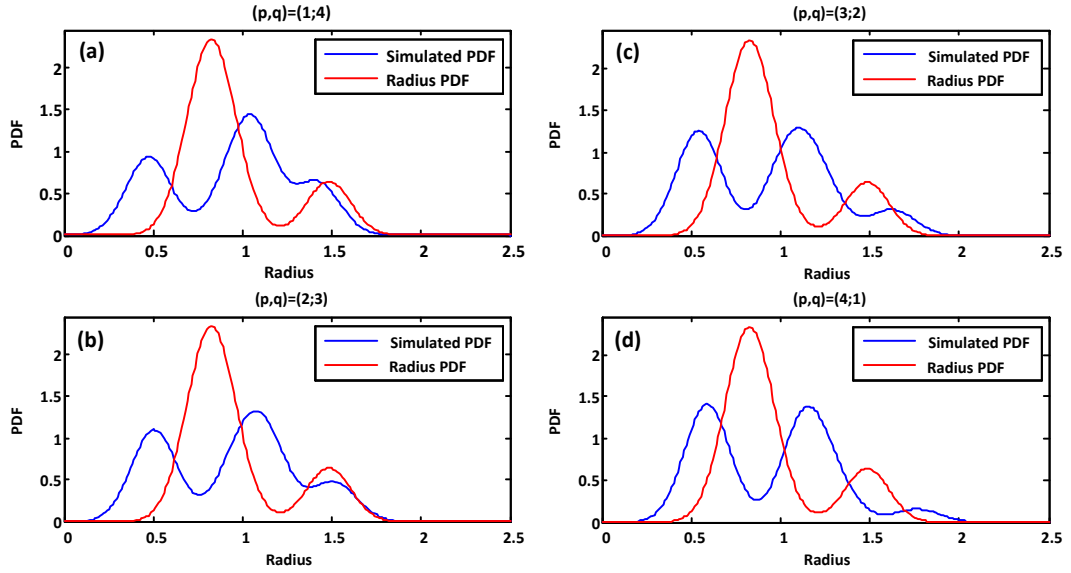

Fig. 4.27. In red, the estimated received symbols radius PDF for the received QPSK3-8QAM2 signal in the back-to-back, OSNR = 32dB. In blue, the theoretical symbols radius PDF for a 8QAMp-16QAMq signal: (a) For (p,q) = (1,4); (b) For (p,q) = (2,3); (c) For (p,q) = (3,2); (d) For (p,q) = (4,1).

Figure 4.28 illustrates the minimization process of the error criterion (total the mean square error) between the received signal's symbol radius PDF and reference TDHMFs' symbol radius PDFs. The received signal TDHMF is identified by the minimum total mean square error. The estimated received signal's symbol radius PDF result from an experimental transmitted signal modulated with QPSK3-8QAM2, received in the back-to-back configuration with an OSNR of 32dB.

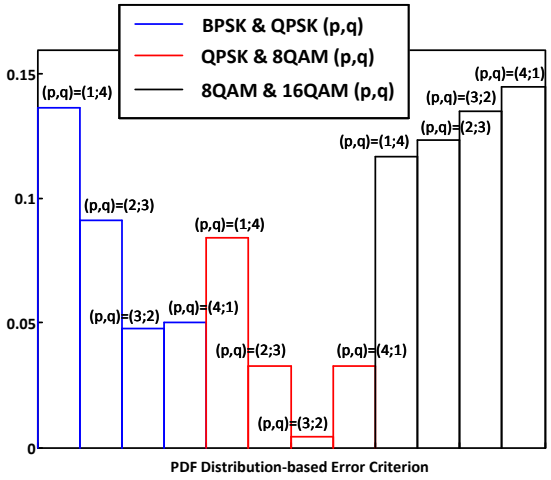

Fig. 4.28. Error criterion and identification of the composing modulation formats and their ratio in the pattern. Illustration with an experimental received QPSK3-8QAM2 signal in the back-to-back, OSNR = 32dB.

Time-domain hybrid modulation format pattern arrangement in time

Recognizing a TDHMF involves identifying the pattern length (known at this point), the composing modulation formats (known at this point), their ratio in the pattern (known at this point), and the pattern arrangement in time.

The pattern arrangement in time is identified using a HOS-based error criterion. Following the knowledge of the composing modulation formats ratio and the pattern length, all possible pattern arrangements in time are considered. Accordingly, for each case, subsets of the received signal's symbol time-series are extracted and their HOS are

compared to reference homogeneous modulation format's HOS. Minimization of the mean square error yields pattern arrangement in time.

Figure 4.29 summarizes the detailed steps of the proposed algorithm for time-domain hybrid modulation format recognition.

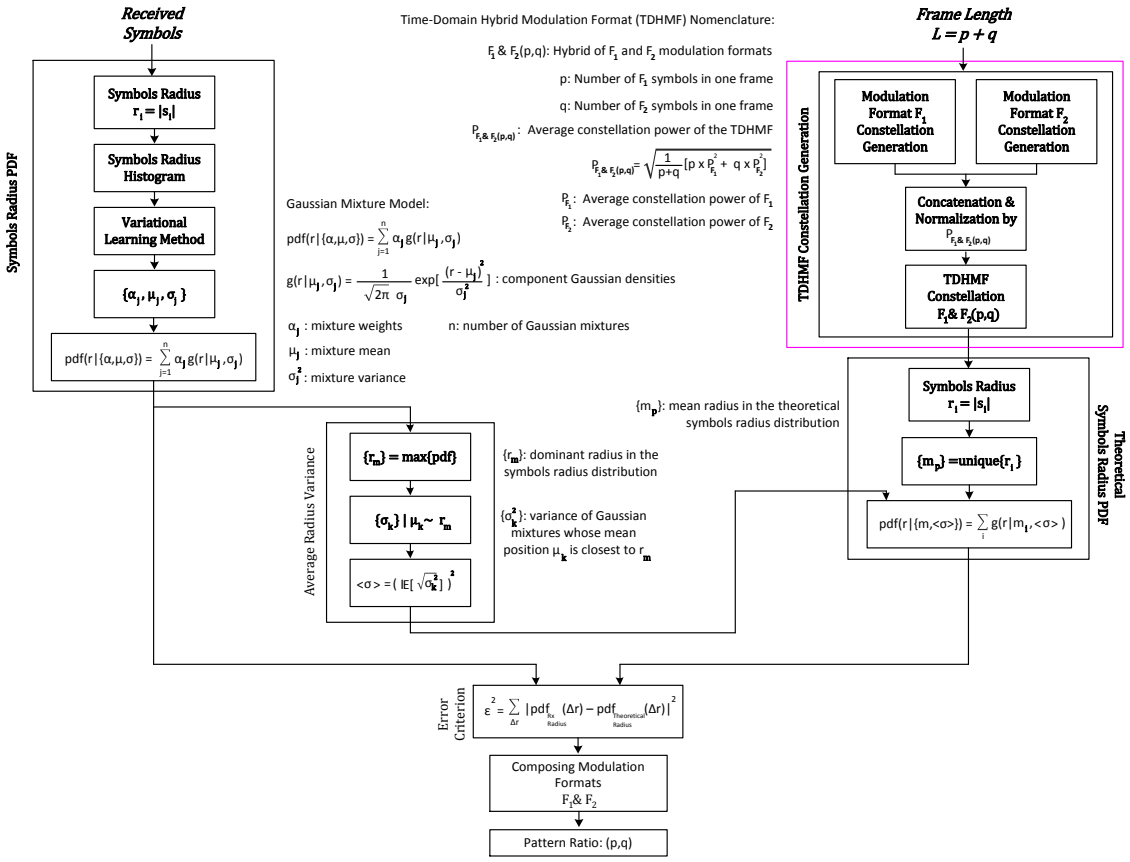

Fig. 4.29. Detailed block diagram of the proposed TDHMF recognition algorithm.

4.6 EXPERIMENTAL VALIDATIONS AND DISCUSSIONS

In this section, we examine the experimental performance of the proposed autonomous architectures for fiber optic communication links (Chapter 4- Section 3) and for photonic assisted wireless communication links (Chapter 4- Section 4). Specifically, we investigate the merits of: the autonomous architecture for fiber optic communication links performing HOS-based conventional MFR (Chapter 4 – Section 6.1), of the autonomous architecture for fiber optic communication links performing Stokes space-based conventional MFR (Chapter 4 – Section 6.2), of the autonomous architecture for fiber optic communication links performing time-domain hybrid modulation format recognition (Chapter 4 – Section 6.3), and of the autonomous architecture for photonic assisted wireless communication links performing Stokes space-based conventional MFR (Chapter 4 – Section 6.4).

4.6.1 AUTONOMOUS RECEIVER FOR FIBER OPTIC COMMUNICATION LINKS PERFORMING HIGHER ORDER STATISTICS-BASED CONVENTIONAL MODULATION FORMAT RECOGNITION

To validate the performance of the proposed autonomous receiver architecture for fiber optic communication links performing conventional MFR, Fig. 4.1, based on HOS, Fig. 4.14, we tested the algorithms using the experimental set-up of Fig. 4.30, which consists of a single-channel transmitter, an EDFA-based recirculating loop comprised of 88 km LAF spans, and a Picometrix coherent receiver with outputs digitized at 80 GS/s with 30 GHz bandwidth Agilent Infiniium DSA 93004L real-time oscilloscopes. The transmitter pulse pattern generator was configured for commonly used modulation formats, i.e. OOK, BPSK, QPSK and 16-QAM at 16 or 32 Gbaud. All signals were channelized for a 50 GHz grid using an optical filter with 46 GHz 3dB bandwidth. After polarization

multiplexing, the data is circulated four times through the loop for a total transmission of 1056 km. BER evaluation is quantified using Pseudo-Random Bit Sequences (PRBS-15).

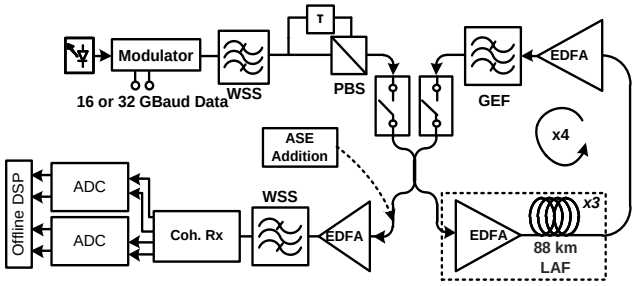

Fig. 4.30. Experimental network configuration consisting of an EDFA-based loop with three, 88 km LAF spans, and 80 GSa/s digitization.

The BER vs. OSNR performance of the experimental link was first evaluated with our conventional demodulation code (transmission parameters are known), in the back-to-back configuration, Fig. 4.31.a, and after 1056 km fiber transmission, Fig. 4.31.b. This assessment exhibits the demodulating capabilities of the fundamental demodulation methods (constrained by the link performance). Overall, the back-to-back results demonstrate excellent performance as the BER vs. OSNR curves approach the theoretical limit [115] for their respective constellations with a noticeable but reasonable implementation penalty. However, the implementation penalty for 16 GBaud-PDM-16QAM signals is greater than for 32 GBaud-PDM-16QAM signals. The X/Y polarization time-delay within the polarization multiplexer at the transmitter was likely not optimized for 16 GBaud-PDM-16QAM signals, causing additional DGD in the transmitted signal, and resulting in an additional penalty. The multi-span 1056 km fiber transmission reveals good performance with an added link implementation penalty.

The blind processing module evaluates the signal's transmission parameters and modulation format by examination of multiple data blocks. At a given OSNR, 15 discontinuous data blocks within the received signal were processed, each block comprising 40k symbols/polarization.

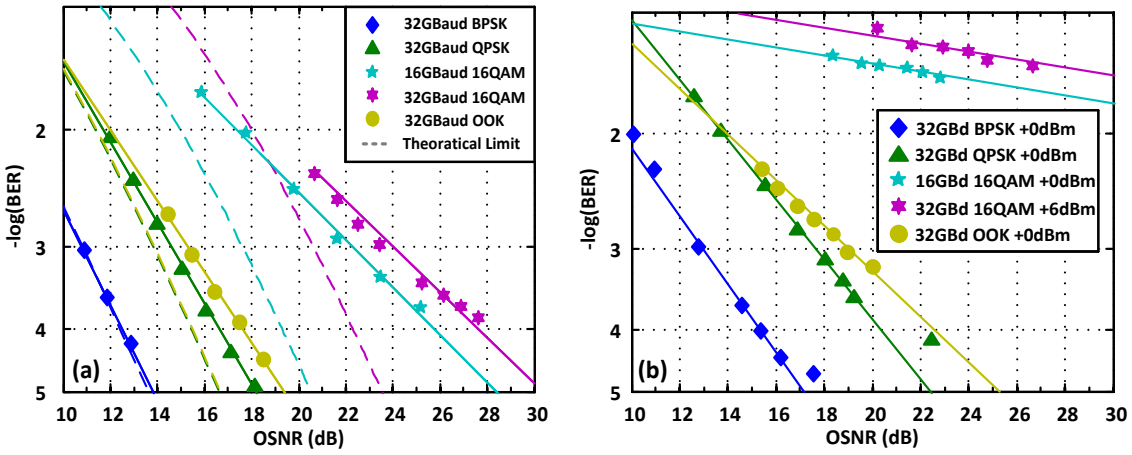

Fig. 4.31. BER vs. OSNR performance of the experimental link for various PDM-signals: (a) in the back-to-back configuration; (b) after 1056 km transmission in LAF at different launch powers.

To quantify the performance and the limits of the symbol rate estimation algorithm, we investigated the percentage of blocks with correct symbol rate identification vs. received OSNR, Fig. 4.32. While symbol rate identification is 100% successful in the back-to-back for the four modulation formats of interest over the considered range of OSNR, it

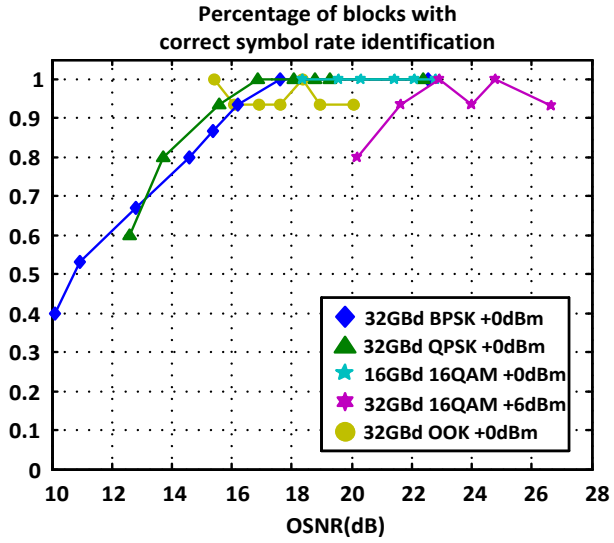

Fig. 4.32. Performance and limits of the symbol rate estimation algorithm after 1056 km transmission in LAF at different launch powers for various PDM-signals.

is sufficiently robust after 1056 km of fiber transmission. The algorithm fails for 32 GBaud-PDM-BPSK signals with an OSNR strictly lower than 11dB.

To quantify the efficacy of the blind processing module, we evaluated the robustness of correctly identifying the signal modulation format vs. OSNR which tests the identification of the entire set of signal parameters. We performed these tests for both back-to-back configuration, Fig. 4.33.a, and after transmission in 1056 km of LAF, Fig. 4.33.b, for each of the four modulation formats. The format classification performance of the architecture is very robust for both back-to-back and multi-span links, Fig. 4.33.a and 4.33.b. The probability of correctly identifying a single block of a waveform is nearly 100% for all reasonable OSNR. Thus, when choosing a likely format based on examination of multiple data blocks, the correct format is selected with near 100% accuracy for reasonable OSNR. Increasing the number of blocks examined will increase the confidence level. After 1056 km transmission in LAF, Fig. 4.33.b, high OSNR signals are recognized easily. We do note that identifying 32 Gbaud BPSK and QPSK signals for very low OSNR becomes challenging.

We also examined the behavior of the specific values of the HOS of interest vs. the received OSNR in the back-to-back, Fig. 4.33.c, and after 1056km fiber transmission Fig. 4.33.d. In the back-to-back configuration, Fig. 4.33.c, HOS for BPSK, QPSK and 16-QAM formats are quasi-insensitive to added ASE noise and their values are close to the expected theoretical fourth-order cumulants for noiseless and stationary constellations (cf. Table 4.1). Conversely, HOS for OOK are sensitive to the OSNR and their values tend to diverge from the theoretical expectation. This is mostly due to the required non-optimal choice of the blind polarization demultiplexing algorithms performed during the MFR process. After 1056 km fiber transmission, Fig. 4.33.d, we witness a higher dependence of HOS values to the added ASE noise for all formats of interest, although these values converge to the theoretical HOS values for higher OSNRs.

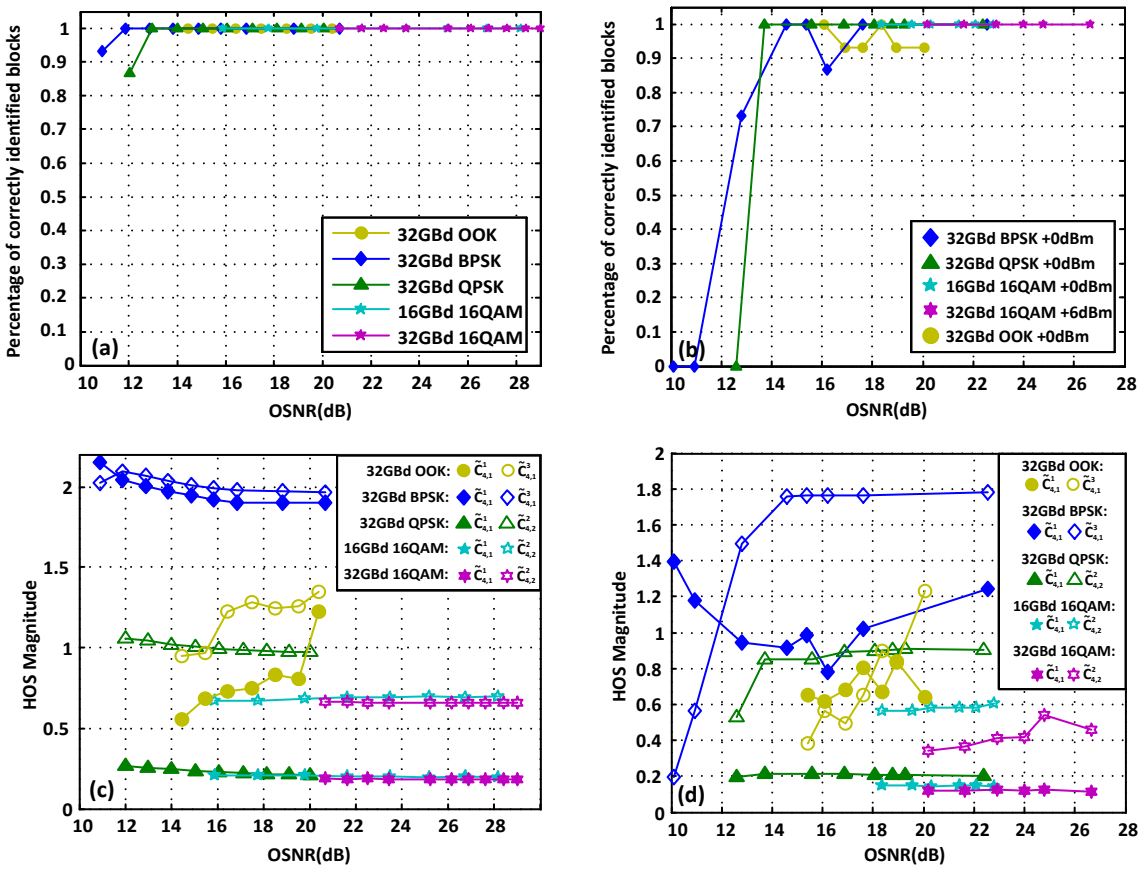

Fig. 4.33. Experimental classification performance vs. OSNR: When choosing a likely format based on examination of multiple blocks, the correct format is selected with 100% accuracy for both the (a) back-to-back configuration (b) and after 1056 km transmission in LAF. Experimental higher order statistics magnitude vs. OSNR: (c) in the back-to-back configuration; (d) after 1056 km transmission in LAF.

The proposed autonomous receiver architecture for fiber optic communication links performing conventional MFR based on HOS demonstrates excellent performance of identifying and subsequently decoding each modulation format at different symbol rates. Furthermore, the optimized processing steps ensure that there is almost no penalty compared to equivalent modulation standard single-format receivers. Therefore, for OSNR regimes with successful identification, the BER vs. OSNR performance of the autonomous

architecture overlaps with the standard performance of Fig. 4.31 obtained when the receiver is fully aware of the signal parameters.

As a conclusion, the proposed autonomous receiver architecture for fiber optic communication links performing conventional MFR based on HOS is able, with minimum knowledge about the transmitted signal, to identify and demodulate OOK, BPSK, QPSK and 16-QAM optimally. The architecture retrieves, in a blind fashion, transmission parameters such as the symbol rate, the accumulated CD, the number of multiplexed polarizations and the phase offset between the transmitting laser and the LO. Additionally, our blind demodulation code exhibits essentially the same performance as that of standard coherent demodulation algorithms for each modulation format.

4.6.2 AUTONOMOUS RECEIVER FOR FIBER OPTIC COMMUNICATION LINKS PERFORMING STOKES SPACE-BASED CONVENTIONAL MODULATION FORMAT RECOGNITION

To evaluate the performance of the proposed autonomous receiver architecture for fiber optic communication links performing conventional MFR, Fig. 4.1, based on our hybrid method combining Stokes space analysis with HOS, Fig. 4.16, we use our well calibrated 32 Gbaud fiber test bed with custom conventional demodulation algorithms. We first assessed the demodulating capabilities (constrained by the link performance) of the fundamental (non-blind) demodulation methods by evaluating the BER vs. OSNR performance of the experimental link. We then quantified the classification performance of the proposed Stokes space-based MFR method by investigating the percentage of correctly identified waveforms vs. OSNR.

The experimental test bed, Fig. 4.34, is composed of a single-channel optical baseband transmitter, a fiber optic link consisting of an EDFA-based recirculating loop comprised of three 90 km LAF spans, and an intradyne coherent optical receiver with outputs digitized at 80GSa/s by synchronized 30 GHz bandwidth real-time ADCs.

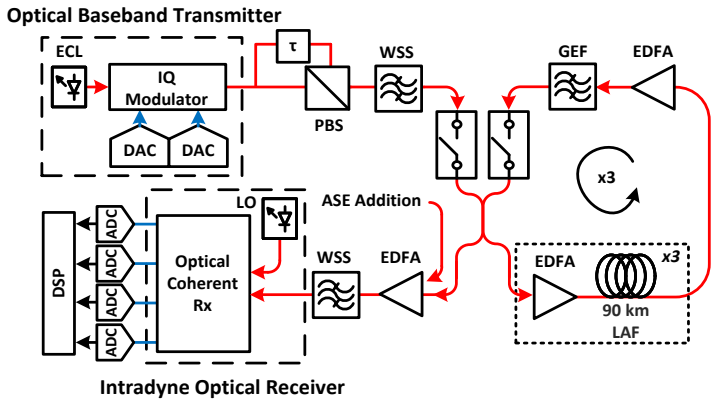

Fig. 4.34. Fiber optic communication link experimental configuration consisting of an EDFA-based loop with three, 88 km LAF spans, and 80 GSa/s digitization.

The transmitter generates a 31.5 Gbaud single-carrier signal centered at 1550.92nm using a LN-IQ modulator with either OOK/ BPSK/ QPSK/ 16QAM. A pulse pattern generator is used to create the OOK and BPSK signals, whereas a 63GSa/s high-speed DAC is used to generate the QPSK and 16-QAM signals with a RRC-0.01-roll-off pulse shape. For DAC-generated signals, our previously described transmitter-based pre-equalization scheme [114], wherein the tap weights are determined by the receiver-side LMS equalization algorithm, is used to compensate for the band-limitations and other linear imperfections of the overall channel.

All optical signals were channelized for a 50 GHz grid, using a reconfigurable optical filter with 46 GHz 3 dB bandwidth, and polarization multiplexed before transmission. After polarization multiplexing, the data is circulated three times through the loop for a total transmission of 810 km. ASE is added to the optical signal prior detection to control the received OSNR. BER is quantified using PRBS-15.

Signal OSNRs were measured at the input of the coherent optical receiver. For the 810 km LAF transmission experiment, launch powers were chosen close to the optimum launch power for each modulation format (minimum of the BER vs. launch power curve).

At a given OSNR, both in the back-to-back configuration and after 810 km transmission in LAF, the demodulation performance (quantified by the BER), Fig. 4.35, and the classification performance (quantified by the percentage of correctly identified waveforms), Fig. 4.36, were examined over 15 discontinuous data captures, each containing 100,000 samples/polarization (40,000 symbols/polarization).

The demodulation performance of the optical communication link is excellent in the back-to-back configuration, Fig. 4.35.a, as the BER vs. OSNR curves approach the theoretical limit (dashed lines) [115] for 31.5 Gbaud-PDM-OOK, BPSK, and QPSK signals with a small implementation penalty. However, the implementation penalty for 31.5 Gbaud-PDM-16QAM signals is greater, and a BER floor is reached for very high OSNRs, which we attribute to hardware limitations. The multi-span 810 km LAF transmission, Fig. 4.35.b, exhibits good performance with an added link implementation penalty.

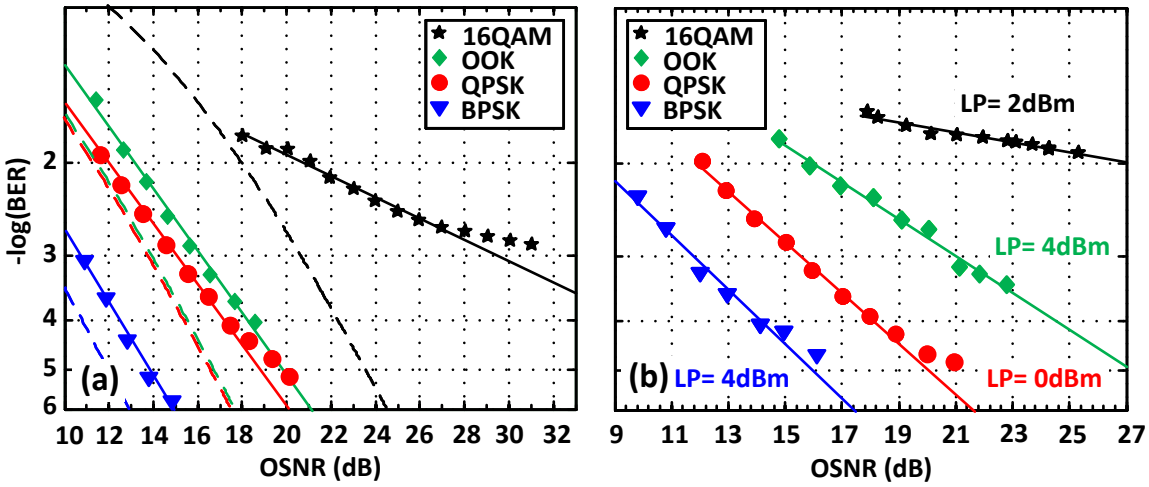

Fig. 4.35. Demodulation performance of the optical communication link for 31.5 Gbaud-PDM-signals: (a) in the back-to-back configuration; (b) after 810 km transmission in LAF at different launch powers.

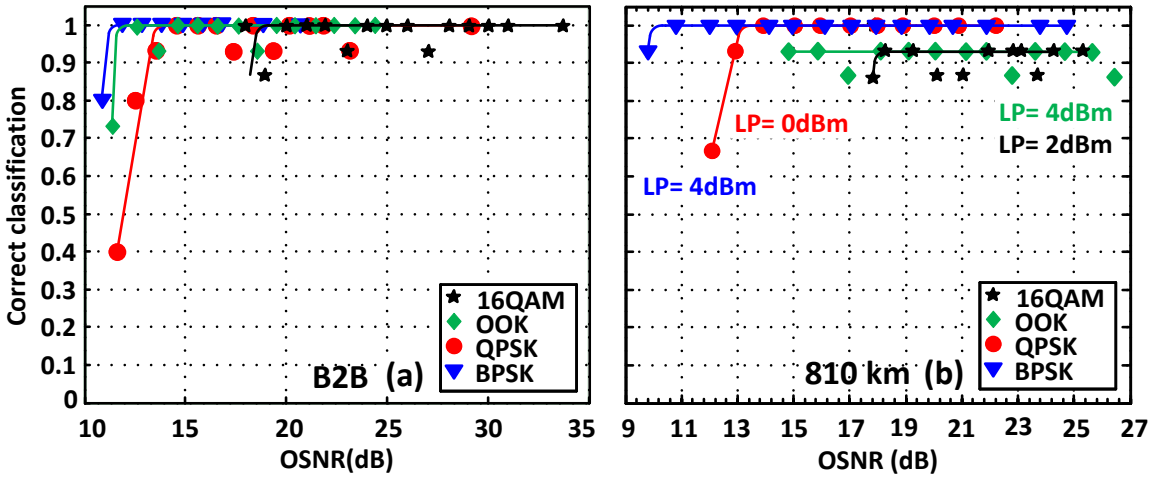

Fig. 4.36. Classification performance of the proposed Stokes space-based MFR method for 31.5 Gbaud-PDM-signals: (a) in the back-to-back configuration; (b) after 810 km transmission in LAF at different launch powers.

The classification performance for all the modulation formats studied (OOK, BPSK, QPSK, 16QAM) is exceedingly robust in the back-to-back configuration, Fig. 4.36.a, and after 810 km transmission in LAF, Fig. 4.36.b. The Stokes space-based MFR method yields the correct format with very high confidence for reasonable OSNRs. Indeed, the percentage of correctly identified waveforms is nearly 100% for OSNRs greater or equal to the OSNR required to achieve a 10^{-2} BER. Increasing the number of waveforms examined will increase the confidence level. We note that after 810 km transmission, the percentage of correctly identified waveforms for OOK or 16QAM signals does not approach 100%, Fig. 4.36.b, most likely due to a combination of residual CD, DGD, PDL, and nonlinearities.

We further examine, Figs. 4.37 and 4.38, the decision metrics used in the MFR process (coefficients d, magnitudes of normalized weighted estimates $\tilde{C}_{4,i}$ of fourth-order cumulants, and spatial cross-correlation indices) vs. OSNR.

Fig. 4.39 represents the decision tree describing the process; the first decision separating the {M-QAM} formats from {OOK + M-PSK + M-PAM} was described previously. Figs. 4.37.a, b, c, and 4.38.a depict the decision metrics for the four modulation

formats in the back-to-back configuration, and Figs. 4.37.d, e, f, and 4.38.b depicts the same metrics after 810 km transmission in LAF. Specifically, Fig. 4.37.a (4.37.d) illustrates the average coefficient d vs. OSNR in the back-to-back (after transmission). The 2-dimensional Stokes space constellation coefficient d clearly lies below the displayed threshold, with an increased reliability for higher OSNR regimes. Fig. 4.37.b (4.37.e) shows the magnitudes of normalized weighted estimate $\tilde{C}_{4,1}$ vs. OSNR in the back-to-back (after transmission) used to distinguish BPSK from {OOK+QPSK}. Experimental

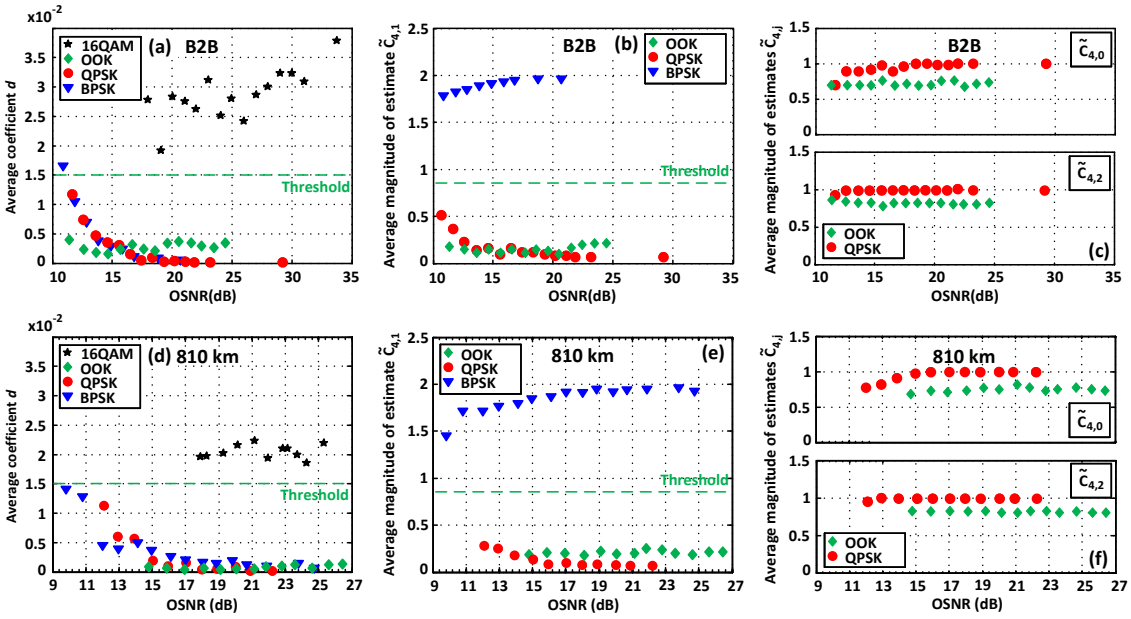

Fig. 4.37. (a) Average coefficient d vs. OSNR; (b) average magnitude of the normalized weighted estimate $\tilde{C}_{4,1}$ vs. OSNR; (c) average magnitude of the normalized weighted estimates $\tilde{C}_{4,i}$ vs. OSNR (i=0 or 2) for 31.5 Gbaud-PDM-signals in the back-to-back configuration. (d) Average coefficient d vs. OSNR; (e) average magnitude of the normalized weighted estimates $\tilde{C}_{4,i}$ vs. OSNR (i=0 or 2); (f) average magnitude of the normalized weighted estimate $\tilde{C}_{4,1}$ vs. OSNR for 31.5 Gbaud-PDM-signals after 810 km transmission in LAF.

measurements for BPSK lie in a non-ambiguous fashion above the displayed threshold. Fig. 4.37.c (4.37.f) exhibits the magnitudes of normalized weighted estimates $\tilde{C}_{4,i}$ vs. OSNR

(i=0 or 2) in the back-to-back (after transmission) used to distinguish OOK from QPSK. Experimental measurements converge closely to theoretical values calculated for ideal noiseless constellations (Table 4.3). Finally, Fig. 4.38.a (4.38.b) shows the spatial cross-correlation index Γ_{XY} vs. OSNR for 16QAM in the back-to-back (after transmission). The minimization process robustly results in the identification of 16QAM formats across the range of investigated OSNR.

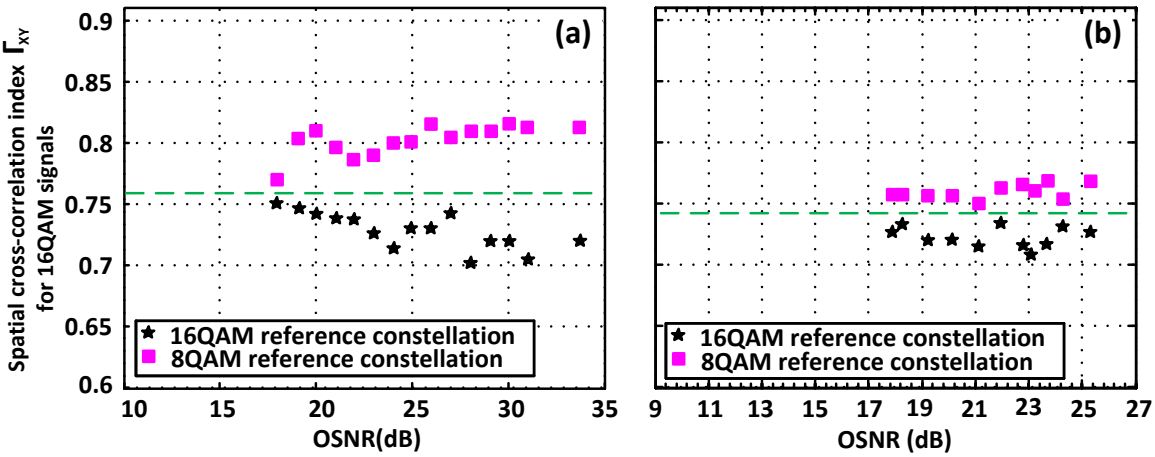

Fig. 4.38. Average spatial cross-correlation index calculated for 31.5 Gbaud 16QAM signals vs. OSNR: (a) in the back-to-back configuration; (b) after 810 km transmission in LAF at different launch powers.

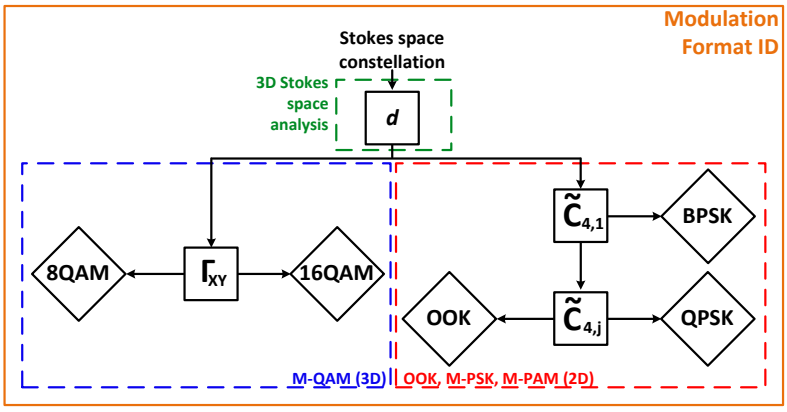

Fig. 4.39. Decision metrics used in the proposed Stokes space-based modulation format recognition method.

As a conclusion, the proposed autonomous receiver architecture for fiber optic communication links performing conventional MFR based on our hybrid method combining Stokes space analysis with HOS is able, with minimum knowledge about the transmitted signal, to identify and demodulate M-PSK, M-PAM, M-QAM, and legacy formats.

Via experiment, we demonstrated robust identification of a variety of signal formats over a wide range of received OSNR including OOK, BPSK, QPSK, and 16QAM. The advantages of the proposed algorithm include: the capacity to autonomously identify single and dual polarization formats, a resistance to low-OSNR conditions inherent to HOS, and an immunity to the received SOP variations. Furthermore the Stokes space method is inherently insensitive to residual carrier-LO frequency and phase offsets.

The proposed algorithm does not require training, and is performed relatively early in the receiver DSP architecture. It is envisioned that the format recognition is only required at start up or when there is a loss of coordination between transmitter and receiver.

4.6.3 AUTONOMOUS RECEIVER FOR FIBER OPTIC COMMUNICATION LINKS PERFORMING TIME-DOMAIN HYBRID MODULATION FORMAT RECOGNITION

To evaluate the performance of the proposed autonomous receiver architecture for fiber optic communication links performing time-domain hybrid modulation format recognition, Fig. 4.7, based on the statistical distribution of the received signal's radius, Fig. 4.21, we constructed an experimental network, Fig. 4.40. The experimental setup consists of a single-channel dual-polarization system transported at 1550.92 nm with 50 GHz optical filters at the transmitter and receiver, an EDFA-based recirculating loop comprising three 90 km LAF spans, a coherent optical receiver and two synchronized ADCs sampling at 80GSa/s. A 64GSa/s high-speed DAC was used to generate 31.5 GBaud electrical TDHMF signals driving an I/Q modulator. A pre-

equalization scheme based on the tap weights determined by the receiver-side LMS equalization algorithm was used to compensate for the band-limitations and other imperfections of the channel [114]. Signals were acquired in the back-to-back and after 3 loops (total distance of 810km) for 7 different TDHMFs composed with BPSK, QPSK, 8QAM & 16QAM. At a given OSNR, the probability of recognition of a format was quantified over 15 waveforms (130,000samples/ polarization/ waveform).

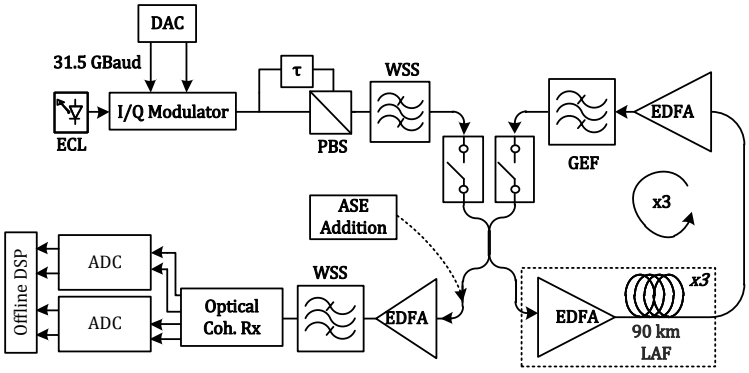

Fig. 4.40. Fiber optic communication link experimental configuration consisting of an EDFA-based loop with three, 88 km LAF spans, and 80 GSa/s digitization.

The BER vs. OSNR performance of the architecture was evaluated with full knowledge of the received signal's transmission parameters, before transmission (back-to-back configuration), Fig. 4.41.a, and after transmission in the loop, Fig. 4.41.b.

The introduced frame length estimation algorithm very rarely fails both in the back-to-back and after transmission. Therefore the spectral analysis of the received radius time-series is a good method to detect TDHMFs.

The classification success of the proposed MFR method for TDHMFs is shown in Fig. 4.42. The proposed TDHMF recognition method demonstrates excellent classification performance in the back-to-back, Fig. 4.42.a, and after 810km transmission, Fig. 4.42.b. Indeed, for BER below the FEC threshold, the probability of correct recognition reaches 1. However, identifying QPSK1-8QAM1 is challenging after fiber transmission. Indeed, at

lower OSNR, the high symbol radius variance contributes to a misestimation with 8QAM1-16QAM1. Nevertheless, reliable recognition is achieved at high OSNR.

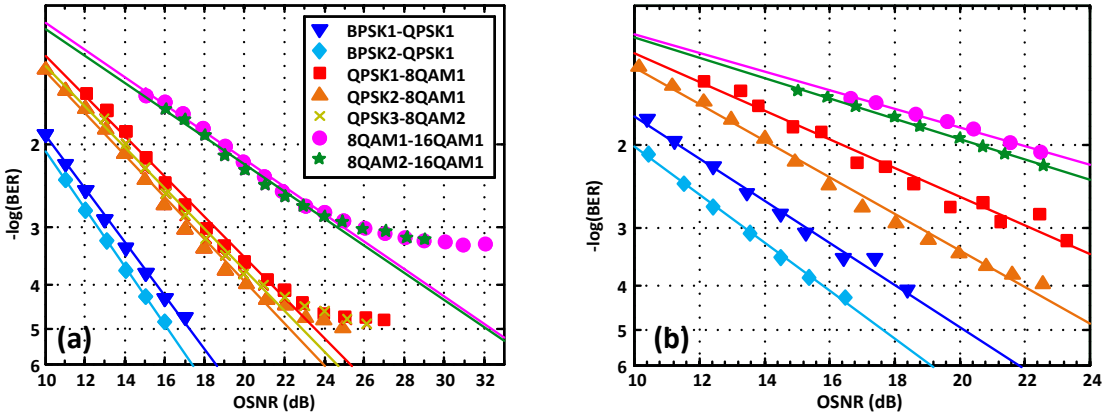

Fig. 4.41. Experimental BER vs. OSNR performance for various 31.5Gbaud time-domain hybrid modulation format (TDHMF) signals after blind reception, symbol rate estimation, format identification, and optimized processing: (a) in the back-to-back configuration; (b) after transmission in 810 km in LAF (0dBm launch power).

As a conclusion, the proposed autonomous receiver architecture for fiber optic communication links performing time-domain hybrid modulation format recognition based on the statistical distribution of the received signal's radius is able, with minimum knowledge about the transmitted signal, to identify and demodulate TDHMFs.

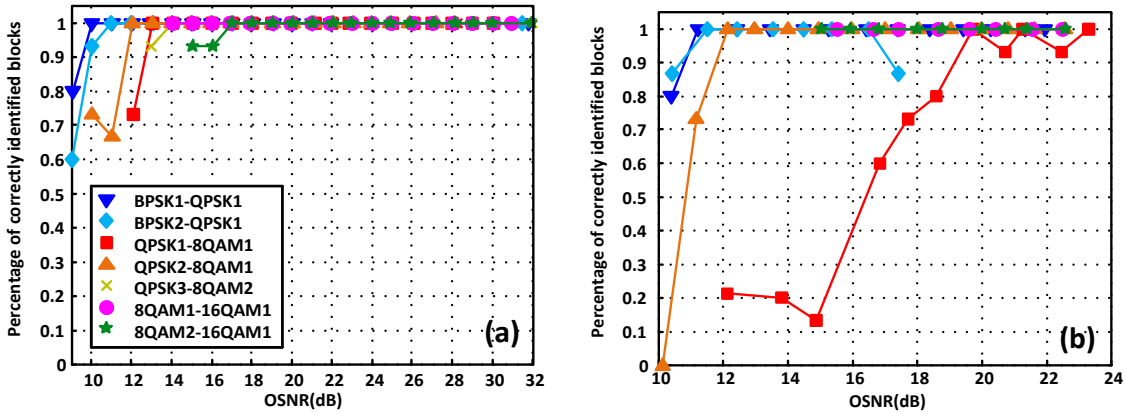

Fig. 4.42. Experimental classification performance for various 31.5Gbaud TDHMF signals: (a) in the back-to-back configuration; (b) after transmission in 810 km in LAF (0dBm launch power).

Via experiment, we demonstrated robust identification, over a wide range of received OSNR, of a variety of TDHMFs composed with BPSK, QPSK, 8QAM and 16QAM.

The proposed time-domain hybrid modulation format recognition method, is robust to very low-OSNR conditions. The architecture has mostly excellent classification performance with signal OSNRs greater or equal to the OSNR required to achieve a 10-2 BER.

4.6.4 AUTONOMOUS RECEIVER FOR PHOTONIC ASSISTED WIRELESS COMMUNICATION LINKS PERFORMING STOKES SPACE-BASED CONVENTIONAL MODULATION FORMAT RECOGNITION

To evaluate the performance of the proposed autonomous receiver architecture for photonic assisted wireless communication links performing conventional MFR, Fig. 4.7, based on our hybrid method combining Stokes space analysis with HOS, Fig. 4.16, we designed an experimental optical-wireless network. The experimental setup, Fig. 4.43, consists of a single-polarization optical baseband transmitter, an optical heterodyne up-converter, a V-band wireless link, and a heterodyne V-band receiver.

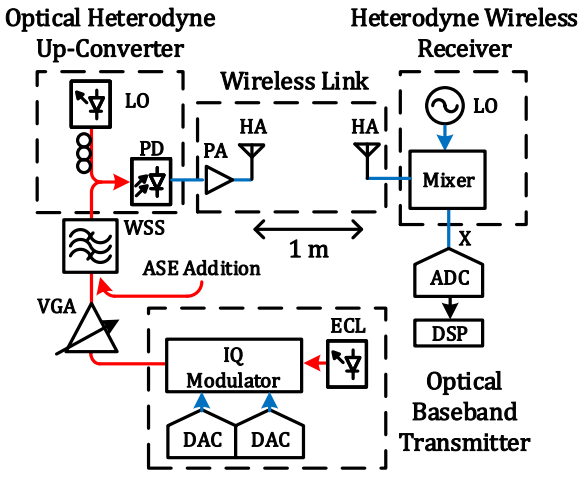

Fig. 4.43. Photonic assisted wireless communication link experimental configuration.

The single-polarization optical baseband transmitter, comprised of a 64 GSa/s high-speed DAC and a linear LN-IQ modulator, generates a single-polarization single-carrier signal at 1550.92 nm and modulated at 3.2 Gbaud with either BPSK/ QPSK/ 8QAM/ 16QAM with a RRC-0.05-roll-off pulse shape. A pre-equalization scheme, similar to the method presented by Pan et al. [114], and based on the tap weights determined by the receiver-side LMS equalization algorithm, was used to compensate for the band-limitations (low-pass and pass-band) and other linear imperfections of the overall optical-wireless channel. After modulation, ASE is added to the optical signal and filtered in a 50GHz optical filter to reduce out-of-band noise. The optical heterodyne up-converter includes a C-band high-speed photodiode with a bandwidth greater than 50 GHz, and an optical LO with a 52.8 GHz frequency offset compared to the optical signal carrier frequency. The V-band wireless link contains a high power amplifier (PA) with a 16 GHz bandwidth centered at 58 GHz, and two 24 dBi V-band horn antennas (HA) for wireless transmission and reception, separated by 1 m. Finally, the heterodyne V-band receiver includes a 50GHz-RF LO, and a V-band mixer. Down-converted IF signals are sampled at 40 GSa/s with a 16 GHz bandwidth real-time ADC.

We quantified the classification performance of the architecture by investigating the percentage of correctly identified (processing) blocks vs. OSNR, Fig. 4.44. BER vs. OSNR performances are shown as insets. Controlling the optical signal OSNR enables modifying the received RF signal SNR.

Signal OSNRs were measured at the input of the photodiode. The input optical power of the optical heterodyne up-converter was selected to operate in the linear regime of the photodiode and kept constant throughout the measurements to maintain a received RF power of ~10 dBm at the mixer input. At a given OSNR, the percentage of correctly identified blocks was determined by examining 10 waveforms (200,000 samples each or 16,000 symbols).

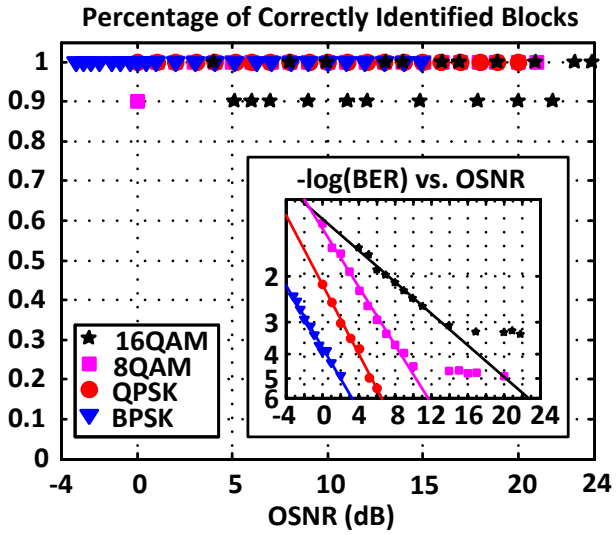

Fig. 4.44. Experimental classification performance vs. OSNR for 3.2 Gbaud photonic assisted RF signals transported over 1 m in the V-band.

We also illustrated, Fig. 4.45, the decision metrics used in the MFR process. Fig. 4.45.a illustrates the average value of the coefficient c vs. the OSNR for the four modulation formats of interest. 2-dimensionnal Stokes space constellations coefficient c lie below the displayed threshold. Fig. 4.45.b exhibits the normalized weighted fourth order cumulant C4,1 vs. OSNR used to distinguish BPSK from QPSK. Fig. 4.45.c (4.45.d) shows the spatial cross-correlation index vs. OSNR for 8QAM (16QAM) signals.

The classification performance of the proposed architecture, Fig. 4.45, is excellent as blocks are accurately identified with a success ratio greater than 90% across the range of OSNR investigated for all the modulation formats of interest (BPSK, QPSK, 8QAM, 16QAM). The reliability of the algorithm is even met in very low-OSNR regimes (for BER above the 10^{-2} FEC threshold), as modulation format can be properly identified despite the high amount of noise.

As a conclusion, the proposed autonomous receiver architecture for photonic assisted wireless communication links performing conventional MFR based on our hybrid method combining Stokes space analysis with HOS is able, with minimum knowledge

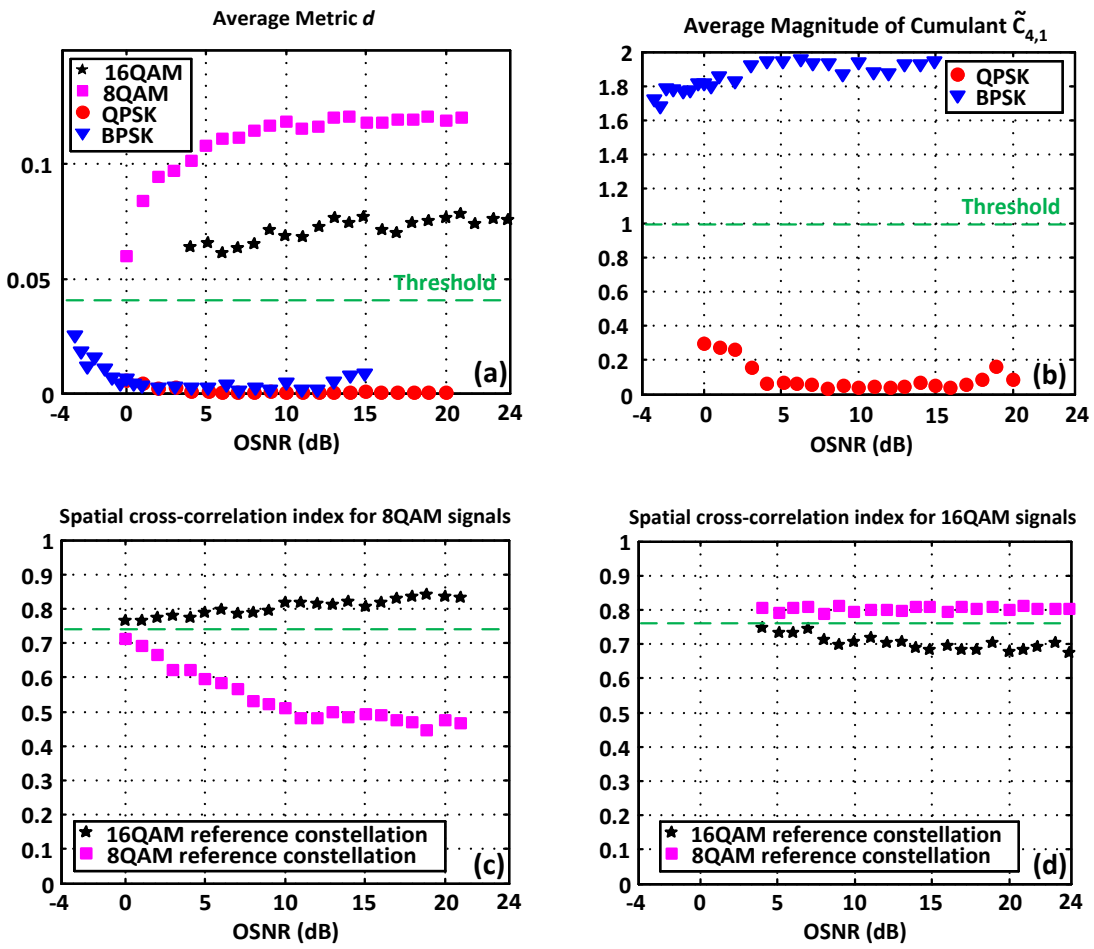

Fig. 4.45. Decision metrics used for MFR: (a) discriminating M-PSK from M-QAM: average statistic d vs. OSNR used to estimate the dimension of the Stokes space constellation; (b) discriminating BPSK from QPSK: average magnitude of the normalized weighted fourth order cumulant $C_{4,1}$ vs. OSNR; (c) ddiscriminating 8QAM from 16QAM: spatial cross-correlation index calculated for 3.2Gbaud 8QAM signals vs. OSNR; (d) discriminating 8QAM from 16QAM: spatial cross-correlation index calculated for 3.2Gbaud 16QAM signals vs. OSNR.

about the transmitted signal, to identify and demodulate M-PSK, M-PAM, and M-QAM wireless signals generated with a high-speed optical transmitter.

Via experiment, we demonstrated robust identification of a variety of multi-gigabit wireless signal formats over a wide range of received OSNR including BPSK, QPSK, 8QAM and 16QAM. The advantages of the proposed algorithm include: the capacity to autonomously identify single and dual polarization formats, a resistance to low-OSNR

conditions inherent to HOS, and an immunity to the received SOP variations. Furthermore the Stokes space method is inherently insensitive to residual carrier-LO frequency and phase offsets.

The architecture has excellent classification performance with a success ratio greater than 90% across the range of OSNR investigated for all the modulation formats of interest.

We acknowledge other fundamental limiting parameters to the architecture classification performance such as the transmitter bandwidth and DAC ENoB, the received SNR, or the ADC bandwidth and ENoB. In general, any parameter limiting the optical-wireless transmission link performance will impact the architecture classification performance. Increasing the wireless transmission distance can be attained with higher output power photodiodes, and the utilization of a RF low-noise amplifier (LNA) at the receiver-end at the cost of linearity degradations.

On top of the architecture performance, we demonstrated the scalability of our proposed conventional MFR method combining Stokes space analysis with HOS to optical signals and multi-gigabit photonic assisted wireless signals.

CHAPTER 5

BLIND SIGNAL RECONSTRUCTION

5.1 CONCEPT OF SIGNAL RECONSTRUCTION

In Chapter 4, we introduced autonomous receivers that can operate fully autonomously to identify and demodulate, without prior knowledge, any received signal. These architectures rely on advanced DSP techniques to blindly identify parameters necessary to proceed to the received signal demodulation. We investigated in details blind parameters estimation algorithms for link impairments parameters and for the received signal parameters, including the modulation format.

Autonomous receivers unlock access to link impairments parameters and signal parameters, providing the support required to recreate the detected signal with high-fidelity. Digital analog-to-converter (DAC)-based transmitter architectures designed for signal reconstruction can leverage the parameters identified by autonomous receivers to reconstruct and retransmit a replica of the received signal such that it is indiscernible from the original.

The concept of blind signal reconstruction consists in DAC-based transmitter architectures that are capable of constructing or reconstructing any signal, for a wide range of signal parameters and link impairments parameters.

5.2 MOTIVATION AND APPLICATIONS

DAC-based transmitter architectures capable of generating any signal for transmission are an ideal technology for testing communication links and particularly receivers' performance. By finely controlling the DAC-generated signal parameters (such as the pulse shape, the symbol rate, the number of multiplexed polarizations, and the modulation format) and the link impairments parameters embedded in the DAC-generated signal (impairments resulting from the transmitter, the transmission link, or the receiver),

the communication link characteristics can be evaluated, such as the bandwidth of concatenated link components, the receiver performance to fiber optic impairments, or the network dynamic spectrum management capabilities.

In other applications, when associated with autonomous receivers, DAC-based architectures designed for signal reconstruction are ideal candidates for regenerators. Being independent from the supervisory control plane, these architectures can autonomously reconstruct a replica of the received signal, with the same signal parameters, after having neutralized the penalties incurred by transmission link impairments (regeneration).

Finally, in some applications, there are needs to recreate an identical copy of the received signal with high-fidelity. DAC-based architectures designed for signal reconstruction coupled with autonomous architecture can reconstruct and retransmit a replica of the received signal such that it is indiscernible from the original.

5.3 ARCHITECTURES FOR FIBER OPTIC COMMUNICATION LINKS

The set of parameters required to reconstruct a received signal with high fidelity can be divided in two sub-sets: signal parameters and link impairments parameters.

Signal parameters are comprised of: the signal pulse shape, the symbol rate, the number of multiplexed polarizations, and the modulation format.

Link impairments parameters can result from the transmitter, the fiber optics transmission link, or the coherent optical receiver. Link impairments parameters resulting from the transmitter are comprised of: modulators' I/Q imbalance, timing jitter, and band limitations. Link impairments parameters resulting from the fiber optic transmission link are comprised of: CD, change in SOP, PMD, PDL, ICI, ASE noise, band limitations, and Kerr-induced nonlinear effects such as SPM, XPM, and FWM. Link impairments parameters resulting from the coherent optical receiver are comprised of: transmitter laser-LO frequency offset and phase noise contribution, ADC's sampling clock timing error and jitter, band limitations, and shot noise.

We designed an autonomous receiver-assisted DAC-based architecture for signal generation, Fig. 5.1, that constructs or reconstructs any signal, for a wide range of signal parameters and link impairments parameters.

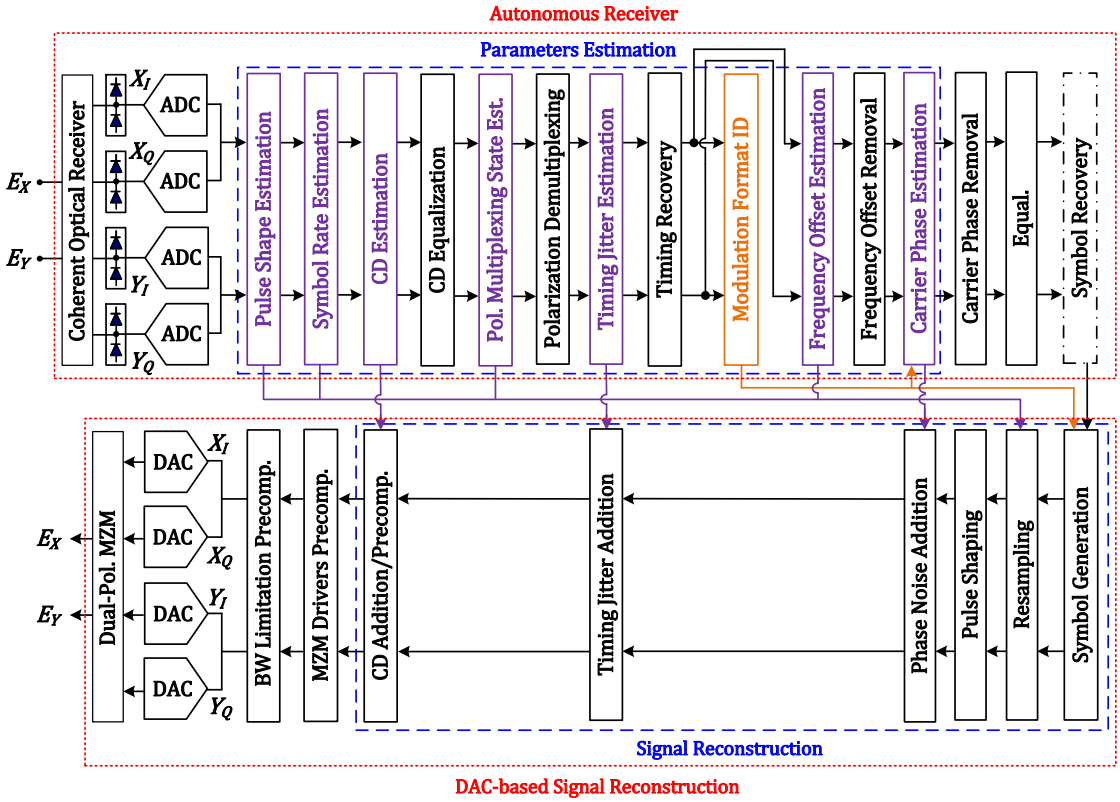

Fig. 5.1. Autonomous receiver-assisted DAC-based architecture for signal reconstruction. The autonomous receiver (upper architecture) estimates the signal parameters and link impairments parameters required to reconstruct the received signal with high-fidelity.

Reconstruction of a received signal can be organized in two steps. First, knowledge of the desired signal parameters and link impairments parameters are acquired. Particularly, these are blindly estimated by the assisting autonomous receiver (but, the parameters can also be communicated by the supervisory control layer in some situations). Second, the received signal is reconstructed.

In our work, we investigate the estimation of signal parameters (Chapter 5 – Section 3.1) and a sub-set of the link impairments parameters mentioned above. Specifically, we

focused on: CD, and timing jitter (Chapter 5 – Section 3.2). We also investigated the addition of the associated link impairments to the DAC-generated signal (Chapter 5 – Section 3.2).

5.3.1 SIGNAL PARAMETERS ESTIMATION

Signal Pulse Shape Estimation

Lopez-Salcedo et al. introduced an iterative frequency domain method based on the second-order cyclostationary property of the received signal to estimate the pulse shape for linear modulations [116]. Although we have not investigated the direct application of this method to received broadband optical signals, we believe a similar cost function inspired from this work can be developed for the purpose of blind identification of pulse shapes for broadband optical signals modulated with conventional modulation formats.

Symbol Rate Estimation

We investigated how to blindly estimate the received signal's symbol rate in Chapter 4 - Section 5.2

Number of Multiplexed Polarizations Estimation

We investigated how to blindly estimate the received signal's number of multiplexed polarizations in Chapter 4 - Section 5.2

Modulation Format Recognition

We examined how to blindly identify the modulation format of the incoming signal in Chapter 4 – Section 5.3. Particularly, for fiber optic communication links, we investigated conventional MFR and time-domain hybrid modulation format recognition algorithms.

5.3.2 LINK IMPAIRMENTS PARAMETERS ESTIMATION AND ADDITION

Total Accumulated Chromatic Dispersion

Total Accumulated Chromatic Dispersion Estimation

We investigated how to blindly estimate the total accumulated CD in Chapter 4 – Section 5.1.

Total Accumulated Chromatic Dispersion Addition

We have seen in Chapter 2 - Section 5 that CD can be digitally mitigated by filtering the received signal in the time or frequency domain with a linear filter. Specifically, the CD frequency domain transfer function can be modeled as [36]:

$$H_{CD}(f) = \exp(-i\frac{\pi cDL}{(f_c-f)^2}f^2)$$

Where L is the fiber length, and D is the fiber CD coefficient. fc is the carrier frequency and f is the symbol rate of the modulating electrical signal ($-F_s/2 \leq f \leq F_s/2$, with F_s: the sampling rate of the ADC). Since $fc \gg f$, $(f_c - f)^2$ can be approximated by ${f_c}^2$, we thus obtain a simplified frequency domain transfer function for CD:

$$H_{CD}(f) \cong \exp(-i\frac{\pi cDL}{{f_c}^2}f^2)$$

The minimum tap length of $H_{CD}\ (f)$ is estimated by $cLDf_{max}F_s/{f_c}^2$, where f_{max} is the frequency of the spectrum edge of the transmitted signal [36].

In our applications, we aim at retransmitting received signals with highest fidelity. Specifically, in some situations, we might want to have the flexibility to retransmit the received signal with the same amount of detected total accumulated CD. Therefore, after having blindly estimated the total accumulated CD in the received signal, we can digitally add CD to the DAC-generated signal. This operation can be simply performed by changing the sign of the fiber CD coefficient D to $-D$ in the CD frequency domain transfer function to add CD in the signal.

Thus, CD addition in the DAC-generated signal can be digitally performed by filtering the generated signal in the time or frequency domain with a linear filter. Specifically, the linear filter is given by:

$$H_{CD}(f) = \exp(i\frac{\pi cDL}{(f_c - f)^2} f^2)$$

Where L is the fiber length, and D is the fiber CD coefficient.

Timing Jitter

Effective Number of Bits and Timing Jitter

ADCs and DACs timing clocks are imperfect and exhibit sampling rate jitter. Sampling jitter is a timing error compared against an ideal sampling clock. Jitter is a random noise, which causes sampling errors and ultimately generates decoding errors. Among the many types of jitter, period jitter most commonly dominates sampling jitter, which can be easily measured as the standard deviation of the clock's period. It is possible to accurately estimate noise due to sampling jitter (or jitter noise) with an oscilloscope, and determine how much the jitter noise degrades the effective number of bits (ENoB) over frequency.

The ENoB compares ideal ADC/DAC noise against other non-ideal noises from signal-to-noise-ratio (SNR). The ENoB of an ADC/DAC architecture is calculated with sinusoidal signals, and is defined at a certain frequency f. The ENoB of an ADC/DAC architecture is given by:

$$ENOB(f) = log_2[SINAD(f)] - \frac{1}{2}log_2\left(\frac{3}{2}\right) - log_2\left(\frac{A}{V/2}\right)$$

Where $SINAD(f)$ is the signal-to-noise-and-distortion ratio of the f-Hz sinusoidal signal. The SINAD is defined by the ratio of the root mean square (RMS) signal amplitude to the mean value of the root-sum-square of all other spectral components, including harmonics:

$$SINAD = \frac{P_{signal} + P_{noise} + P_{distortion}}{P_{noise} + P_{distortion}}$$

If we assume that the amplitude A of the distorted output f-Hz sinusoidal signal is fitted to the full-scale V of the measuring oscilloscope, we have $V = 2A$, yielding:

$$ENoB(f) = log_2[SINAD(f)] - \frac{1}{2}log_2\left(\frac{3}{2}\right)$$

It possible to express the ENoB as a function of the RMS sampling jitter $\sigma_{sampling-jitter}$ of the ADC/DAC of interest. If N is the ADC/DAC architecture number-of-bits (quantization limited ENoB), we have:

$$ENoB(f) = N - \frac{1}{2}log_2[1 + 6(2^N \pi f \sigma_{sampling-jitter})^2]$$

In the limit scenario where the ENoB is jitter limited (N→+∞), we obtain the following theoretical relationship for jitter-limited ENoB:

$$\lim_{N \to +\infty} ENoB(f) = -log_2(\sqrt{6}\pi f \sigma_{sampling-jitter})$$

Because jitter noise increases with frequencies, the ENoB degrades at higher frequencies.

Timing Jitter Estimation

A method to assess sampling jitter consist in measuring the variance of the histogram of the eye diagram sampling time at the eye closing intersection, Fig. 5.2.

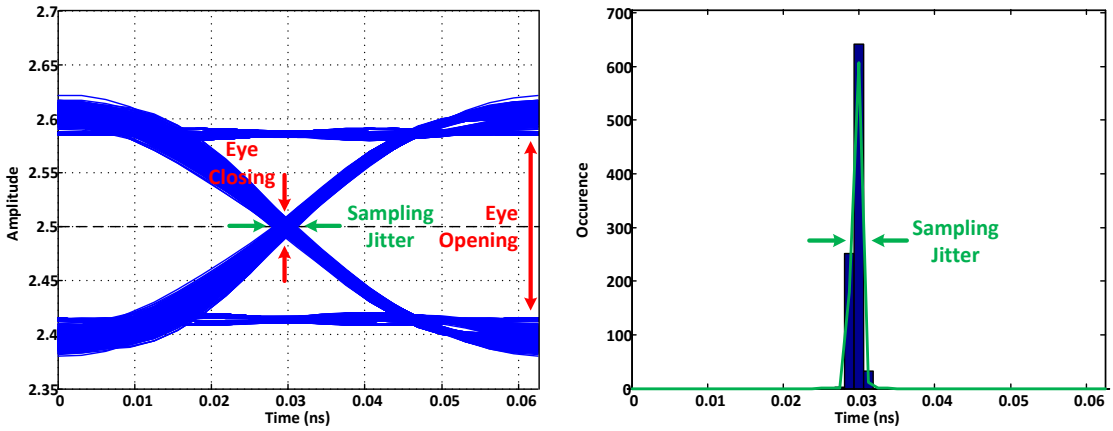

Fig. 5.2. Sampling jitter assessment method based on the histogram of the eye diagram sampling time at the eye closing intersection.

Timing Jitter Addition

We developed a simple method to add sampling jitter in DAC-generated signals based on an sampling-to-amplitude jitter conversion principle, Fig. 5.3.

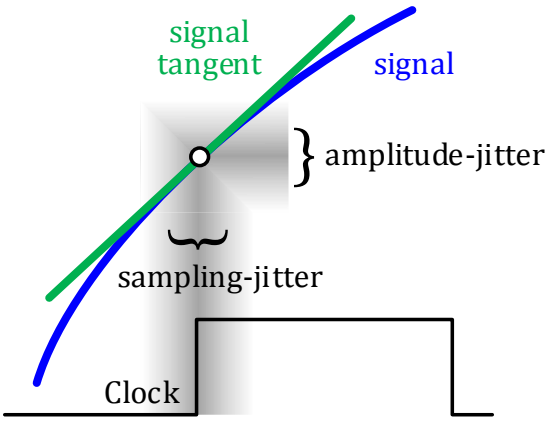

Fig. 5.3. Amplitude-to-sampling jitter conversion principle to add sampling jitter in a DAC-generated signal.

From a DSP perspective, the method utilizes the time derivative of the DAC-generated signal to link sampling jitter to amplitude jitter, Fig. 5.4. Specifically, by controlling the root mean square sampling jitter parameter $\sigma_{sampling-jitter}$, we can influence the resulting amplitude jitter in the DAC-generated signal.

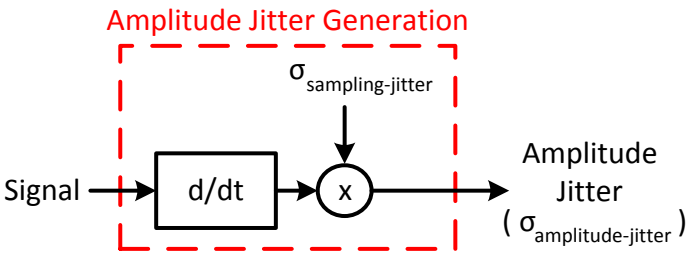

Fig. 5.4. Sampling-to-amplitude jitter conversion principle to add sampling jitter in a DAC-generated signal.

We validated our sampling-to-amplitude jitter generation model by measuring the ENoB degradation versus the input sinusoidal frequency, resulting from sampling jitter addition as proposed in the block diagram in Fig. 5.4. Specifically, we implemented the numerical model presented in Fig. 5.5.

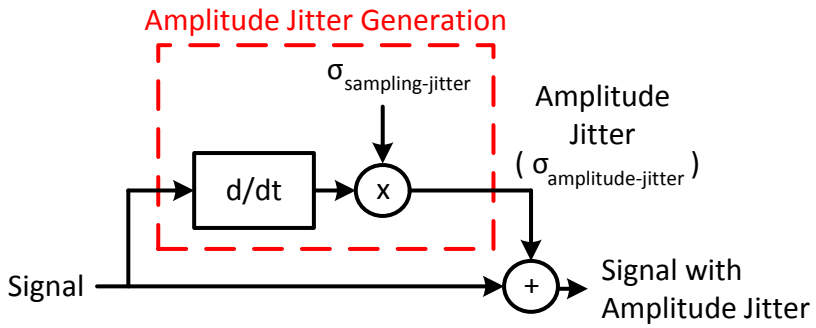

Fig. 5.5. Implemented numerical model to validate the proposed sampling-to-amplitude jitter generation model.

To measure the ENoB resulting from the distorted output signal $f(t)$, we used the block diagram displayed in Fig. 5.6.

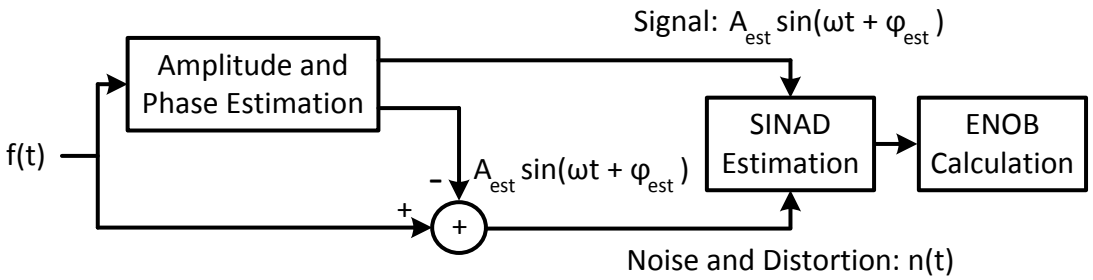

Fig. 5.6. Block diagram to measure the ENOB from the distorted output signal $f(t)$.

The performance of the proposed sampling-to-amplitude jitter generation model is quantified with the ENoB versus input sinusoidal frequency curve, Fig. 5.7. The numerical simulation was carried with a 64 GSa/s sampling clock rate, a digital-to-analog

oversampling rate of 16, and a RMS sampling jitter of 0.600 ps. Simulated results are perfectly matched with the theoretical jitter-limited ENoB formula.

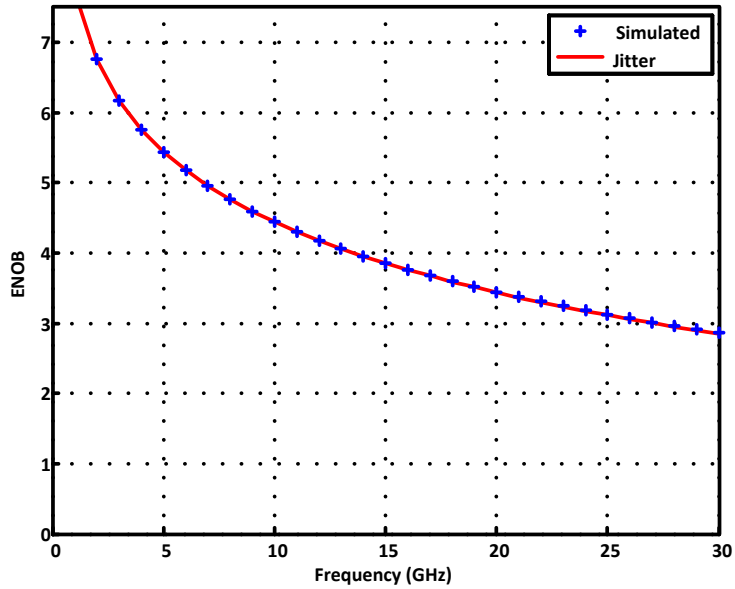

Fig. 5.7. ENoB versus input sinusoidal frequency for the proposed sampling-to-amplitude jitter generation model.

After having validated the proposed sampling-to-amplitude jitter generation model, Fig. 5.5, we investigated how the proposed sampling-to-amplitude jitter generation model can help us model more accurately high-speed DACs imperfect clocks. Thus, we first developed a numerical model for high-speed DACs with imperfect timing clock, Fig. 5.8.

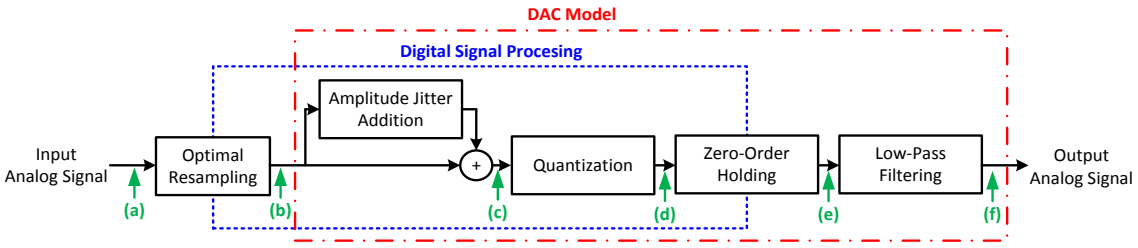

Fig. 5.8. Numerical model for high-speed digital-to-analog converters with imperfect timing clock.

To assess the validity of the proposed model for high-speed DAC with imperfect clock, we quantified its performance with the ENOB versus input sinusoidal frequency curve, Fig. 5.9. The numerical simulation was carried with a 64 GSa/s sampling clock rate, a digital-to-analog oversampling rate of 16, a 6.5 bits architecture (quantization limited ENOB), a 20 GHz low-pass filter (8^{th} order Gaussian filter), and a RMS sampling jitter of 0.600 ps. Simulated results are very close with theoretical formulas. Across the simulated frequencies, an average error of about 1.5 bits was measured between the simulation results and the theoretical formula (quantization + jitter + filter).

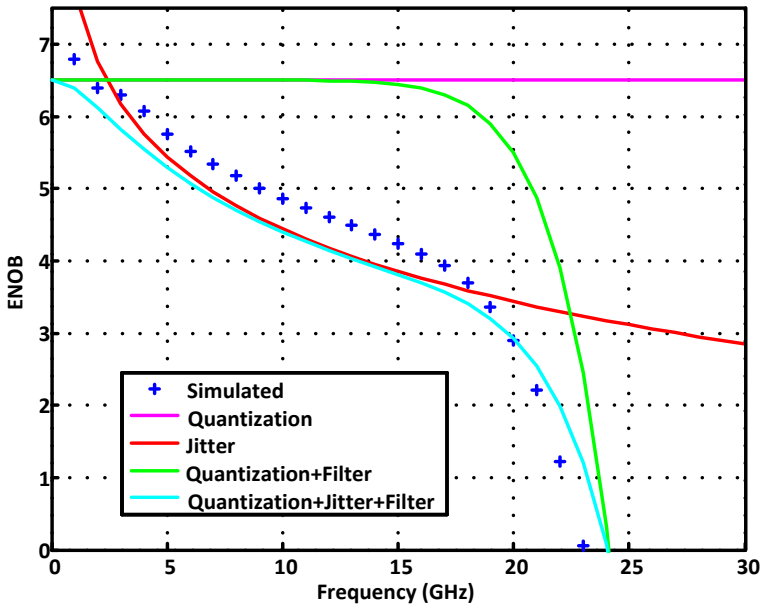

Fig. 5.9. ENoB versus input sinusoidal frequency for the proposed model for high-speed digital-to-analog converter with imperfect clock.

After having validated the proposed model for high-speed DACs with imperfect timing clock, Fig. 5.8, we investigated how the proposed model behaves with broadband communication signals. Specifically, we numerically measured the sampling jitter from sinusoidal and broadband signals generated with the proposed model for high-speed DAC with imperfect clock.

We presented Fig.5.10, the generation process flow for a 16 GHz sinusoidal signal at different points (point a-f, see Fig. 5.8 for labeling) in the proposed high-speed DAC with imperfect clock. The numerical simulations, Figs. 5.10 and 5.11, was carried with a 64 GSa/s sampling clock rate, a digital-to-analog oversampling rate of 16, a 6.5 bits

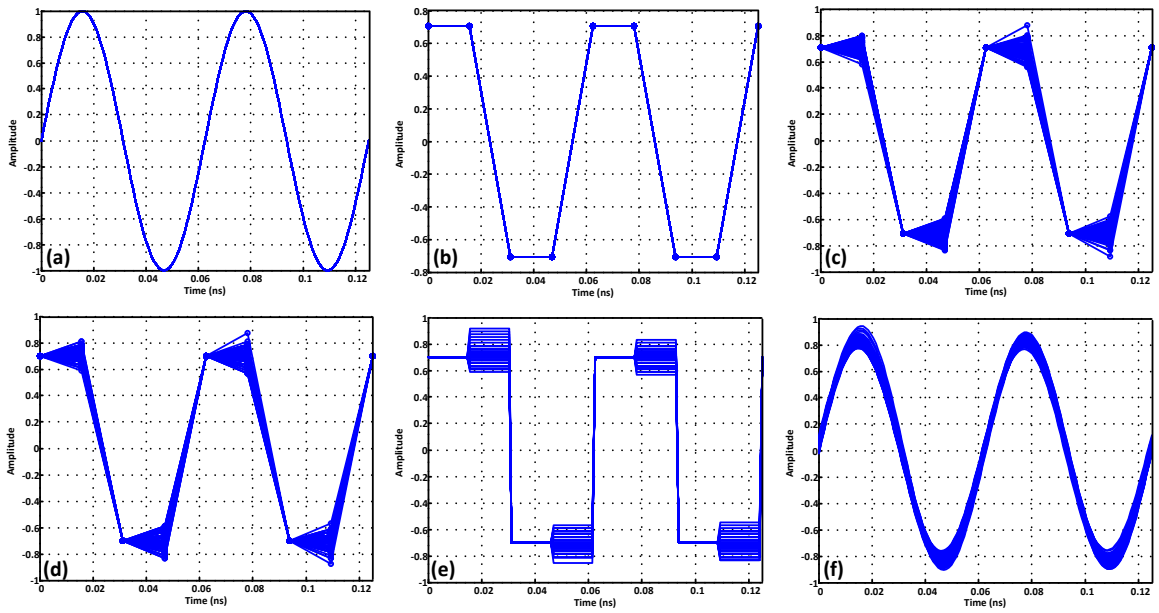

Fig. 5.10. Generation process flow for a 16 GHz sinusoidal signal at different points in the proposed model for high-speed DAC with imperfect clock. (a) Input analog signal; (b) Digital signal after optimal resampling; (c) Digital signal after jitter addition; (d) Digital signal after quantization; (e) Analog signal after zero-order holding; (f) Output analog signal. The root mean square sampling jitter value is 0.600 ps.

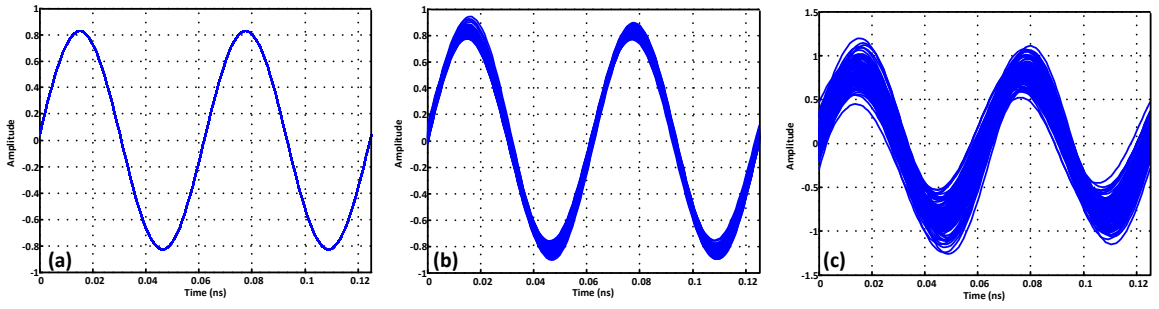

Fig. 5.11. Generated 16 GHz sinusoidal signals with the proposed model for high-speed DAC with imperfect clock for different root mean square sampling jitter values: (a) No sampling jitter; (b) 0.600 ps; (c) 3 ps.

architecture (quantization limited ENOB), and a 20 GHz low-pass filter (8th order Gaussian filter).

Fig. 5.12 represents the measured root mean square sampling jitter values for different sinusoidal signals frequencies (4 GHz, 8 GHz, 16 GHz) generated with the proposed model for high-speed DAC with imperfect clock for different input root mean square sampling jitter values. The numerical simulation was carried with a 64 GSa/s sampling clock rate, a digital-to-analog oversampling rate of 16, a 6.5 bits architecture (quantization limited ENOB), and a 20 GHz low-pass filter (8th order Gaussian filter). The RMS Jitter in decibels is defined as:

$$RMS\ Jitter\ (dB) = 10log_{10}(RMS\ Jitter\ x\ Symbol\ Rate)$$

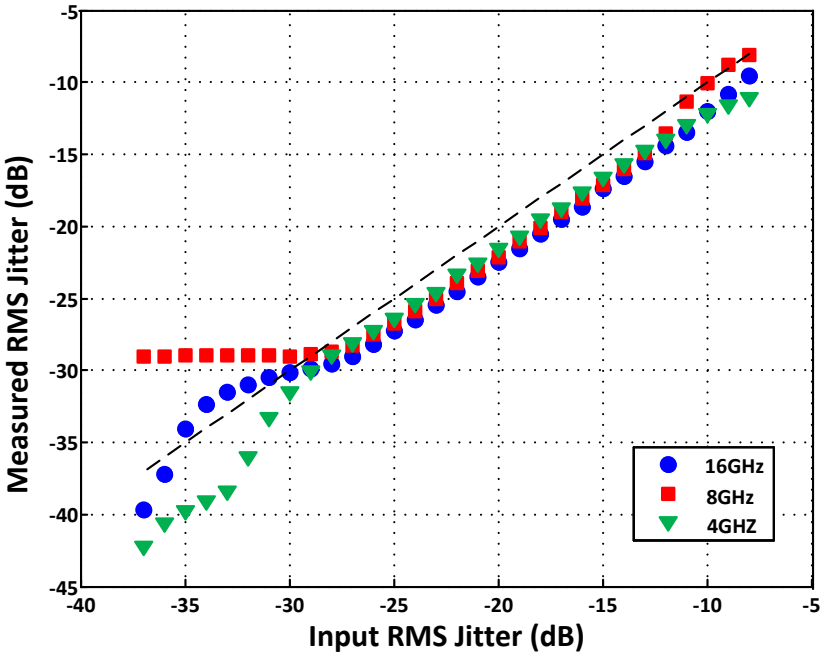

Fig. 5.12. Measured root mean square sampling jitter for different sinusoidal signals frequencies generated with the proposed model for high-speed DAC with imperfect clock for different input root mean square sampling jitter values.

We presented Fig. 5.13, the generation process flow for the real part of a 32 Gbaud NRZ-QPSK signal (zero roll-off) at different points (point a-f, see Fig. 5.8 for labeling) in the proposed high-speed DAC with imperfect clock.

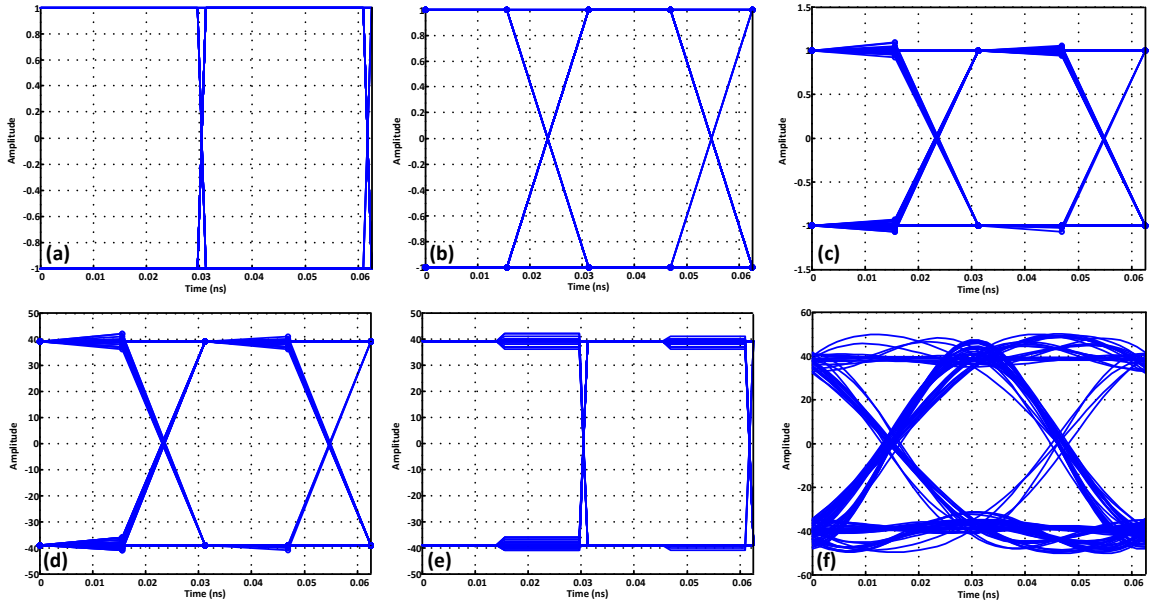

Fig. 5.13. Generation process flow for the real part of a 32 Gbaud NRZ-QPSK signal (zero roll-off) at different points in the proposed model for high-speed DAC with imperfect clock. (a) Input analog signal; (b) Digital signal after optimal resampling; (c) Digital signal after jitter addition; (d) Digital signal after quantization; (e) Analog signal after zero-order holding; (f) Output analog signal. The root mean square sampling jitter value is 0.3125 ps.

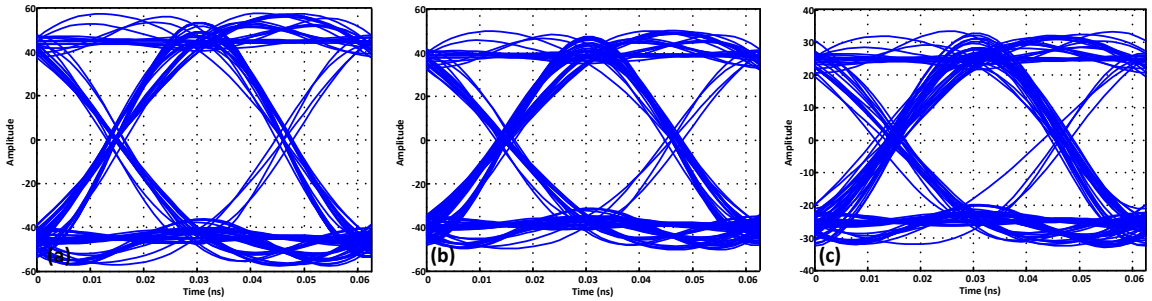

Fig. 5.14. Generated real part of the 32 Gbaud NRZ-QPSK signal (zero roll-off) with the proposed model for high-speed DAC with imperfect clock for different root mean square sampling jitter values: (a) No sampling jitter; (b) 0.3125 ps; (c) 1.5662 ps.

The numerical simulation, Figs. 5.13 and 5.14, was carried with a 64 GSa/s sampling clock rate, a digital-to-analog oversampling rate of 16, a 6.5 bits architecture (quantization limited ENOB), and a 20 GHz low-pass filter (8th order Gaussian filter).

Fig. 5.15 represents the measured root mean square sampling jitter values for different NRZ-QPSK signals (zero roll-off) symbol rates (16 GBaud, 24 GBaud, 32 GBaud) generated with the proposed model for high-speed DAC with imperfect clock for different input root mean square sampling jitter values. The numerical simulation was carried with a 64 GSa/s sampling clock rate, a digital-to-analog oversampling rate of 16, a 6.5 bits architecture (quantization limited ENOB), and a 20 GHz low-pass filter (8th order Gaussian filter). The RMS Jitter in decibels is defined as:

$$RMS\ Jitter\ (dB) = 10log_{10}(RMS\ Jitter\ x\ Symbol\ Rate)$$

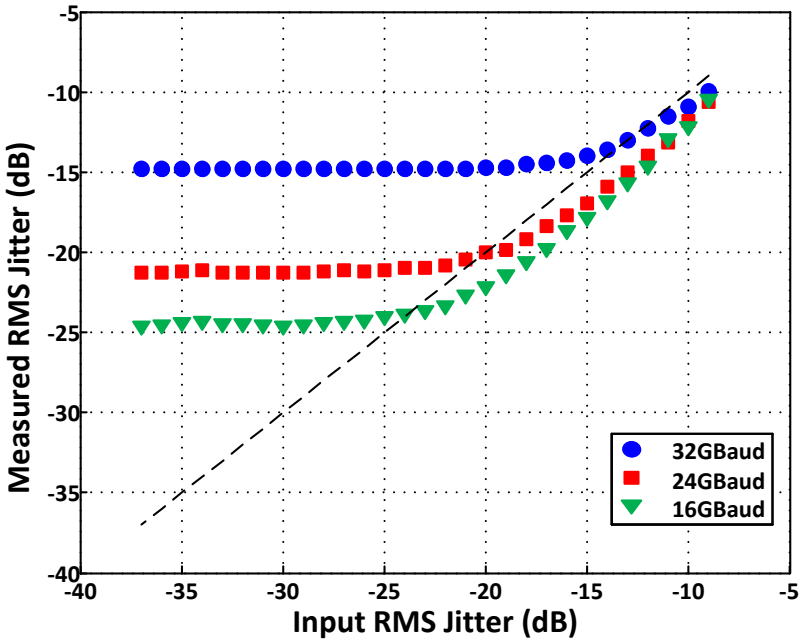

Fig. 5.15. Measured root mean square sampling jitter for different NRZ-QPSK signals (zero roll-off) symbol rates generated with the proposed model for high-speed DAC with imperfect clock for different input root mean square sampling jitter values.

CHAPTER 6

CONCLUSIONS

6.1 BLIND SIGNAL IDENTIFICATION

We introduced in this dissertation the concept of autonomous receiver (Chapter 4 - Section 1) and presented various architectures for fiber optic communication links (Chapter 4 - Section 3) and for photonic assisted wireless communication links (Chapter 4 - Section 4), capable of operating fully autonomously to identify and demodulate, without prior knowledge, received broadband communication signals. These autonomous architectures utilize blind parameters estimation algorithms to autonomously estimate link impairments parameters, and recognize the received signal parameters, including the modulation format (Chapter 4 - Section 5). Experimental validation was carried on optical signals transported over hundreds of kilometers of optical fiber, and on radio frequency signals transported wirelessly (Chapter 4 - Section 6).

6.2 BLIND SIGNAL RECONSTRUCTION

We introduced the concept of signal reconstruction for fiber optic communication links (Chapter 5 - Section 1) and presented an autonomous receiver-assisted DAC-based architecture for signal generation that constructs or reconstructs any signal, for a wide range of signal parameters and link impairments parameters (Chapter 5 - Section 3).

INTELLECTUAL PROPERTY

PATENTS

[1] **P. Isautier**, K. Mehta, A.J. Stark, and S.E. Ralph, "Systems and Methods for Autonomous Signal Modulation Format Identification", U.S. Patent Application No.: 14/221,246, patent pending.

[2] **P. Isautier**, and S.E. Ralph, "Systems and Methods for Autonomous Signal Modulation Format Identification", U.S. Patent Application No.: 14/475,648, patent pending.

[3] **P. Isautier**, and S.E. Ralph, "Systems and Methods for Autonomous Signal Modulation Format Identification", U.S. Patent Application No.: 14/587,306, patent pending.

INVENTION DISCLOSURE

[1] **P. Isautier**, and S.E. Ralph, "Time-Domain Hybrid Modulation Format Recognition Method for Autonomous Software-Defined Coherent Optical Receivers", Georgia Tech Research Corporation ID #6896, filed Spring 2015.

JOURNAL PUBLICATIONS

[1] J. Pan, **P. Isautier**, M. Alfiad, S. Tibuleac, and S.E. Ralph, "In-Band Crosstalk Penalty Analysis Based on Gaussian Noise Model", to be submitted to the J. of Lightw. Technol., 2015.

[2] **P. Isautier**, J. Pan, R. DeSalvo, and S.E. Ralph, "Stokes Space-Based Modulation Format Recognition for Autonomous Optical Receivers", accepted to the J. of Lightw. Technol., 2015.

[3] M. Sodagar, A. H. Hosseinnia, **P. Isautier**, H. Moradinejad, S. E. Ralph, A. A. Eftekhar, and A. Adibi, "Compact, 15 Gb/s Electro-Optic Modulator Through Carrier Accumulation in a Hybrid Si/SiO2/Si Microdisk", Opt. Express, vol.23, no. 22, pp. 28306-28315, Nov. 2015.

[4] **P. Isautier**, K. Mehta, A.J. Stark, and S.E. Ralph, "Robust Architecture for Autonomous Coherent Optical Receivers", J. Opt. Commun. Netw., vol. 7, no. 9, pp. 864-874, Sep. 2015.

[5] A.J. Stark, **P. Isautier**, J. Pan, S.K. Pavan, M. Filer, S. Tibuleac, R. Lingle, Jr., R. DeSalvo, and S.E. Ralph, "Advanced Signaling Technologies for High-Speed Digital Fiber-Optic Links", Applied Optics, vol. 53, no. 25, pp. 5824-5840, Sep. 2014.

CONFERENCE PRESENTATIONS

[1] **P. Isautier**, S. Varughese, J. Langston, M. Pratt, J. Lavrencik, A. Melgar, M. Alfiad, S. Tibuleac, and S.E. Ralph, "Sampling Jitter of Digital-to-Analog Converters: Simulation Methods and Performance of Experimental 64QAM Systems", submitted to the Conference on Optical Fiber Communication (OFC), Anaheim, CA, USA, Mar. 2016.

[2] M. Sodagar, A. H. Hosseinnia, **P. Isautier**, S.E. Ralph, A. A. Eftekhar, and A. Adibi, "15 Gb/s Accumulation-based Micro-disk Modulator", submitted to the Conference on Optical Fiber Communication (OFC), Anaheim, CA, USA, Mar. 2016.

[3] **P. Isautier**, and S.E. Ralph, "Autonomous Identification and Detection for Multi-Gigabit Photonic", IEEE International Topical Meeting on Microwave Photonics (MWP), Paphos, Cyprus, Oct. 2015.

[4] J. Langston, **P. Isautier**, and S.E. Ralph, "Simple Nonlinear Post-Compensator for Coherent Detection", IEEE Photonics Conference (IPC), Reston, VA, Oct. 2015.

[5] J. Pan, **P. Isautier**, S. Tibuleac, and S.E. Ralph, "A Novel Channel Estimation Technique for transmitter Side Narrowband Filtering Compensation", IEEE Photonics Conference (IPC), Reston, VA, Oct. 2015.

[6] **P. Isautier**, J. Pan, and S.E. Ralph, "Autonomous Receiver Architecture for Multi-Gigabit Photonic Assisted RF Signals", European Conference and Exhibition on Optical Communication (ECOC), Valencia, Spain, Sep. 2015.

[7] **P. Isautier**, J. Langston, J. Pan, and S.E. Ralph, "Agnostic Software-Defined Coherent Optical Receiver Performing Time-Domain Hybrid Modulation Format Recognition", Th2A.21, Conference on Optical Fiber Communication (OFC), Los Angleles, CA, USA, Mar. 2015.

[8] J. Pan, **P. Isautier**, M. Filer, S. Tibuleac, and S.E. Ralph, "Addition of In-band Crosstalk to the Gaussian Noise Model", Th2A.22, Conference on Optical Fiber Communication (OFC), Los Angleles, CA, USA, Mar. 2015.

[9] S. Hughes, J. Pan, J. S. Langston, **P. Isautier**, H. Shankar, and S.E. Ralph, "Linearity Requirements of QAM Transmitters", Th2A.12, Conference on Optical Fiber Communication (OFC), Los Angleles, CA, USA, Mar. 2015.

[10] **P. Isautier**, J. Pan, J. Langston, R. DeSalvo, and S.E. Ralph, "Autonomous Receivers for Complex Format Identification and Demodulation", TuB2, Avionics, Fiber-Optics and Photonics Technology Conference (AVFOP), Atlanta, GA, USA, Nov. 2014.

[11] **P. Isautier**, J. Pan, J. Langston, and S.E. Ralph, "Performance Comparison of Autonomous Software-Defined Coherent Optical Receivers", MG3.2, IEEE Photonics Conference (IPC), San Diego, CA, USA, Oct. 2014.

[12] J. Pan, **P. Isautier**, J. S. Langston, and S.E. Ralph, "DAC Enabled Frequency Domain Pre-Shaper Design for Nyquist Signaling", SM3E.2, Signal Processing in Photonics Communications (SPPCom), San Diego, CA, USA, Jul. 2014.

[13] **P. Isautier**, J. Pan, and S.E. Ralph, "Robust Autonomous Software-Defined Coherent Optical receiver", W1G.7, Conference on Optical Fiber Communication (OFC), San Francisco, CA, USA, Mar. 2014.

[14] J. Pan, **P. Isautier**, and S.E. Ralph, "Gaussian Noise Model Aided In-band Crosstalk Analysis in ROADM-enabled DWDM Networks", Th1I.1, Conference on Optical Fiber Communication (OFC), San Francisco, CA, USA, Mar. 2014.

[15] **P. Isautier**, A. J. Stark, J. Pan, K. Mehta, and S.E. Ralph, "Autonomous Software-Defined Coherent Optical Receivers Performing Modulation Format Recognition in Stokes-Space", P.3.30, European Conference and Exhibition on Optical Communication (ECOC), London, UK, Sep. 2013.

[16] J. Pan, **P. Isautier**, and S.E. Ralph, "Digital Pre-shaping for Narrowband Filtering Impairment Compensation in Superchannel Applications", JT3A.1, Signal Processing in Photonics Communications (SPPCom), Rio Grande, PR, USA, Jul. 2013.

[17] **P. Isautier**, A. J. Stark, K. Mehta, R. DeSalvo, and S.E. Ralph, "Autonomous Software-Defined Coherent Optical Receivers", OTh3B.4, Conference on Optical Fiber Communication (OFC), Anaheim, CA, USA, Mar. 2013.

REFERENCES

CHAPTER 1

[1] Cisco, "Cisco Visual Networking Index: Forecast and Methodology, 2014-2019," May 2015.

[2] R. Ramaswami, K.N. Sivarajan, and G. H. Sasaki, "Introduction to Optical Networks", Optical Networks: A Practical Perspective, 3rd ed. Morgan Kaufmann, Chapter 1, 2009.

[3] Accenture, "The Future Communications Service Provider," 2013.

[4] C. Laperle, and M. O'Sullivan, "High-Speed DACs and ADCs for Next Generation Flexible Transceivers", SM3E.1, in Signal Processing in Photonics Communications (SPPCom), San Diego, CA, USA, Jul. 2014.

[5] K. Roberts, and C. Laperle, "Flexible Transceivers", We.3.A.3, in European Conference and Exhibition on Optical Communication (ECOC), Amsterdam, Netherlands, Sep. 2012.

[6] S. Koenig, J. Antes, D. Lopez-Diaz, R. Schmogrow, T. Zwick, C. Koos, W. Freude, J. Leuthold, and I. Kallfass, "20 Gbits/s Wireless Bridge at 220 GHz Connecting two Fiber-Optic Links", Journal of Optical Communications and Networking, vol. 6, no. 1, pp. 54-61, Jan. 2014.

CHAPTER 2

[7] R. Ramaswami, K.N. Sivarajan, and G. H. Sasaki, Optical Networks: A Practical Perspective, 3rd ed. Morgan Kaufmann, 2009.

[8] S. Kumar, and M. Jamal Deen, Fiber Optic Communications: Fundamentals and Applications, 1st ed. Wiley, 2014.

[9] J. Pan, G.-K. Chang, M. Bloch, S. Tibuleac, E. W. Zegura, and S.E. Ralph, "Advanced System Design and Performance Analysis for High-Speed Optical Communications", Doctoral Dissertation, The Georgia Institute of Technology, 2015.

[10] A. J. Stark, G.-K. Chang, R. Lingle Jr., S. Tibuleac, M. Chapman, and S.E. Ralph, "Advanced System Design and Performance Analysis for High-Speed Optical Communications", Doctoral Dissertation, The Georgia Institute of Technology, 2015.

[11] Cisco, "Fiber Types in Gigabit Optical Communications," http://www.cisco.com/c/en/us/products/collateral/interfaces-modules/transceiver-modules/white_paper_c11-463661.html

[12] E. Ip, A. Pak Tao Lau, D. F. J. Barros, and J. M. Kahn, "Coherent Detection in Optical Fiber Systems", Optics Express, vol. 16, no. 2, pp. 753-791, Jan. 2008.

[13] R.-J. Essiambre, and R. W. Tkach, "Capacity Trends and Limits of Optical Communication Networks", Proc. IEEE, vol. 100, no. 5, pp. 1035-1055.

[14] A.P.T. Lau, Y. Gao, Q. Sui, D. Wang, Q. Zhuge, M.H. Mosry-Osman, M. Chagnon, X. Xu, C. Lu, and D.V. Plant, "Advanced DSP Techniques Enabling High Spectral Efficiency and Flexible Transmissions", IEEE Signal Processing Magazine, pp. 82-92, Mar. 2014.

[15] C. R. S. Fludger, et al., "Coherent Equalization and POLMUX-RZ-DQPSK for Robust 100-GE Transmission," J. Lightw. Technol., vol. 26, no. 1, Jan. 2008.

[16] X. Liu, et al., "Efficient digital coherent detection of a 1.2 Tb/s 24-carrier no-guard interval CO-OFDM signal by simultaneously detection multiple carriers per sampling," in Conference on Optical Fiber Communication (OFC), San Diego, CA, Mar. 2010.

[17] S. Chandrasekhar, et al., "Transmission of 1.2 Tb/s 24-carrier no-guard-interval coherent OFDM super-channel over 7200 km of ultra-large-area fiber," Eur. Conf. Optical Communication (ECOC), Vienna, Austria, Sept. 2009.

[18] Y. Ma, et al., "1-Tb/s single-channel coherent optical OFDM transmission with orthogonal-band multiplexing and subwavelength bandwidth access," J. Lightw. Technol., vol. 28, no. 4, Feb. 2010.

[19] S. K. Ibrahim, et al., "Toward a Practical Implementation of Coherent WDM: Analytical, Numerical, and Experimental Studies," IEEE Photonics Journal, Vol. 2, No. 5, Oct. 2010.

[20] F. Tian, et al., “Generation of 50 Stable Frequency-Locked Optical Carriers for Tb/s Multicarrier Optical Transmission Using a Recirculating Frequency Shifter,” J. Lightw. Technol., vol. 29, no. 8, Apr. 2011.

[21] J. Sakaguchi, et al., “19-core fiber transmission of 19x100x172-Gb/s SDM-WDM-PDMQPSK signals at 305 Tb/s,” in Conference on Optical Fiber Communication (OFC), Los Angeles, CA, Mar. 2012, paper PDP5C.1.

[22] X. Chen, et al., “Reception of Dual-LP11-Mode CO-OFDM Signals through Few-mode Compatible Optical Add/Drop Multiplexer,” in Conference on Optical Fiber Communication (OFC), Los Angeles, CA, Mar. 2012, paper PDP4B.4.

[23] R. Ryf, et al., “Low-Loss Mode Coupler for Mode-Multiplexed transmission in Few-Mode Fiber,” in Conference on Optical Fiber Communication (OFC), Los Angeles, CA, Mar. 2012, paper PDP5B.5.

[24] L. Gruner-Nielsen, et al., “Few Mode Transmission Fiber with low DGD, low Mode Coupling and low Loss,” in Conference on Optical Fiber Communication (OFC), Los Angeles, CA, Mar. 2012, paper PDP5A.1.

[25] R. Ryf, et al., “Space-Division Multiplexed Transmission over 4200 km 3-Core Microstructured Fiber,” in Conference on Optical Fiber Communication (OFC), Los Angeles, CA, Mar. 2012, paper PDP5C.2.

[26] N. K. Fontaine, “Space-division multiplexing and all-optical MIMO demultiplexing using a photonic integrated circuit,” in Conference on Optical Fiber Communication (OFC), Los Angeles, CA, Mar. 2012, paper PDPB.1.

[27] P. J. Winzer, “High-Spectral-Efficiency Optical Modulation Formats”, J. Lightw. Technol., vol.30, no.24, pp.3824-3835, Dec. 2012.

[28] R. Ramaswami, K.N. Sivarajan, and G. H. Sasaki, “Introduction to Optical Networks”, Optical Networks: A Practical Perspective, 3rd ed. Morgan Kaufmann, Chapter 2, 2009.

[29] S. Kumar, and M. Jamal Deen, Fiber Optic Communications: Fundamentals and Applications, 1st ed. Wiley, Chapter 2, 2014.

[30] S. Kumar, and M. Jamal Deen, Fiber Optic Communications: Fundamentals and Applications, 1st ed. Wiley, Chapter 1, 2014.

[31] R. Ramaswami, K.N. Sivarajan, and G. H. Sasaki, "Introduction to Optical Networks", Optical Networks: A Practical Perspective, 3rd ed. Morgan Kaufmann, Appendix D, 2009.

[32] S. Kumar, and M. Jamal Deen, Fiber Optic Communications: Fundamentals and Applications, 1st ed. Wiley, Chapter 10, 2014.

[33] R. Ramaswami, K.N. Sivarajan, and G. H. Sasaki, "Introduction to Optical Networks", Optical Networks: A Practical Perspective, 3rd ed. Morgan Kaufmann, Chapter 3, 2009.

[34] R. Ramaswami, K.N. Sivarajan, and G. H. Sasaki, "Introduction to Optical Networks", Optical Networks: A Practical Perspective, 3rd ed. Morgan Kaufmann, Chapter 4, 2009.

[35] S. Kumar, and M. Jamal Deen, Fiber Optic Communications: Fundamentals and Applications, 1st ed. Wiley, Chapter 5, 2014.

[36] R. Kudo, T. Kobayashi, K. Ishihara, Y. Takatori, A. Sano, and Y. Miyamoto, "Coherent Optical Single Carrier Transmission Using Overlap Frequency Domain Equalization for Long-Haul Optical Systems", J. Lightw. Technol., 27, 16, pp.3721-3728, 2009.

[37] M. Oerder, and H. Meyr, "Digital filter and square timing recovery", IEEE Transactions on Communications, vol. 36, no. 5, pp. 605–612, May 1988.

[38] F. Gardner, "A BPSK/QPSK timing-error detector for sampled receivers", IEEE Transactions on Communications, vol. 34, no. 5, pp. 423– 429, May 1986.

[39] D. Godard, "Passband timing recovery in an all-digital modem receiver", IEEE Transactions on Communications, vol. 26, no. 5, pp. 517–523, May 1978.

[40] S. Lee, "A new non-data-aided feedforward symbol timing estimator using two samples per symbol", IEEE Communications Letters, vol. 6, no. 5, pp. 205–207, May 2002.

[41] K. Shi, Y. Wang, and E. Serpedin, "On the design of a digital blind feedforward, nearly jitter-free timing recovery scheme for linear modulations", IEEE Transactions on Communications, vol. 52, no 9, pp. 1464–1469, Sep. 2004.

[42] Y. Wang, E. Serpedin, and P. Ciblat, "An alternative blind feedforward symbol timing estimator using two samples per symbol", IEEE Transactions on Communications, vol. 51, no. 9, pp. 1451–1455, Sep. 2003.

[43] E. Panayirci, and E. K. Bar-Ness, "A new approach for evaluating the performance of a symbol timing recovery system employing a general type of nonlinearity", IEEE Transactions on Communications, vol. 44, no. 1, pp. 29–33, Jan. 1996.

[44] T. T. Fang, "Analysis of self-noise in a fourth-power clock regenerator", IEEE Transactions on Communications, vol. 39, no. 1, pp. 133–140, Jan. 1991.

[45] M. Morelli, A. N. D'Andrea, and U. Mengali, "Feedforward ML-based timing estimation with PSK signals", IEEE Communications Letters, vol. 1, no. 3, pp. 80–82, May 1997.

[46] H. Sun, and K. Wu, "A novel dispersion and PMD tolerant clock phase detector for coherent transmission systems", SPWC5, in Conference on Optical Fiber Communication (OFC), Los Angeles, CA. USA, Mar. 2011.

[47] K. Kikuchi, "Polarization-demultiplexing algorithm in the digital coherent receiver", MC2.2, in IEEE/LEOS Summer Topical Meetings, Jul. 2008.

[48] A. Hyvärinen, Independent Component Analysis, New York : J. Wiley, 2001.

[49] D.N. Godard, "Self-recovering equalization and carrier tracking in two-dimensional data communication systems", IEEE Trans. On. Commun., COM-28, 11, pp. 1867-1875, 1980.

[50] S. Amari, S.C. Douglas, A. Chichocki, and H.H. Yang., "Multichannel Blind Deconvolution and Equalization using Natural Gradient", in 1st IEEE Workshop on Signal Processing Advances in Wireless Communications (SPAWC), Paris, France, Apr. 1997.

[51] M. Morelli, and U. Mengali, "Feedforward frequency estimation for PSK: a tutorial review", Eur. Trans. Telecommun., 9, 2, pp. 103-119, 1998.

[52] M. Nakazawa, et al., "Ultrahigh-speed "orthogonal" TDM transmission with an optical Nyquist pulse train". Optics Express, 2012. 20(2): p. 1129-1140.

[53] G. Picchi and G. Prati, "Blind Equalization and Carrier Recovery Using a 'Stop-and-Go' Decision-Directed Algorithm", IEEE Transactions on Communications, vol. COM-35, No. 9, pp.877-887, Sep. 1987.

CHAPTER 3

[54] R. W. Thomas, L. A. DaSilva, and A. B. MacKenzie, "Cognitive Networks," in IEEE International Symposium on New Frontiers in Dynamic Spectrum Access Networks, vol. 1. IEEE, pp. 352–360, 2005.

[55] J. III Mitola, "Cognitive Radio: an Integrated Agent Architecture for Software Defined Radio," Doctoral Dissertation, Royal Institute of Technology (KTH), 2000.

[56] R. Borkowski, I. Tafur Monroy, D. Zibar, "Enabling Technologies for Cognitive Optical networks", Doctoral Dissertation, Technical University of Denmark (DTU), 2014.

[57] W. Wei, C. Wang, and J. Yu, "Cognitive optical networks: key drivers, enabling techniques, and adaptive bandwidth services," IEEE Communications Magazine, vol. 50, no. 1, pp. 106–113, Jan. 2012.

[58] C. E. Shannon, "A Mathematical Theory of Communication," Bell System Technical Journal, vol. 27, no. 3, pp.379-423, Jul. 1948.

[59] X. Zhou, L. E. Nelson, and P. Magill, "Rate-Adaptable Optics for Next-Generation Long-Haul Transport Networks", IEEE Communications Magazine, pp. 41-49, Mar. 2013.

[60] B.T. Teipen, M.H. Eiselt, K. Grobe, and J.-P. Elbers, "Adaptive Data Rates for Flexible Transceivers in Optical Networks", Journal of Networks, vol. 7, no. 5, pp. 776-782, May 2012.

[61] J. Mitola, "The Software Radio Architecture", IEEE Communications Magazine, vol. 33, no. 5, pp. 26-38, May 1995.

[62] J. Zhang, Y. Zhao, H. Yang, Y. Ji, H. Li, Y. Lin, G. Li, J. Han, Y. Lee, and T. Ma, "First Demonstration of Enhanced Software Defined Networking (eSDN) over Elastic Grid (eGrid) Optical Networks for Data Center Service Migration", PDP5B.1, in Conference on Optical Fiber Communication (OFC), Anaheim, CA, USA, Mar. 2013.

[63] M. Channegowda, R. Nejabati, and D. Simeonidou, "Software-Defined Optical Networks Technology and Infrastructure: Enabling Software-Defined Optical Networks Operations [Invited]", Journal of Optical Communications and Networking, vol. 5, no. 10, pp. A274-A282, Oct. 2013.

[64] H-M. Chin, K. Shi, R. Maher, M. Paskov, B. Thomsen, and S. Savory, "Fast Optical Spectrum Estimation using a Digital Coherent Receiver", paper P.3.23, presented at the 39 Eur. Conf. Exhib. Optical Communication, London, UK, Sept. 22-26, 2013.

[65] F. Pittala, F.N. Hauske, Y. Ye, N.G. Gonzalez, and I.T. Monroy, "Fast and robust CD and DGD estimation based on data-aided channel estimation", We.D1.5, in International Conference on Transparent Optical Networks (ICTON), Stockholm, Sweden, Jun. 2011.

[66] F.N.Hauske, Y. Ye, I.T. Monroy, F. Pittala, and N.G. Gonzalez, "Combined CD and DGD monitoring based on data-aided channel estimation", SPTuC3, in Signal Processing in Photonics Communications (SPPCom), Toronto, Canada, Jun. 2011.

[67] F. Pittala, F.N. Hauske, Y. Ye, N.G. Gonzalez, and I.T. Monroy, "Data-aided frequency-domain channel estimation for CD and DGD monitoring in coherent transmission systems", THBB3, in IEEE Photonics Conference (IPC), Arlington, VA, USA, Oct. 2011.

[68] F. Pittala, F.N. Hauske, Y. Ye, N.G. Gonzalez, and I.T. Monroy, "Joint PDL and in-band OSNR monitoring supported by data-aided channel estimation", OW4G.2, in Conference on Optical Fiber Communication (OFC), Los Angeles, CA, USA, Mar. 2012.

[69] F. Pittala J. Qi, M. Msallem, and J.A. Nossek, "Joint frame synchronization and frequency offset estimation in coherent optical transmission systems", Mo.4D.4, in European Conference and Exhibition on Optical Communication (ECOC), London, UK, Sep. 2013.

[70] F. Pittala, and J.A. Nossek, "Training-aided frequency offset estimation in 16-QAM Nyquist transmission systems", MG2.3, in IEEE Photonics Conference (IPC), Bellevue, WA, USA, Sep. 2013.

[70] F. Pittala, I. Slim, A. Mezghani, and J.A. Nossek, "Training-Aided Frequency-Domain Channel Estimation and Equalization for Single-Carrier Coherent Optical Transmission Systems", Journal of Lightwave Technology, vol. 32, no. 24, pp. 4247-4261, Dec. 2014.

[72] R. Elschner, F. Frey, C. Meuer, J.K. Fischer, S. Alreesh, C. Schmidt-Langhorst, L. Molle, T. Tanimura, and C. Schubert, "Experimental Demonstration of a Format-Flexible Single-Carrier Coherent Receiver Using Data-Aided Digital Signal Processing", Optics Express, vol. 20, no. 27, pp. 28786-28791, Dec. 2012.

[73] M. Kuschnerov, M. Chouayakh, K. Piyawanno, B. Spinnler, E. de Man, P. Kainzmaier, M.S. Alfiad, A. Napoli, and B. Lankl, "Data-Aided Versus Blind Single-Carrier Coherent Receivers", IEEE Photonics Journal, vol. 2, no. 3, pp.387-403, Jun. 2010.

[74] M. Kuschnerov, F.N. Hauske, K. Piyawanno, B. Spinnler, A. Napoli, and B. Lankl, "Adaptive Chromatic Dispersion Equalization for Non-Dispersion Managed Coherent Systems", OMT1, in Conference on Optical Fiber Communication (OFC), San Diego, CA, USA, Mar. 2009.

[75] Y. Meng, T. Zhenning, Z. Huijian, Y. Weizhen, T. Hoshida, and J.C. Rasmussen, "Adaptive Blind Equalization for Coherent Optical BPSK System", Th.9.A.4, in European Conference and Exhibition on Optical Communication (ECOC), Torino, Italy, Sep. 2010.

[76] S. Guo, F. Xu, W. Xu, and K. Fan, "Weighted Multi-Modulus Blind Equalization Algorithm Based on Momentum Term", in T. Zhang (Ed.), Mechanical Engineering and Technology, Springer, 2011.

[77] A.J. Viterbi and A.M. Viterbi, "Nonlinear estimation of PSK-Modulated carrier phase with application to burst digital transmission", IEEE Transactions on Information Theory, vol. IT-29, No. 4, pp.543-551, Jul. 1983.

[78] S. Abrar, and A.K. Nandi, "Adaptive Solution for Blind Equalization and Carrier-Phase Recovery of Square-QAM", IEEE Signal Processing Letters, vol. 17, no. 9, pp. 791-794, Sep. 2010.

[79] T. Inoue, and S. Namiki, "DSP-Implementable Block Processing of Carrier-Phase Recovery for M-QAM Signals", W3K.6, in Conference on Optical Fiber Communication (OFC), San Francisco, CA. USA, Mar. 2014.

[80] M.V. Ionescu, M.S. Erkilinc, M. Paskov, S.J. Savory, and B.C. Thomsen, "Novel Baud-Rate estimation Technique for M-PSK and QAM Signals Based on the Standard Deviation of the Spectrum", in European Conference and Exhibition on Optical Communication (ECOC), London, UK, Sep. 2013.

[81] L. Mazet and P. Loubaton, "Cyclic correlation based symbol rate estimation", in Thirty-Third Asilomar Conference on Signals, Systems, and Computers, no. 2, pp.1008-1012, 1999.

[82] G. Sun, A. Jianping, J. Yang, J. Yang, and Z. Li, "Symbol Rate Estimation Using Cyclic Correlation and Haar Wavelet Transform", in International Conference on Wireless Communications, Networking and Mobile Computing, Oct. 2008.

[83]Q. Sui, A.P.T. Lao, and C. Lu, "OSNR Monitoring in the Presence of First-Order PMD Using Polarization Diversity and DSP", Journal of Lightwave Technology, vol. 28, no. 15, pp. 2105-2114, Aug. 2010.

[84] N. G. Gonzalez, D. Zibar, and I. T. Monroy, "Cognitive Digital Receiver for Burst Mode Phase Modulated Radio over Fiber Links," Eur. Conf. Optical Communication (ECOC), Torino, Italy, Sep. 2010, paper P6.11.

[85] F. N. Khan, Y. Zhou, A. P. T. Lau, and C. Lao, "Modulation Format Identifiaction in Heterogeneous Fiber-Optic Networks Using Artificial Neural Networks,",Opt. Express, vol. 20, no. 11, pp. 12422-12431, May 2012.

[86] R. Borkowski, D. Zibar, A. Caballero, V. Arlunno, and I. T. Monroy, "Optical Modulation Format Recognition in Stokes Space for Digital Coherent Receivers," Optical Fiber Communication Conf. Expo., Nat. Fiber Optic Engineers Conf. (OFC/NFOEC), Anaheim, CA, USA, Mar. 2013, paper OTh3B.3.

[87] R. Borkowski, D. Zibar, A. Caballero, V. Arlunno, and I.T. Monroy, "Stokes Space-Based Optical Modulation Format Recognition for Digital Coherent Receivers," IEEE Photon. Technol. Lett., vol. 25, no. 21, Nov. 2013.

[88] G. Bosco, M. Visintin, P. Poggiolini, A. Nespola, M. Huchard, and F. Forghieri, "Experimental Demonstration of a Novel Update Algorithm in Stokes Space for Adaptive Equalization in Coherent Receivers," Eur. Conf. Optical Communication (ECOC), Cannes, France, Sept. 2014.

[89] R. Boada, R. Borkowski, and I. T. Monroy, "Clustering Algorithms for Stokes Space Modulation Format Recognition," Opt. Express, vol. 23, no. 12, pp. 15521-15531, Jun. 2015.

[90] J. Liu, Z. Dong, K. Zhong, A. P. T. Lau, C. Lu, and Y. Lu, "Modulation Format Identification Based on Received Signal Power Distribution for Digital Coherent Receivers," Optical Fiber Communication Conf. Expo., Nat. Fiber Optic Engineers Conf. (OFC/NFOEC), San Fransisco, CA, USA, Mar. 2014, paper Th4D.3.

[91] M. C. Tan, F. N. Khan, W. H. Al-Arashi, Y. Zhou, and A. P. T. Lau, "Simultaneous Optical Performance Monitoring and Modulation Format/Bit-Rate Identification Using Principal Component Analysis," J. Opt. Commun. Netw., vol. 6, no. 5, pp.441-448, May 2014.

[92] S. Cui, S. He, J. Shang, C. Ke, S. Fu, D. Liu, "Method to Improve the Performance of the Optical Modulation Format Identification System Based on Asynchronous Amplitude Histogram," Optical Fiber Technology, vol. 23, p. 13-17, Jun. 2015.

[93] H.-C. Chien, A. Chowdhury, Z. Jia, Y.-T. Hsueh, and G.-K. Chang, "60 GHz Millimeter-Wave Gigabit Wireless Services over Long-Reach Passive Optical Network Using Remote Signal Regeneration and Upconversion", Optics Express, vol. 17, no. 5, pp. 3016-3024, Mar. 2009.

[94] A. Hirata, H. Takahashi, R. Yamaguchi, T. Kosugi, K. Murata, T. Nagatsuma, N. Kukutsu, and Y. Kado, "Transmission Characteristics of a 120-GHz-Band Wireless Link Using Radio-on-Fiber Technology", Journal of Lightwave Technology, vol. 26, no. 15, pp. 2338-2344, Oct. 2008.

[95] H.-J. Song, K. Ajito, A. Hirata, A. Wakatsuki, Y. Muramoto, T. Furuta, N. Kukutsu,, and Y. Kado, "8 Gbit/s Wireless Data Transmission at 250 GHz", Electronics Letters, vol. 45, no. 22, pp.1121-1122, Oct. 2009.

[96] A. Kanno, K. Inagaki, I. Morohashi, T. Sakamoto, T. Kuri, T. Kawanishi, Y. Yoshida, and K.-I. Kitayama, "40 Gb/s W-Band (75-110 GHz) 16-QAM Radio-over-Fiber Signal Generation and its Wireless Transmission", Optics Express, vol. 19, no. 26, pp. B.56-B63, Dec. 2011.

[97] S. Koenig, F. Boes, D. Lopez-Diaz, J. Antes, R. Henneberger, R. Schmogrow, D. Hillerkuss, R. Palmer, T. Zwick, C. Koos, W. freude, O. Ambacher, I. Kallfass, and J. Leuthold, "100 Gb/s Wireless Link with mm-Wave Photonics", PDP5B.4, in Conference on Optical Fiber Communication (OFC), Anaheim, CA, USA, Mar. 2013.

[98] X. Li, Z. Dong, J. Yu, N. Chi, Y. Shao, and G.-K. Chang, "Fiber-Wireless Transmission System of 108 Gb/s Data over 80 km Fiber and 2 x 2 Multiple-Input Multiple-output Wireless Link at 100GHz W-Band frequency", Optics Letter, vol. 37, no. 24, pp.5106-5108, Dec. 2012.

[99] X. Pang, A. Caballero, A. Dogadaev, V. Arlunno, R. Borkowski, J.S. Pedersen, L. Deng, F. Karinou, F. Roubeau, D. Zibar, X. Yu, and I.T. Monroy., "100Gbit/s Hybrid Optical Fiber-Wireless Link in the W-Band (75-110 GHz)", Optics Express, vol. 19, no. 25, pp. 24944-24949, Dec. 2011.

[100] W.-J. Jiang, C.-T. Lin, L.Y. He, C.C. Wei, C.-H. Ho, Y.-M. Yang, P.-T. Shih, J. Chen, and S. Chi, "32.65-Gbps OFDM RoF Signal Generation at 60 GHz Employing an Adaptive I/Q Imbalance Correction", Th.9.B.5, in European Conference and Exhibition on Optical Communication (ECOC), Torino, Italy, Sep. 2010.

[101] R. Sambaraju, D. Zibar, A. Caballero, J. Herrera, J.B. Jensen, I.T. Monroy, U. Westergen, A. Walber, and J. Marti, "Up to 40 Gb/s Wireless Signal generation and Demodulation in 75-110GHz Band Using Photonic techniques", in IEEE international Topical Meeting on Microwave Photonics, Montreal, QC, Canada, Oct. 2010.

[102] A. Stöhr, S. Babiel, P.J. Cannard, B. Charbonnier, F. van Dijk, S. Fedderwitz, D. Moodie, L. Pavlovic, L. Ponnampalam, C.C. Renaud, D. Rogers, V. Rymanov, A. Seeds, A.G. Steffan, A. Umbach, and M. Weiss, "Millimeter-Wave Photonic Component for Broadband Wireless System", IEEE Transactions on Microwave Theory and Techniques, vol. 58, no. 11, pp. 3071 – 3082, Nov. 2010.

[103] A. N'goma, C.-T. Lin, L.-Y.W. He, W.-J. Jiang, F. Annunziata, J. Chen, P.-T. Shih, J. George, and S. Chi, "31 Gbps RoF System Employingg Adaptive bit-loading OFDM Modulation at 60 GHz", OWT7, in Conference on Optical Fiber Communication (OFC), Los Angeles, CA, Mar. 2011.

[104] D. Zibar, R. Sambaraju, A. Caballero, J. Herrera, U. Westergen, A. Walber, J.B. Jensen, J. Marti, and I.T. Monroy, "High-Capacity Wireless Signal Generation and demodulation in 75-110GHz Band Employing All-Optical OFDM", IEEE Photonics Technology Letters, vol. 23, no. 12, pp. 810-812, Jun. 2011.

[105] J. Yu, X. Li, and N. Chi, "Faster than fiber: over 100-Gb/s Signal Delivery in Fiber wireless Integration system", Optics Express, vol. 21, no. 19, pp. 22885 – 22904, Sep. 2013.

CHAPTER 4

[106] Q. Zhuge et al., J. Lightw. Technol., Vol. 21, no. 31, pp.2621-2628, 2013.

[107] Y. Gao et al., paper Th.3.E.5, OFC, 2014.

[108] S. Tsukamoto, Y. Ishikawa, and K. Kikuchi, "Optical Homodyne Receiver Comprising Phase and Polarization Diversities with Digital Signal Processing", presented at the 32nd Eur. Conf. Exhib. Optical Communication, Cannes, France, Sept. 24-28, 2006.

[109] A. Swami and B.M. Sadler, "Hierarchical Digital Modulation Classification Using Cumulants", IEEE Trans. Commun., 48, 3, pp.416-429, 2000.

[110] B. Szafraniec, B. Nebendahl, and T. S. Marshall, "Polarization Demultiplexing in Stokes Space," Opt. Express, vol. 18, no. 17, pp.17928-17939, Aug. 2010.

[111] B. Szafraniec, T. S. Marshall, and B. Nebendhal, "Performance Monitoring and Measurement technique for Coherent Optical Systems," J. Lightw. Technol., vol. 31, no. 4, pp. 648-663, Feb. 2013.

[112] C. M. Bishop, Pattern Recognition and Machine Learning, 3rd ed., Springer, 2006.

[113] A. Getis, "Spatial Interaction and Spatial Autocorrelation: A Cross Product Approach," Environment and Planning A, vol. 23, no. 9, pp.1269-1277, Sep. 1991.

[114] J. Pan, P. Isautier, and S. E. Ralph, "Digital Pre-shaping for Narrowband Filtering Impairment Compensation in Superchannel Applications," paper JT3A, Advanced Photonics, Signal Processing in Photonics Communications (SPPCom), Rio Grande, PR, USA, Jul. 2013.

[115] J. G. Proakis and M. Salehi, Digital Communications, 5th ed., Boston: McGraw-Hill, 2008.

[116] J.A. Lopez-Salcedo, and G. Vazquez, "Frequency Domain Iterative Pulse Shape Estimation Based on Second-Order Statistics," IEEE 5th Workshop on Signal Processing Advances in Wireless Communications (SPAWC), Lisbon, Portugal, Jul. 2004. Frequency domain iterative pulse shape estimation based on second-order statistics

VITA

PIERRE ISAUTIER

ISAUTIER received the M.S. degree from Ecole Supérieure d'Electricité (Supélec), France. In 2013, he graduated with a M.S. in electrical and computer engineering from the Georgia Institute of Technology, Atlanta, GA, USA, where he pursued a Doctorate in electrical and computer engineering.

In 2012, he joined the Georgia Institute of Technology Terabit Optical Networking Consortium, a hybrid industry-academic research group at the intersection of fiber optics, high-speed digital communications, and digital signal processing.

His research interests are focused on ultra-high speed long-haul optical communication systems, autonomous signal identification and reconstruction, software-defined optical transceivers, secure optical networks and, radio frequency wireless photonics.

During his free time, he enjoys travelling, discovering new cultures, and reading about history, geopolitics, and religion.